

Nano Scale Cluster Devices

A thesis

submitted in partial fulfilment
of the requirements for the Degree

of

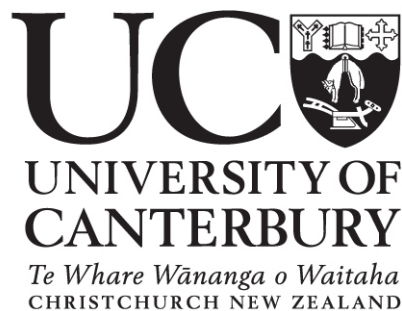
Doctor of Philosophy in Physics

in the

University of Canterbury

by

René Reichel



Department of Physics and Astronomy
2007

Science is like sex: sometimes something useful comes out, but that is not the reason we are doing it.

Richard Feynman

The most exciting phrase to hear in science, the one that heralds new discoveries, is not 'Eureka!' but 'That's funny...'.

Isaac Asimov

The definition of insanity is: Doing things over and over again and expect something different to happen.

Albert Einstein

Abstract

This study uses clusters formed in a UHV-compatible cluster apparatus, which was built and commissioned during this thesis. The design and operation of the cluster deposition system is described. This system is optimised for high cluster fluxes and for the production of cluster assembled nanoscale devices. One key feature of the system is a high degree of flexibility, including interchangeable sputtering and inert gas aggregation sources, and two kinds of mass spectrometer, which allow both characterisation of the cluster size distribution and deposition of mass-selected clusters. Another key feature is that clusters are deposited onto electrically contacted lithographically defined devices mounted on an UHV-compatible cryostat cold finger, allowing deposition at room temperature as well as at cryogenic and at elevated temperatures.

The electrically contacted nanoscale cluster devices were fabricated using a novel template technique. Hereby, clusters are placed between two electrodes separated only by ~ 100 nm. The width of the cluster ensemble is in the order of a few cluster diameters, which means that the assembled clusters form a cluster wire bridging the electrode separation. During this thesis, the design and layout has been optimised to be able to measure electrical properties of the cluster devices and in particular to investigate the interaction between the cluster ensemble and the contact electrodes.

In-situ electrical characterisation of cluster assembled nanoscale devices are performed in the temperature range 4.2 K to 375 K. The samples are provided with a backgate, which in principle allows modification of the conduction through the cluster ensemble by applying a gate voltage. However, no change in conduction with changes in gate voltages was seen.

The main focus of the electrical measurements is on the current voltage characteristics. It was noticed that the nanoscale bismuth (and antimony) cluster devices exhibited non-linear current voltage characteristics, which were in stark contrast to the linear current voltage characteristics measured for cluster films previously. Investigations into the causes of this non-linearity suggests that tunnelling conduction occurs between the cluster ensemble (wire) and the contact

electrodes. The non-linear current voltage characteristics were fitted using three models of tunnelling conduction and appear to be best fitted using a model involving fluctuation-assisted tunnelling through barriers of different heights.

Further, measurements of the temperature dependent resistance are performed showing an increase of resistance with decreasing temperature for bismuth and antimony assembled cluster devices. The temperature dependence of bismuth assembled cluster wires can be explained by the decrease of the carrier concentration in bismuth for decreasing temperature.

Annealing of the cluster ensemble and the cluster contact connection resulted in an increase in conduction. This increase of conduction can be explained due to the current flow through the cluster wire. Locally, at the bottlenecks, the current flow causes resistive heating and subsequently coalescence of two (or more) clusters.

Contents

List of Figures	vii
List of Tables	ix
Acknowledgements	xii
Preamble	1
Nanotechnology	1
Atomic Clusters	2
References	4
1 Introduction	5
1.1 Bismuth Cluster	6
1.1.1 What are Atomic Clusters?	6
1.1.2 Properties of Bismuth	8
1.2 Previous Studies	9
1.3 Percolation Theory	10
1.3.1 Theory	10
1.3.2 Finite-Size Effects	11
1.4 Previous Experiments at UC	12
1.4.1 Description of the Experiments	12
1.4.2 Percolating Bismuth Cluster Films	13
1.4.3 Bismuth Cluster Nanowires in V-Grooves	15
1.5 Research Outline	16
1.6 Fractal Conductance Fluctuations	18
1.6.1 Introduction	18
1.6.2 About Fractals	19
1.6.3 When Fractal becomes Non-Fractal	19
1.6.4 Sample Design and Problems	21
1.7 Bismuth Clusters and FCFs	22
1.7.1 Introduction	22
1.7.2 Proposed Sample Design	22
1.8 Contact Issues	23
1.8.1 Schottky Diode	23

1.8.2	Bismuth-Metal Contacts	25
1.9	Tunnelling Conduction	26
1.9.1	Simmons' Theory	27
1.9.2	Further Theories on Tunnelling Junctions	29
	References	32
2	Design of a UHV Cluster Apparatus	37
2.1	Introduction	37
2.2	Cluster Source Stage	39
2.2.1	Inert Gas Aggregation Source	40
2.2.2	Magnetron Sputtering Source	42
2.3	Differential Pumping	43
2.4	Mass Selection Stage	43
2.4.1	Mass-Filter	44
2.4.2	TOF	46
2.5	Sample Stage	47
2.5.1	Cryostat	48
2.5.2	Electrical Measurements	49
2.6	Modes of Operation	50
	References	51
3	Evolution & Utilisation	53
3.1	Gas Flow in Vacuum	53
3.2	The UHV-compatible Apparatus	56
3.2.1	Evolution of the Apparatus	56
3.2.2	Pump selection	57
3.2.3	Baking	58
3.2.4	Leak Testing	60
3.3	Inert Gas Aggregation Source	60
3.3.1	Introduction	60
3.3.2	Cluster Formation	61
3.3.3	Formation of a Molecular Cluster Beam	61
3.3.4	Bismuth Clusters using the IGA	64
3.3.5	Antimony Clusters	65
3.4	Magnetron Sputter Source	67
3.4.1	Introduction	67
3.4.2	Cluster Formation	68
3.4.3	Cluster Experiments	68
3.5	Mass Selection	70
3.5.1	Introduction	70
3.5.2	Mass Filter	71
3.5.3	Testing the TOF	72
	References	74
4	Sample Preparation	77
4.1	Introduction	77

4.1.1	Sample Preparation Steps	77
4.1.2	Facilities	79
4.2	Preparation Techniques	82
4.2.1	Formation of Backgate Contacts	82
4.2.2	Formation of Large Scale Contacts	83
4.2.3	Formation of Small Scale Contacts	83
4.2.4	Formation of the Passivation Layer	84
4.3	Sample styles	86
4.3.1	PMMA-templated Slot Samples	86
4.3.2	Four Point Samples	87
4.3.3	Percolating Film Samples	87
	References	90
5	Adhesion of Atomic Clusters	91
5.1	Introduction	91
5.2	PMMA Exposure and Residue	93
5.3	Cluster Coverage vs PMMA Exposure	95
5.3.1	Bismuth	95
5.3.2	Antimony	96
5.3.3	Quantitative Study	98
5.4	RMS Roughness vs PMMA Exposure	100
5.5	Discussion and Conclusion	102
5.5.1	Discussion	102
5.5.2	Simulational Studies	103
5.5.3	Conclusion	104
	References	107
6	Electrical Measurements	109
6.1	Preliminary Samples	110
6.2	Percolating Film Samples	111
6.2.1	Deposition Details	112
6.2.2	Annealing	113
6.2.3	Sample Ag ₂	115
6.2.4	Conclusion	115
6.3	Cluster Filled Slots	116
6.3.1	Bismuth Cluster Filled Slots	116
6.3.2	Antimony Cluster Filled Slots	123
6.4	Cluster Contact Four Point Samples	125
6.4.1	Why use Clusters as Contacts	125
6.4.2	Preparation	125
6.4.3	Four Point Measurements	126
6.4.4	R(T) Measurements	127
6.5	Four Point Samples with Metal Contacts	129
6.5.1	Bismuth Clusters	132
6.5.2	Antimony Clusters	133
6.5.3	Palladium Clusters	136

6.5.4	Annealing	138
6.5.5	Conclusion	140
6.6	Non-Linear I(V) vs Linear I(V)	140
6.6.1	Causes of Non-Linear Effects	141
6.6.2	Non-Linear I(V) Examples	142
6.7	Fitting the Data	143
6.7.1	Data Fitting Procedure	143
6.7.2	Fitting Parameters	144
6.7.3	Detailed Analysis	150
6.8	Summary	154
	References	156
7	Conclusions & Outlook	159

List of Figures

1.1	Ancient Nanotechnology. The Lycurgus Cup.	6
1.2	Photoelectron spectra of mercury clusters.	7
1.3	Band diagram of the semimetal Bismuth.	9
1.4	A typical percolation experiment using clusters. [?]	13
1.5	A cluster ‘wire’ formed between two sets of contacts. [?]	14
1.6	A V-groove in a silicon wafer.	15
1.7	The semiconductor billiard schematically.	17
1.8	The scaling plot for an empty billiard.	20
1.9	Fractal dimension D is plotted against Q	20
1.10	Formation of a Schottky barrier.	24
1.11	Band diagram for a bismuth and gold contact.	26
1.12	Tunnel Junction.	27
1.13	Comparison between the different theories.	30
2.1	Schematic drawing of the UHV-compatible Cluster Apparatus.	38
2.2	Schematic of size and shape for the nozzles used.	39
2.3	Schematic and nozzle placement for the IGA source.	40
2.4	Schematic crucible design and IGA source back plate.	41
2.5	Schematically Magnetron Sputter source.	42
2.6	Von Issendorff & Palmer mass selection system.	44
2.7	Mode of operation for the von Issendorff & Palmer mass selection.	44
2.8	Schematically the focusing of clusters using einzelenses.	45
2.9	Schematically TOF.	46
2.10	Schematic for the deposition chamber.	47
2.11	The 10 pin sample holder mounted on the cryostat cold finger.	49
3.1	RGA scan showing a typical vacuum atmosphere.	59
3.2	IGA source pressure versus gas flow of argon.	63
3.3	IGA source pressure versus gas flow.	63
3.4	Size dependence of antimony clusters with helium/argon ratio.	66
3.5	Antimony clusters at the apexes of V-grooves and on plateaus.	67
3.6	Silicon clusters produced with the magnetron sputter source.	70
3.7	Mass distribution for Pd clusters using the magnetron sputter source.	71
3.8	TOF mass spectrum for Pd clusters.	73

4.1	Sample preparation of slot samples and four point samples.	78
4.2	A typical large scale contact layout.	78
4.3	EBL pattern used for the formation of the four point samples.	80
4.4	Patterns used to form the slot samples.	81
4.5	Bi-layer process	84
4.6	Process of the formation of a passivation layer.	85
4.7	Alignment marks.	86
4.8	Example of a slot sample.	86
4.9	Example of a four point sample.	87
4.10	A simple percolating film sample with bismuth cluster.	88
4.11	Spray painting versus thermal evaporation.	88
5.1	Fundamental processes in cluster surface collisions.	92
5.2	Mechanism diagram in cluster surface collisions.	93
5.3	Opening pattern in PMMA exposed with a dosage of $80 \mu\text{C}/\text{cm}^2$	94
5.4	Opening pattern in PMMA exposed with a dosage of $140 \mu\text{C}/\text{cm}^2$	94
5.5	Variation in coverage of Bi clusters for varying exposure dosages.	96
5.6	Variation in coverage of Sb clusters for varying exposure dosages.	97
5.7	Variation in coverage of Sb clusters for varying exposure dosages.	97
5.8	Bismuth clusters in partially exposed patterns in PMMA.	98
5.9	Variation in coverage (quantitatively) of bismuth clusters.	99
5.10	Variation in coverage (quantitatively) of antimony clusters.	99
5.11	Partially exposed and developed HMW PMMA.	101
5.12	RMS roughness of HMW PMMA.	102
5.13	Adhesion probability of a cluster with varying impact velocity.	104
5.14	Bismuth clusters form the map of New Zealand.	105
5.15	Antimony clusters form the map of New Zealand.	105
6.1	Schematic layout of a slot sample.	110
6.2	Schematic layout of a percolating film sample.	111
6.3	Onset curves for samples Ag2 and Au2.	112
6.4	$I(V)$ characteristic for sample Ag1.	114
6.5	$I(V)$ characteristic for sample Ag2.	115
6.6	Bismuth cluster filled slot sample.	116
6.7	$I(V)$ for slots#7.	120
6.8	$I(V)$ for slots#18.	121
6.9	$I(V)$ for slots#26.	121
6.10	Antimony cluster filled slot sample.	124
6.11	$I(V)$ for sample slots#22	124
6.12	A cluster contact 4 point sample.	125
6.13	$I(V)$ characteristic for sample 4pt#1.	127
6.14	Temperature dependent four point resistance of sample 4pt#3.	128
6.15	Schematic layout of the four point samples.	129
6.16	FE-SEM image showing sample 4pt#17.	130
6.17	Labelling convention of the contacts.	131
6.18	2-point resistance measurement of contacts 12&78 of sample 4pt#21.	134

6.19	2-point resistance measurement of contacts 12&78 of sample 4pt#18.	134
6.20	2-point resistance measurement of contacts 34&56 of sample 4pt#4.	134
6.21	4-point resistance measurement of sample 4pt#18	135
6.22	4-point resistance measurement of sample 4pt#21	135
6.23	2-point resistance measurement of contacts 34&56 of sample 4pt#28.	136
6.24	4-point resistance measurement sample 4pt#16.	137
6.25	4-point resistance measurement for sample 4pt#15	138
6.26	Annealing with fixed voltage.	138
6.27	Accidentally ‘annealed’ nanoscale cluster device.	139
6.28	Annealing with fixed current.	140
6.29	Fit curves and data for I/V of contacts 34&56 of sample 4pt#28.	151
6.30	Detail of Figure 6.29.	151
6.31	Residual $I(V)$ for contact 34&56 of sample 4pt#28.	152
6.32	Residual $G(V)$ for contact 34&56 of sample 4pt#28.	152
6.33	$G(V)$ for contact 12&78 of sample 4pt#27.	153
6.34	$G(V)$ for contact 34&56 of sample 4pt#18.	154

List of Tables

3.1	Calculated Pressures at various stages.	55
3.2	Typical source conditions using the IGA source.	65
3.3	Typical source conditions using the magnetron sputter source . .	68
6.1	Deposition details of the percolating film samples.	112
6.2	Onset resistances and resistances after a 10 V ramp anneal.	113
6.3	List of the bismuth slot samples.	117
6.4	List of the antimony slot samples.	123
6.5	Deposition details 4pt cluster contact samples	126
6.6	Resistances of 4pt cluster contact samples.	126
6.7	List of the cluster four point samples.	130
6.8	Comparison of sample layouts.	139
6.9	Fit parameters using Equation 1.17.	145
6.10	Barrier heights and barrier widths.	146
6.11	Fit parameters using Equation 1.21.	148
6.12	Fit parameters using Equation 1.22.	149
6.13	Fit parameters using Equation 1.22. 4pt#27	153

Acknowledgements

First I would like to thank my supervisor Dr Simon Brown for supporting me throughout these years.

Many a thanks to all the technical staff at the Physics and Astronomy Department without their help this research would not have been possible: Owen Cauhgley who welded and machined the body of the UHV compatible cluster apparatus; Ross Ritchie and Geoff Graham for building the flow controller and the voltage supply; Graeme McDonald for his support on the turbo pumps; Wayne Smith who machined the small bits and pieces which later became the sample holders; Bob Flygenring for his steady supply of cryogenic fluids; and Graeme Kershaw. Further thanks also to the staff in the Electrical and Computer Engineering Department: Helen Devereux and Gary Turner.

How would this all be without the computer support. Thanks to Orlon Petterson, Jeremiah Brown and Paul Arnold. You kept it running.

During the darkest times and longest hours, what would I have done without the assistance of my fellow students in the cluster group: Ahmad Ayesh, Dr Martin Kaufmann, Monica Schulze, Dr Shelly Scott, Dr Andreas Wurl, KC Tee, David McCarthy, David Mackenzie, Gaelle Parquez and Toby Mathewson.

Vital information and support came also from the Post Docs in the cluster group: Dr Alan Dunbar, Dr Jim Partridge, Dr Franck Natali and Dr Euan Boyd.

Working along side a company that does research on clusters is of great benefit, too. Thanks for the support therefore goes to the staff of NCD: Dr Andreas Lassesson, Dr Joris van Lith, Monica Schulze and Shannon Kopp.

Last, but definitely not least I would like to thank my parents and my partner Dominique. They have always supported me throughout these years. Even when I decided to go to the other side of the world to conduct my research; they were there for me.

Preamble

Nanotechnology

Over the last few years, a scientific and technical revolution has begun. The ability to systematically organize and manipulate matter on the nanometre length scale formed a new branch of science — Nanotechnology. Yet, what actually makes the nanometre length scale so important?

A key feature of biological systems is the systematic organization of matter on the nanometre length scale. Nanotechnology promises to allow us to place artificial components and assemblies inside cells, and to make new materials using the self-assembly methods of nature. This is a powerful new combination of materials science and biotechnology [Montemagno and Bachand, 1999; Freitas, 1999].

Furthermore, changes to the structure of materials in the range about 10^{-9} to 10^{-7} m can modify material behaviour. This means materials constructed of nanometre-scale components can be engineered to have entirely new properties, which may not even exist in nature. Composites can be produced that combine the most desirable properties of very different materials to obtain characteristics that are greatly improved over those that nature supplies or that appear in combinations nature does not produce.

Nanostructuring can bring wear-resistant tires made by combining nanometer-scale particles of inorganic clays with polymers. It can promise advances for nanoparticles as medicines with vastly improved delivery and control characteristics. Greatly improved printing can be achieved by nanometre-scale particles combining the best properties of both dyes and pigments. Controlling layer thickness to better than a nanometre can vastly improve lasers and magnetic disk heads.

The combination of nanotechnology and biotechnology could produce ingestible systems that are harmless to the patient and that could enable a physician to determine the type and location of diseased cells and organs, if there are problems. Nanometer-scale traps could remove pollutants from the environment and

deactivate chemical warfare agents. Computers with the capabilities of current workstations could be the size of a grain of sand and could be able to operate for decades with the equivalent of a single wristwatch battery. Robotic spacecraft that weigh only a few pounds could be sent out to explore our solar system, and perhaps even the neighbouring stars.

The total societal impact of nanotechnology is expected to be greater than the total influence that the silicon integrated circuit, medical imaging, computer-aided engineering, and synthetic polymers have had in the last century. Significant improvements in performance and changes of manufacturing paradigms could lead to several industrial revolutions in the 21st century. Nanotechnology could change the nature of almost every human-made object.

For further speculations and more controversial visions, see ‘Engines of creation’ by K. E. Drexler [Drexler, 1990]. Noting that technological advances have caused some of the deepest transformations in human history, he studies emerging technologies with the power to cause future global transformations. The book outlines the prospects for advanced molecular manufacturing technology, its capabilities, their medical, environmental and economic implications, dangers and security risks, and potential policy responses. He introduced the term ‘nanotechnology’ to describe a vision articulated by Richard Feynman [Feynman, 1959] and the technologies it will enable.

Atomic Clusters

The approach to nanotechnology in this group is to study and to make use of the interesting properties of atomic clusters. Atomic clusters are finite aggregates of atoms or molecules that are bound by forces which may be metallic, covalent, ionic, hydrogen-bonded or Van-der-Waals in character and can contain from a few to tens of thousands of atoms. Although, clusters can be prepared in a number of ways, in this group the production by inert gas aggregation and the formation of a molecular beam of clusters is used. This technique accounted for an enormous growth in the field of cluster science. The resulting atomic clusters can be mass-selected, deposited onto substrates and subjected to high-resolution microscopy, which allows performing very detailed and sensitive studies.

Atomic clusters exhibit not only a range of useful electronic, chemical and magnetic properties they also show great potential as building blocks for nanoscale devices. With this ‘bottom-up’ approach, nanoscale resolution can be achieved instantly. This differs from the highly developed and reliable state-of-the-art ‘top-down’ approach, a combination of lithography and etching, achieving devices with dimensions of about 10 nm currently only at great expense. The ‘bottom-up’ approach however suffers from a range of other problems, like the difficulty, expense, and long times that can be required to assemble the building blocks.

To explore the unique properties of atomic clusters controllable assembly and integration in larger scale devices is necessary in a combination of both the ‘top-down’ and ‘bottom-up’ approach. One simple technique is the random deposition of atomic clusters between prefabricated lithographically defined nanoscale contacts, which can be understood with percolation theory [Schmelzer Jr. et al., 2002]. Another way is the assembly of atomic clusters into working devices using a new template technique [Brown and Partridge, 2003; Partridge et al., 2003].

We are especially interested in the electrical properties of atomic clusters and in the formation of atomic cluster assembled devices [Schmelzer Jr. et al., 2002; Brown and Schmelzer Jr., 2002]. Particularly interesting, are the properties of nanoscale atomic cluster devices with regard to fractal conductance fluctuations (FCFs) (see Section 1.6).

The aim of this PhD thesis is to study conductance through nanowires and/or square systems formed from atomic clusters in order to observe fractal conductance fluctuations (FCFs) [Taylor et al., 1997]. Previously, FCFs have only been studied in semiconductor billiards. The development of a detailed formalism for the characterisation of nanoscale devices using FCFs will help to understand these effects and could lead to new device functionality.

For this study a new approach to forming nanoscale cluster devices has been developed. Atomic cluster are deposited between two electrodes to bridge a spacing between the electrodes of about 100 nm. The clusters used for this research were produced using a new UHV-compatible cluster apparatus which was built and commissioned during this thesis.

References

Brown, S. A. and Partridge, J. G. (2003). Templated cluster assembled wires. New Zealand Patent Application No. 524059. Provisional Patent Application lodged 7 February 2003.

Brown, S. A. and Schmelzer Jr., J. (2002). Nanoscale electronic devices & fabrication methods. New Zealand Patent Application No. 513637. PCT Application filed August 20, 2002.

Drexler, K. E. (1990). *Engines of creation*. Fourth Estate, London. www.foresight.org/EOC/index.html.

Feynman, R. P. (1959). There's plenty of room at the bottom. A talk given by Richard P. Feynman on December 26, 1959, at the Annual Meeting of the American Physical Society, held at the California Institute of Technology. www.its.caltech.edu/~feynman.

Freitas, R. A. (1999). *Nanomedicine*, volume I. Landes Bioscience, Georgetown TX. www.nanomedicine.com/NMI.htm.

Montemagno, C. and Bachand, G. (1999). Constructing nanomechanical devices powered by biomolecular motors. *Nanotechnology*, 10:225.

Partridge, J., Scott, S., Dunbar, D., Schulze, M., Brown, S. A., Wurl, A., and Blaikie, R. (2003). Self-assembled cluster nanowires. In *Symposium on Microtechnologies for the New Millennium*, volume 411, Gran Canaria. SPIE5118.

Schmelzer Jr., J., Brown, S. A., Wurl, A., Hyslop, M., and Blaikie, R. J. (2002). Finite-size effects in the conductivity of cluster assembled nanostructures. *Phys. Rev. Lett.*, 88:226802.

Taylor, R. P., Newbury, R., Sachrajda, A. S., Feng, Y., Coleridge, P. T., Dettmann, N., Zhu, N., Gou, H., Delage, A., Kelly, P., and Wasilewski, Z. (1997). Self-similar magnetoresistance of a semiconductor sinai billiard. *Phys. Rev. Lett.*, 78:1952.

Introduction

The focus of this work is on the investigation of cluster assembled nanoscale devices using an Ultra High Vacuum (UHV) compatible cluster apparatus which was built and commissioned at the beginning of this PhD. This chapter is to introduce the reader to the outline of this thesis and to background information for the research presented in this thesis.

The first section (Section 1.1) of this chapter provides useful information regarding atomic clusters. Particularly explained are bismuth clusters which were of main interest to this work. The properties of bismuth are presented that make bismuth clusters such an interesting candidate for investigation.

Previous studies done elsewhere using atomic cluster devices are shown in Section 1.2. Before shifting to the work previously done by the group at the University of Canterbury a short introduction to percolation theory is given (Section 1.3). The previous experiments done by the group at the University of Canterbury can be found in Section 1.4.

Section 1.5 then provides the idea which ignited the interest in the investigation of fractal conductance fluctuation (FCF) in (bismuth) cluster assembled nanoscale devices. This is followed by an explanation of what FCFs are (Section 1.6) and how previous studies of FCFs were carried out.

From there, the focus is switched back to the outline of this research and how bismuth clusters could be used to investigate FCFs in cluster assembled nanoscale devices (Section 1.7). A concept sample design is presented and following, possible known problems like contact issues (Section 1.8) are discussed. This section starts with a short overview of metal-semiconductor junctions or Schottky diodes before discussing the (bulk) bismuth contact junction.

Electrical contacts to clusters are difficult to form due to the small nature of clusters. For instance tunnelling barriers at the contacts could dominate the conduction. The theory which is used to explain tunnelling conduction in scanning tunnelling microscopy and which can be used to understand the bismuth cluster contact junction is presented in Section 1.9.



Figure 1.1: Ancient Nanotechnology. The Lycurgus Cup (British Museum) has a normal green colour, but when illuminated from the inside changes to red.

1.1 Bismuth Cluster

1.1.1 What are Atomic Clusters?

The Oxford dictionary defines a cluster as a group of similar things positioned or occurring closely together [Oxford, 2006]. The term is widely used even in science. For example a computer cluster is the linking of several computers to increase speed and computing power. Astrophysics uses the term of cluster to refer to groups of stars — grouped together over vast distances. In the context of this thesis, the term cluster is referring to the grouping of atoms or molecules to form small particles. The small particles are collectively known as ‘atomic clusters’ or just ‘clusters’. For reasons of simplicity, atomic clusters are called ‘clusters’ throughout the rest of this thesis.

Clusters are not new. — They have been in use for a long time; even though probably not knowingly. For instance the colouring of Roman glass is due to the inclusion of small gold particles in the melt. The Lycurgus Cup (shown in Figure 1.1) made in the 4th century has normally a green colour. If illuminated from the inside of the cup, the colour changes to a reddish colour. It has now been determined that this effect results from 70 nm small gold particles (clusters) in the glass [Barber and Freestone, 1990]. — Neither are clusters rare. In fact they are all around us. In the atmosphere, clusters are the precursors to rain or hail.

From the definition of atomic clusters, it can be seen that clusters can consist of a wide variety of different materials. Even the way the atoms or molecules within a cluster are bound together can vary widely. There are clusters that are bound by metallic, covalent, ionic, hydrogen-bonded or Van-der-Waals forces. The cluster size can range from less than a nanometre to several tens of nanome-

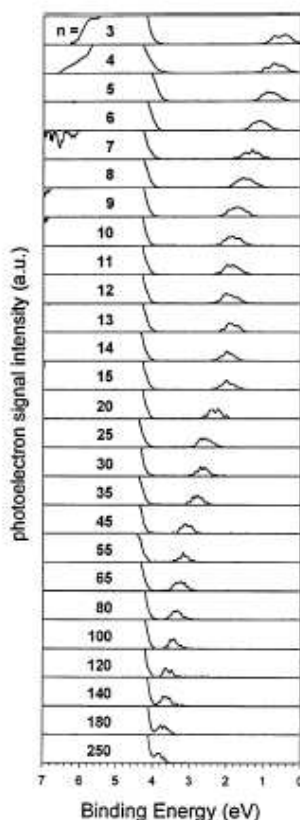


Figure 1.2: Photoelectron spectra of mercury clusters. The cluster size varies between 3 and 250 atoms. [Busani et al., 1998]

tres, containing from a few to tens of thousands of atoms. Clusters bridge the size range from single atoms to the bulk material.

Clusters even differ in the way of how they are prepared. They can be made in solution, forming colloidal particles or formed from the vapour phase of the respective component of the clusters. For more information on the formation of clusters from the vapour phase refer to Section 3.3.2.

The properties exhibited by clusters are unique and different from the properties of the atom or bulk of the respective atoms or molecules they are made of. Furthermore, those properties change from the atomic properties to bulk properties of the respective material. This means that unique materials with tailor-made properties can be fabricated. Many of the cluster properties can be explained by the increased surface area of clusters. In atomic clusters, the fraction of atoms at the surface to atoms inside is very high, whereas the surface atoms are negligible in bulk material. Therefore, the surface properties affect all energy related properties. Because their properties can be much different from single atoms or the bulk, they were proposed to be the fifth state of matter [Stein, 1979].

One such property is the bandgap determining whether a material is metallic or of semiconducting nature. In the semiconductor industry, the bandgap of

semiconductors is tuneable by adjusting the material composition of the semiconductor. Using clusters, the bandgap can be changed simply by adjusting the size of the clusters. Figure 1.2 shows the photoelectron spectra of different size mercury clusters. Bulk mercury is a metal. However, in Figure 1.2, it can be clearly seen that for the 3 atom mercury cluster a wide bandgap exists. By adding more and more atoms to the mercury cluster and changing its size the bandgap closes. Hence, mercury clusters can be changed from metal clusters to semiconducting clusters [Busani et al., 1998]. Another physical property which can be changed depending on the size of the clusters is the melting temperature. As the size of tin clusters decreases the melting temperature drops rapidly [Lai et al., 1996].

Clusters not only exhibit a range of useful adjustable electronic, chemical and magnetic properties they also show a great potential as building blocks for nanoscale devices as well. Clusters can be mass-selected to select a particular property associated with that size and deposited onto substrates. Further, size selected clusters can be used in a so called ‘bottom-up’ approach where nanoscale resolution can be achieved instantly. This differs from the highly developed and reliable state-of-the-art ‘top-down’ approach, a combination of lithography and etching, achieving devices with dimensions ~ 10 nm currently only at great expense. For further reading, the first chapter in [Haberland, 1994] is an informative introduction to the field of cluster physics.

1.1.2 Properties of Bismuth

As described previously, clusters are a unique system having unique properties which can be tailored. Bismuth is not only an interesting candidate to form clusters from; it is also a material of which clusters can be easily formed from the vapour phase. The melting point of bulk bismuth is 271.3 °C [Stöcker, 1994] which can be easily achieved using an inert gas aggregation source. A more important property to be able to form clusters is the vapour pressure. Even though the bulk material melts there might not necessarily be enough vapour readily available to achieve cluster growth. Nevertheless, bismuth has a high vapour pressure at low enough temperatures. The temperature needed to get a bismuth vapour pressure of about 1 Torr is 897 °C [VEECO, 2006], which is easily achieved using an inert gas aggregation source.

As a bulk material, bismuth is a brittle heavy metal. Compared to other metals, bismuth has a very high resistivity of $107 \times 10^{-6} \Omega\text{cm}$ [Stöcker, 1994]. Of all the metals it has the highest Hall effect [WebElements Ltd, 2006]. And apart from mercury it has the lowest thermal conductivity. Due to its band structure, bismuth is thought of as a semimetal. From solid state theory, the position of the valence band and the conduction band relates to the conduction mechanism in solids. In metals the valence band and the conduction band overlap; whereas semiconductors having a small separation between them. For the case of bismuth

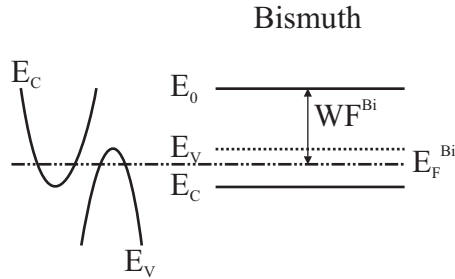


Figure 1.3: Band diagram of the semimetal Bismuth.

(see Figure 1.3) the conduction band is only 0.023 eV below the Fermi level [Dinger and W., 1972; Isaacson and Williams, 1969]. For ‘normal’ metals the bottom of the conduction band is usually a few eV below the Fermi level. The work function of bismuth, i.e. the amount of energy needed to free one electron, is 4.22 eV [Stöcker, 1994].

The mean free path of electrons within bulk bismuth is ~ 250 nm at room temperature with an (anisotropic) Fermi wavelength of ~ 40 nm, which is about 100 times more than ‘normal’ metals [Smith et al., 1964]. Due to the large Fermi wavelength, it is possible to construct structures with a comparable size range. Typical bismuth clusters produced at the University of Canterbury have sizes of around 30-40 nm. It has been suggested that using bismuth as cluster material, quantum properties may be observable at high temperatures (see Section 1.7).

1.2 Previous Studies

Using quench-condensed bismuth clusters, Kubatkin et al. [Kubatkin et al., 2000] have seen Coulomb blockade effects. At low temperatures (4.2 - 11 K) Coulomb steps could be observed in the $I(V)$ characteristics when applying a negative gate voltage to the cluster. The charging energy was reported to be always greater than 10 meV.

As mentioned previously, bismuth is a semimetal with a small band overlap. It has been shown that a semimetal to semiconductor transition can occur in bismuth nanowires [Lin et al., 2000b]. A metal-semiconductor junction characteristic was noticed in the current-voltage analysis of Y-branched bismuth nanowires [Tian et al., 2004]. Step-shaped bismuth nanowires showed metal-semiconductor junction behaviour as well [Tian et al., 2006].

Investigation of the transport properties of Bismuth nanowire arrays doped with Te were performed [Lin et al., 2000a] to explain various temperature dependent resistivity measurements. The resistance temperature characteristic was found to depend on Te dopant concentration, boundary effects, impurities and on phonon scattering.

In studies of the thermoelectric properties of bismuth nanowires [Cronin et al., 2002] it was noticed that the $I(V)$ characteristic showed non-linear behaviour. This was understood as a tunnelling through an oxide shell formed around the bismuth nanowire. It was suggested that tunnelling contacts could be used to perform tunnelling spectroscopy on bismuth nanowires. This would allow the measurement of the electronic density of states in bismuth nanowires.

1.3 Percolation Theory

Before explaining the previous cluster device experiments done at the University of Canterbury, this section explains some of the background theory needed. Some ideas presented in this section will be used later in the text, too.

In order to take advantage of the distinct properties of atomic clusters they need to be incorporated into working small-scale devices. In addition, the small overall system size of devices will exhibit distinctive properties due to finite size effects in cluster-assembled nanostructures. Depositing clusters from a molecular beam onto a substrate is a completely random process. There is a range of parameters that can be controlled, like cluster material, their size and the system size.

To understand how the electrical properties of a randomly deposited cluster film evolve with growing thickness of the film, percolation theory offers a relatively easy model. Together with scaling analysis, it can also explain how the system size may alter the conduction through cluster films.

1.3.1 Theory

This section will introduce the reader briefly to percolation theory. A more detailed explanation can be found elsewhere [Grimmett, 1989; Stauffer, 1985].

Percolation deals with the effects of varying the richness of interconnections present in a random system. The basic idea of percolation is the existence of a sharp transition at which the long-range connectivity of the system appears (or, going the other way, disappears). This transition occurs abruptly when some generalized density in this system reaches a critical value p_c (the percolation threshold).

As an example, the growth process of a thin cluster film can be modelled using percolation theory. At the beginning, the film consists of a few well-separated clusters on a substrate. Hopping conduction is the only way for electronic transport in this film. With the increase in average cluster density, conducting paths between neighbouring clusters appear, and some clusters are electrically connected. At p_c , the first unbroken conducting path extending through the film appears. This is the percolation threshold for the cluster film. Further deposition will construct more and more conducting paths and increase their widths.

However, this example represents an already complex disorder in a system. Not only is the disorder-generating statistical variable (whether there is a connection between islands) random, but the position of islands on the substrate is random (clusters can overlap). This is a kind of continuum percolation model.

To simplify, we could assume a regular geometry, e.g. a 2D square lattice. Disorder is then only introduced by superimposing on such a lattice the randomly deposited clusters. This is known as site percolation on an infinite 2D lattice or as discrete lattice percolation.

In this model [Rintoul and Torquato, 1997], the occupation of a site on the infinite 2D lattice by a cluster represents the statistical variable. One site can only accommodate one cluster (unlike the example given previously). A connection has occurred when two neighbouring sites are both occupied. If the variable p represents the coverage of clusters between 0 and 1, the fraction of occupied sites is p and the remaining empty sites are given by the fraction $(1-p)$. Increasing the coverage means increasing the number of connections between clusters to ever-larger groups of conducting networks. At a specific coverage, this network will span from one side of the system to the other. This is the previously-mentioned percolation threshold p_c , which has been shown to be $p_c = 0.5927461$ for an infinite 2D square lattice [Newman and Ziff, 2000]. For an infinite system, the probability ψ that a spanning cluster exists, is 0 below p_c and 1 above. The threshold p_c also marks a sharply defined point where a phase transition occurs. A spanning cluster appears and conduction through the system becomes possible. The derivative $d\psi(p)/dp$ gives then the probability that for a given coverage p a spanning cluster appears. A finite system can have a spanning cluster before or after the percolation threshold.

From percolation theory [Stauffer, 1985], characteristics of a percolating system are related to the probability of occupation of sites on the lattice by a power law. The functional form for such a characteristic diverges or vanishes at p_c . The conductivity σ and the correlation length ξ can then be written as:

$$\sigma \propto (p - p_c)^t, \quad (1.1)$$

$$\xi \propto (p - p_c)^\nu. \quad (1.2)$$

However, this describes only the functional dependence for the characteristics. The exponents t and ν nevertheless have to be determined by experiments or simulations.

1.3.2 Finite-Size Effects

As mentioned previously, in an infinite 2D lattice a spanning cluster only exists for $p > p_c$. Physical systems of interest are finite. For a finite lattice of size L , the various functions of characteristics of a percolating system vary according to

finite-size scaling theory [Stauffer, 1985] by a scaling ansatz:

$$X(p, L) = L^{-A} f_X((p - p_c)L^B), \quad (1.3)$$

where f_X is a suitable scaling function for X . The components A and B can be found for the limits $L \rightarrow \infty$ and $p = p_c$. This leads to:

$$\sigma(p, L) = L^{-t/\nu} f_\sigma((p - p_c)L^{1/\nu}), \quad (1.4)$$

$$\psi(p, L) = f_\psi((p - p_c)L^{1/\nu}), \quad (1.5)$$

$$\frac{d\psi}{dp}(p, L) = L^{1/\nu} f'_\psi((p - p_c)L^{1/\nu}), \quad (1.6)$$

with t the exponent for the conductivity and ν the exponent for the correlation length [Schmelzer Jr., 2001]. Now, for a finite lattice, conduction can occur even for coverage lower than p_c , due to a finite probability $d\psi/dp$ of having a cluster chain spanning the lattice before the coverage p_c is achieved.

1.4 Previous Experiments at the University of Canterbury

The following experiments were performed at the University of Canterbury. Clusters were deposited onto lithographically pre-formed electrical contact structures to form nanoscale devices [Schmelzer Jr. et al., 2002]. Cluster-assembled nanowires on V-grooved substrates [Partridge et al., 2003b], percolating films [Schmelzer Jr. et al., 2002], and open square systems [Dunbar et al., 2004] were fabricated and have allowed investigation of conduction through nanowires, cluster films and ensembles of clusters, respectively. This section reviews those experiments.

1.4.1 Description of the Experiments

For the original experiments, a high-vacuum (HV) cluster system was used. The system, originally built in Switzerland [Hall, 1991; Flüeli, 1989], was designed to study the structure of unsupported clusters with electron beam diffraction. This study included diffraction studies of lead and zinc [Hyslop, 2002], bismuth [Wurl, 2003] and antimony [Kaufmann, 2006]. The clusters were produced using an inert gas aggregation source, where the cluster aggregation is assisted by a flow of inert gas. The inert gas also forms a molecular beam of clusters leaving the source through a small aperture.

The incorporation of a crude sample stage into the main chamber allowed deposition of clusters onto contacted samples at pressures of around 10^{-6} Torr. However, this HV system was always limited to the characterization of just one

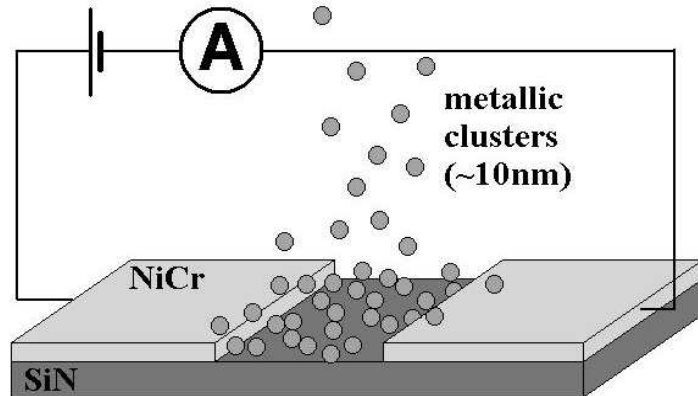


Figure 1.4: A typical percolation experiment using clusters. [Brown, 2007]

sample at a time. In addition, the cluster beam was very narrow and highly inhomogeneous. The alignment of the sample within the cluster beam proved to be difficult. During this thesis the HV system was used as well (during the commissioning of the mass filter in the UHV system). The difficulties in the beam alignment and the narrow beam spot however lead to no conclusive results.

The deposition was performed in the main chamber (chamber used for the diffraction studies) of this HV system. That meant, once the deposition was done, the cluster assembled devices would be left in a vacuum chamber at pressures of around 10^{-6} Torr. The relatively high pressures deteriorated the cluster deposited samples with time due to water layer formation and subsequent oxidation of the cluster assembled devices [Schulze et al., 2003].

For the electrical measurements clusters were deposited on lithographically defined samples, which were prepared on 8×8 mm² silicon oxide on silicon substrates. The active device was positioned in a 3×3 mm² area at the centre of the sample. Contact to the outside was made from the contact pads on the sample to a plastic chip carrier, which was then connected via a 10 wire cable to an outside breakout box.

1.4.2 Percolating Bismuth Cluster Films

The samples for this research incorporate bismuth clusters deposited between electrical contacts separated by ~ 100 nm. The nature of this device is somewhere between a percolating film of bismuth clusters and a chain or nanowire of bismuth clusters. The following shows some previous results found for percolating bismuth cluster films by the group at the University of Canterbury.

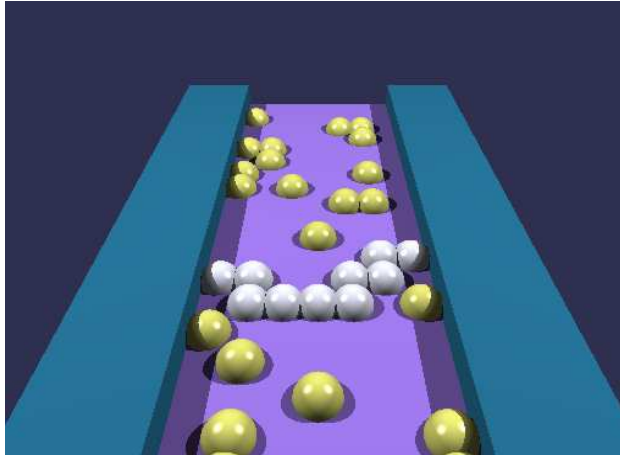


Figure 1.5: A cluster ‘wire’ formed between two sets of contacts. [Brown, 2007]

Investigations of the finite-size effects of bismuth cluster films, both theoretical and experimental, found that the coverage at which an onset of conduction occurs varies as a function of system size with a power law [Schmelzer Jr., 2001]. For those experiments, clusters were deposited between electrodes shaped in the form of inter-digitated fingers with narrow spacing L . Figure 1.4 shows schematically the experiment. Once a current was measured the deposition was stopped. The spacing between the electrodes relates to a finite size percolation network of size L . The spacing used varied between $1\ \mu\text{m}$ and $4\ \mu\text{m}$. The onset coverage was determined by measuring the deposition rate before and after the deposition. Due to the narrow and highly inhomogeneous beam variations in the coverage could occur. To overcome the problem to determine the onset coverage for a given L , the critical thickness for the onset was measured. A reference sample was prepared and the critical thickness for all spacings L were related to the reference sample [Schmelzer Jr. et al., 2002]. Measurements for the critical thickness were performed using an atomic force microscope after the deposition and outside the vacuum chamber.

Using those previous studies, the electronic properties of cluster-deposited bismuth nanowires were investigated [Schulze et al., 2003]. The wires were formed by random cluster deposition between interdigitated fingers. No control over the position and number of wires was possible. The minimum length of the wire was determined by the spacing L between the interdigitated fingers. For a small enough spacing L a conducting path can occur before the percolation threshold is reached. This path resembles a nanowire. Figure 1.5 shows schematically such a cluster wire.

This study [Schulze et al., 2003] found that the resistance of such produced bismuth nanowire can be modified by increasing the voltage across the film. Temperature dependent resistance measurements showed that the resistance of the cluster deposited bismuth nanowires increases with decreasing temperature.

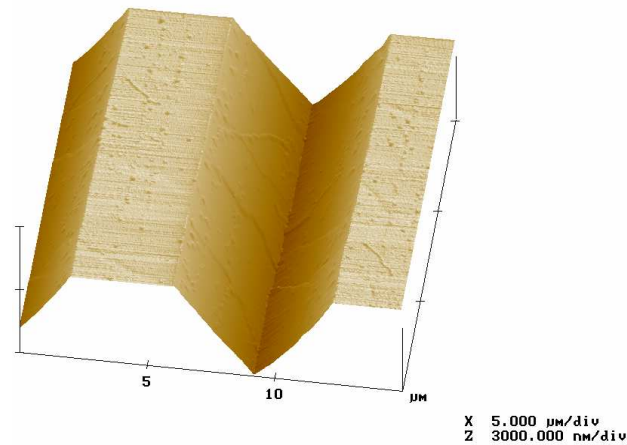


Figure 1.6: A V-groove in a silicon wafer.

FCFs were observed for semiconducting billiards by applying a magnetic field. For the bismuth cluster nanowires, magnetoresistance measurements however have shown no response for fields as high as 5 T. Since the samples had to be exposed to air prior to the magnetoresistance measurements the bismuth nanowires were most likely oxidised. FCFs are predicted to occur for variation of the applied electric field (as a gate) as well.

In the resistance of bismuth nanowires, various steps were observed [Gourley, 2002; Schulze et al., 2003] which were related to oxidation, random telegraph noise or current flow. Some of them were reproducible and others were not. Oxidation was found to be a major problem in fabricating bismuth nanowires, increasing the resistances of the wires.

Furthermore, the field of interest was extended to studies of antimony cluster and silver cluster percolating films [Dunbar et al., 2006]. Antimony clusters and silver clusters were also produced in the aforementioned HV cluster apparatus using an inert gas aggregation source.

1.4.3 Bismuth Cluster Nanowires in V-Grooves

The method of forming bismuth nanowires by percolating clusters is relatively crude. Neither the position, nor the length nor the number of wires could be selected. A more preferred way is the deposition of bismuth cluster wires at selective sites. It was shown that growing nanowires on a substrate can be done due to highly selective aggregation of clusters at step-edges [Francis et al., 1996]. However, this possibility does not allow control of desirable locations of the cluster chains because the features promoting aggregation are surface defects. In addition, the substrate used was a conducting substrate. A more direct and controlled way of forming nanowires is the assembly around man-made features on non-conducting substrate.

The cluster assembly method described in this section makes use of oxidised silicon V-grooves as the template elements [Partridge et al., 2003b]. Briefly, the V-grooves are etched into silicon wafers (see Figure 1.6) using an anisotropic KOH etch. Preformed lithographically defined electrical contacts on either side of the V-groove ensure that the wire is self-contacting, thereby allowing its conductance to be monitored as it is formed. The formation of the nanowires at the bottom of the V-groove is by self-assembly [Partridge et al., 2003a]. Self-assembly between electrical contacts is essential to the measurements of FCFs in bismuth cluster devices.

The flow of the inert gas used to assist in the aggregation of the clusters also determines the average velocity of the clusters leaving the source chamber. It was found that the formation of wires at the apex of the V-grooves is momentum related and therefore depends on the inert gas flow. A model of bouncing and sliding on the surface has been introduced to describe the observed dependence on the cluster velocity [Partridge et al., 2004]. Clusters of certain velocities can bounce off the substrate [Awasthi et al., 2006].

The assembly between electrical contacts allows for monitoring of the conductance of the forming wire. Once a wire was formed, a sharp onset in conduction was seen [Partridge et al., 2003b] and the deposition was stopped. The wires formed using this method were found to show Ohmic conduction.

Using V-grooves as templates for wires is preferable to the percolating film method. However, this method would be not suitable for the proposed FCF measurements either. For V-groove templated wires the contact separation demonstrated by Partridge et al. [Partridge et al., 2003a] is too large. In addition, the V-grooves formed prior to the deposition were around $2\ \mu\text{m}$ to $5\ \mu\text{m}$ wide, which results in bismuth wires of up to $0.5\ \mu\text{m}$ wide. For the proposed devices to measure FCFs contact separations of $\sim 100\ \text{nm}$ and wire widths of the same order are preferred.

1.5 Research Outline

Following the success of making bismuth cluster nanowires either with the percolating film method or the V-groove template method described previously (Section 1.4), the aim was set to further investigate bismuth cluster assembled devices. Both of the presented previous methods have their respective advantages and flaws. Using percolating films, short wires can be produced which can be only as wide as one cluster. This comes with the disadvantage that the position of this wire can not be chosen and even more than one wire could randomly form. With the V-groove template technique only one wire could be electrically contacted and measured. Due to the processing of the V-groove template the width and the length of the cluster wire formed were very large.

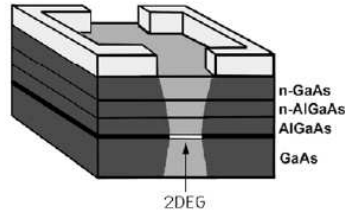


Figure 1.7: The semiconductor billiard schematically.

This research is set out to investigate a different template technique to assemble bismuth clusters between electrical contacts by combining certain aspects of the percolating film method and the V-groove template method. The aim is to assemble bismuth clusters between closely spaced electrical contacts just like the percolating film method. However, the widths of the contact fingers will be narrowed and a template (to be specified below) will be formed on top of the electrodes.

Advanced optical lithography can produce features having scales of $< 1 \mu\text{m}$. Using electron beam lithography it is possible to achieve even smaller scales. Contact fingers can be formed with a contact separation of $\sim 100 \text{ nm}$. Similar to the optical lithography, subsequent layers can be precisely aligned on top of each other (just with much more precision). Having achieved a small enough contact separation now only a template similar to the V-groove is needed on top of the contacts. Once again using electron lithography an opening in a passivation top layer can be created right above the contacts, hence creating the template. Polymethyl methacrylate (PMMA) is a nonconducting polymer used in electron beam lithography. Once exposed to an electron beam it can be developed and removed forming an opening within.

Summarising all the above, the aim of this research is to produce bismuth cluster self assembled nanoscale wires within a template between electrical contacts separated by just a few 100 nm using a newly built and commissioned UHV-compatible cluster apparatus [Reichel et al., 2006b]. This research led to a novel way of fabricating cluster assembled devices [Reichel et al., 2006a]. Furthermore, the devices can show fractal conductance fluctuations. Details on the design of the new cluster apparatus used to produce bismuth cluster assembled devices can be found in Chapter 2. Chapter 3 gives details on how this new apparatus is utilised. The investigation on the cluster assembly is presented in Chapter 5. Before presenting a sample concept design, the theory of fractal conductance fluctuation is explained in the following section (Section 1.6).

1.6 Fractal Conductance Fluctuations

1.6.1 Introduction

For very small electronic devices, the device boundaries become important. The semiconductor ‘billiard’ is one dramatic example of this concept, where the electronic behaviour is dominated by the scattering off the device walls. A semiconductor ‘billiard’ is a AlGaAs/GaAs heterostructure where the walls of the billiard are defined through gate patterns on top enclosing an area shaped like a billiard table (see Figure 1.7). Traditionally current flow could be described as a classical diffusion process of electrons, which no longer holds for sub-micron distances. Instead, electrons are thought to move along well-defined ballistic trajectories. Electron billiards offer a rare opportunity to experimentally investigate a classically chaotic system in the transition from classical to quantum behaviour (quantum chaos) [Berry, 1987; Gutzwiller, 1990; Nakamura, 1993].

Traditionally the parameter S , which is the ratio of the billiard dimension L and the electron Fermi wavelength λ , is used to distinguish between the semi-classical regime, where S is of the order of 30, and quantum mechanical regime, where S is small. Classical behaviour is assumed for frequent inelastic electron scattering, which limits the wave coherence of electrons.

Cooling down to milli-Kelvin temperatures reduces the electron scattering effects and the electrons maintain phase coherence whilst traversing the billiard. This results in quantum interference of the electron waves travelling along the different classical trajectories. Tuning a small magnetic field (or applying an electrostatic potential) and this interference manifests itself as fluctuations of the conductance. The resulting fluctuations are sensitive to the precise microscopic electron scattering configuration [Beenakker and van Houten, 1991]. An interesting feature of the fluctuations in those billiards is the occurrence of fractals [Taylor et al., 1997; Fromhold, 1997].

FCFs can be linked to the semi-classical transport regime [Jalabert et al., 1990; Baranger et al., 1993; Ketzmerick, 1996; Sachrajda et al., 1998]. In contrast, fully classical or fully quantum transport is not predicted to produce fractal fluctuations. Nevertheless, a systematically survey [Micolich et al., 2001] showed the fractal properties of conductance fluctuations in a gradual transition from the classical to the quantum regime. The conductance fluctuations extend across the spectrum of classical, semi-classical and quantum conduction regime. FCFs are a generic property of the billiard. Further, it was shown [Micolich et al., 2002] that FCFs are insensitive to the properties of the walls of the system and depend only on one parameter Q (discussed below) independent to the profile of the billiard (see Section 1.6.3). Moreover, in arrays of electron billiards, this insensitivity to wall properties also appears. Fractal properties evolve smoothly with temperature, device area, material quality and billiard openings.

1.6.2 About Fractals

Fractals are characterized by their fractal dimension D , which quantifies the scaling relationship between patterns ($L1$ and $L2$) — their length or area — observed at different scales ($S1$ and $S2$) [Mandelbrot, 1977; Gouyet, 1996].

$$D = \frac{\log(L2/L1)}{\log(S1/S2)}. \quad (1.7)$$

Non-fractal patterns have integer values for D (1 for a smooth line, 2 for a completely filled area). For a fractal pattern, however, D has a fractional value lying between 1 and 2. For even more complex structures, the D value moves closer to 2 [Mandelbrot, 1977; Gouyet, 1996].

There are two different forms of fractal behaviour: exact self-affinity, where the patterns observed repeat exactly at increasingly fine scales and statistical self-affinity, where the patterns follow the same statistical relationship at different scales. Although, exact self-affinity occupied the mind of many mathematicians over the last hundred years observations in nature are rare. However, many structures in nature show statistical self-affinity, like clouds, coastlines, or fern leaves.

Analyzing the scaling properties of the magnetoconductance of semiconductor billiards [Taylor et al., 2001], it was shown that $1 < D < 2$, as required for fractal behaviour. To determine the fractal dimension D of magnetoconductance traces a box-counting technique can be used [Mandelbrot, 1977; Gouyet, 1996; Taylor et al., 2001]. A mesh of identical squares is placed over the trace. Evaluating which squares are occupied by the trace and which are empty determines the statistical qualities of the fluctuation patterns. Different magnifications can be achieved by reducing the square size in the mesh. For fractal behaviour, the number of occupied squares in the mesh, $N(\Delta B)$, as a function of square size ΔB scales according to $N(\Delta B) \sim \Delta B^{-D}$ with $1 < D < 2$. Or in other words the scaling plot (Figure 1.8) $-\log N(\Delta B)$ against $\log \Delta B$ is a straight line and the gradient is the fractal dimension D .

In Figure 1.8 the range of fractal behaviour from ΔB_2 and ΔB_3 is about 2 orders of magnitude. The average range over which natural fractal phenomena are observed is only 1.3 orders of magnitude [Avnir et al., 1998]. The typical observation range for fractal behaviour in semiconductor AlGaAs/GaAs electron billiards is 2.5 orders [Taylor et al., 2001], well in excess of typical observations in other physical systems.

1.6.3 When Fractal becomes Non-Fractal

The original theory of FCFs [Ketzmerick, 1996] predicted that they could only be observed in the semi-classical regime of electron transport, where the billiard

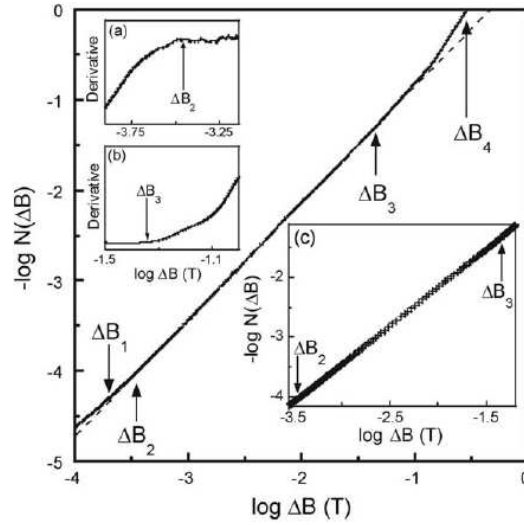


Figure 1.8: The scaling plot for an empty billiard. The data (solid) follows a straight line (dashed line) between the magnetic field scales ΔB_2 and ΔB_3 . Insets (a) and (b) are the derivative plots of the data and (c) shows the individual data points. [Micolich et al., 2001]

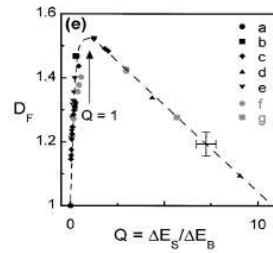


Figure 1.9: D is plotted against Q . The lines joining the data are guides to the eye. The error bars correspond to the maximum possible uncertainties in D and Q . [Micolich et al., 2001]

dimension L is of the order of 30 times larger than the electron Fermi wavelength λ (typically 40 nm for AlGaAs/GaAs semiconductor billiards). Changing the area A enclosed by the billiard or temperature T changes the character of electron transport. Decreasing A (which means decreasing S) leads to purely quantum mechanical transport processes. On the other hand, increasing T , and thereby reducing the wave coherence time of electrons, leads to conduction that is more classical. In both limits FCFs were expected to be absent.

However, recent experiments, under conditions that allowed mapping out transitions from the semi-classical regime to both the classical and quantum extremes, showed behaviour quite distinct from this expectation [Sachrajda et al., 1998]. For as long as fluctuations could be observed the fluctuations did not lose their fractal character. Instead, a smooth evolution in the fractal scaling properties was observed (D value decreases slowly towards 1).

In addition, D does not depend in a simple manner on S , or on the billiard shape, or on the location of the entrance and exit openings. Instead, D depends only on the resolution of electronic states inside the billiard, as described by a

parameter Q (Figure 1.9), which was empirically found as the ratio of the energy level spacing ΔE_S to the average energy broadening ΔE_B [Micolich et al., 2001].

$$Q = \frac{\Delta E_S}{\Delta E_B} = \frac{(2\pi\hbar^2)/(m^*A)}{\sqrt{(\hbar^2/\tau_q) + (k_B T)^2}} \quad (1.8)$$

Dividing the energy of the highest occupied level (the Fermi energy) by the total number of occupied energy levels is the energy level spacing ΔE_S , with A the area of the billiard, and m^* denoting the electron effective mass. The average energy broadening ΔE_B is given by the quadrature summation of thermal broadening $k_B T$ (with the Boltzmann constant k_B and temperature T) and the intrinsic energy level broadening \hbar/τ_q originating from the limited lifetime or phase coherence time τ_q of the quantum states due to phase-breaking scattering. Variations in material quality and the width of the openings were found simply to depend on Q through τ_q (phase coherence time) and hence ΔE_B [Sachrajda et al., 1998].

1.6.4 Sample Design and Problems

The semiconductor billiards used to investigate FCFs were defined using surface gate technology [Taylor, 1994]. Figure 1.7 shows schematically the semiconductor billiard. Within a AlGaAs/GaAs heterostructure a two dimensional sheet of electrons is located at the interface between the GaAs and the AlGaAs layers. The two-dimensional electron gas (2DEG) is the active region for the billiard. Gate patterns are deposited onto the heterostructure using standard ‘top-down’ fabrication techniques. Applying a negative bias to the gates then defines the depletion region and therefore the walls and consequently size as well as the shape of the billiard. As can be seen in Figure 1.7 exit and entrance openings in the gates allow the flow of electrons through the billiard.

The reason for using the semiconductor billiard is the large Fermi wavelength of around 40 nm (at low temperatures). This however comes with the trade-off of dopants and impurities within the semiconductor limiting the mean free path of electrons. To ensure FCFs can be observed high purity systems have to be used. Another reason to use semiconductors is the small effective mass.

Typically, the active area of the semiconductor billiard is about 1 μm . This is due to the fabrication limits of the ‘top-down’ approach in forming the gate patterns. The large area of the billiard means that experiments have to be performed at very low temperatures. This is to ensure the phase coherence of the electron wave. Furthermore, the surface gate technology is limited to the GaAs family of heterostructure system. The changeover of the existing technology to a different system using the properties of new materials is problematic.

1.7 Bismuth Clusters and FCFs

1.7.1 Introduction

According to the definition of Q (Equation 1.8) scaling in temperature and system size means that conduction (as a function of an electric field applied to a gate) of cavities smaller than 150 nm should be dominated by fractal fluctuations even at room temperature for semiconductor billiards. However, devices small enough to investigate this behaviour are difficult to fabricate with the above ‘top-down’ approach.

Dimensions of less than 150 nm can be achieved instantly using bismuth clusters having dimensions of about 30 nm to 40 nm. This ‘bottom-up’ approach achieves nanoscale resolution. In addition, the interesting and unique properties of bismuth (small effective mass, long mean free path and high Fermi wavelength) make it an ideal candidate for investigation of FCFs.

Bismuth clusters offer a rare opportunity to study chaotic effects in much smaller nanoscale devices, but it is difficult to define devices with just one bismuth cluster. Usually, more than one cluster will bridge the gap between two electrodes. It was shown [Micolich et al., 2002] that the fractal effect is insensitive to the walls of the cavity. This insensitivity to the way the cavity is formed means that conductance through any small region with an entrance and an exit should exhibit the effect of interest; shape does not matter. Theoretical studies of arrays of three billiards [Micolich et al., 2002] have shown that the three billiards act as individual billiards and that the area, which appears in Equation 1.8, is the area of one billiard. Using a gate voltage to open up the connection between the billiards, a transition occurred where the billiards acted as one big billiard. The area in Q is then the area of all billiards combined. Bismuth clusters deposited in between electrodes resemble chains or arrays of billiards.

Furthermore, it has now been shown that the fractal effect occurs not just in the ballistic but also in the diffusive scattering regime [Taylor et al., 2004]. Therefore, it should occur not only in systems where scattering is minimized (like semiconductor devices), but also in a range of different nanostructures. For instance disordered arrangements of bismuth clusters should allow the observation of FCFs.

1.7.2 Proposed Sample Design

The previous section justified the use of bismuth clusters for the investigation of FCFs. The following explains what such a sample would look like in order to study FCFs using clusters. For comparable experiments to the study of FCFs in semiconducting billiards it is advantageous to contact only a small number of bismuth clusters. The proposed way of forming FCF bismuth devices is the

deposition of bismuth clusters in between two electrodes separated by a very small gap.

Whereas it is uncomplicated to achieve separations of $1\ \mu\text{m}$ using optical lithography, contact separations in the size range of bismuth clusters (30 - 40 nm) is only achievable using electron beam lithography. Electron beam lithography however has the disadvantage that it is a serial process and therefore much slower. It is desirable to use a combination of optical lithography and electron beam lithography for the large scale contacts and the small scale contacts respectively.

Since the preparation time of just one FCF bismuth device per sample is relatively long, it is desirable to have a large numbers of such devices per sample. Previously prepared samples (Section 1.4) could have up to 10 contact pads per sample, which will be the same for the new design of the FCF samples, since the optical pattern previously is the same as for the new design. Two of the contacts are used to connect to a backgate, which leaves eight contacts for the devices. If one pair of contacts was used per active device, this would be four devices per sample.

The sample will have a backgate since gate measurements can be performed in situ. Even though the studies of FCFs in semiconductor billiards were performed by applying a magnetic field and monitoring the magnetoconductance, FCFs are predicted to occur for variation in a applied electric field (as a gate) as well.

Only clusters which are positioned in the small gap between the small scale electrodes should take part in the conduction. The rest of the sample has to be electrically passivated. This is to eliminate stray conduction paths elsewhere. For the passivation, the samples are covered with PMMA and on top of the electrodes small windows are exposed for bismuth clusters to form a connection between the electrodes. The height of the polymer is sufficient to ensure that no stray connection can occur. More on the sample design and details on the preparation can be found in Chapter 4.

1.8 Contact Issues

As shown in the previous section (Section 1.7.2), bismuth clusters are intended to be contacted to metal electrodes. This means a junction exists between the bismuth cluster ensemble and a contact electrode material. The following reviews the known contact case of a Schottky diode for semiconductors and then proceeds to the bismuth-gold junction.

1.8.1 Schottky Diode

The Schottky diode is a device that makes use of the rectifying Schottky barrier in a metal-semiconductor junction diode [Sze, 1985]. Only the majority carriers with a charge q and an effective mass m^* take part in the current transport

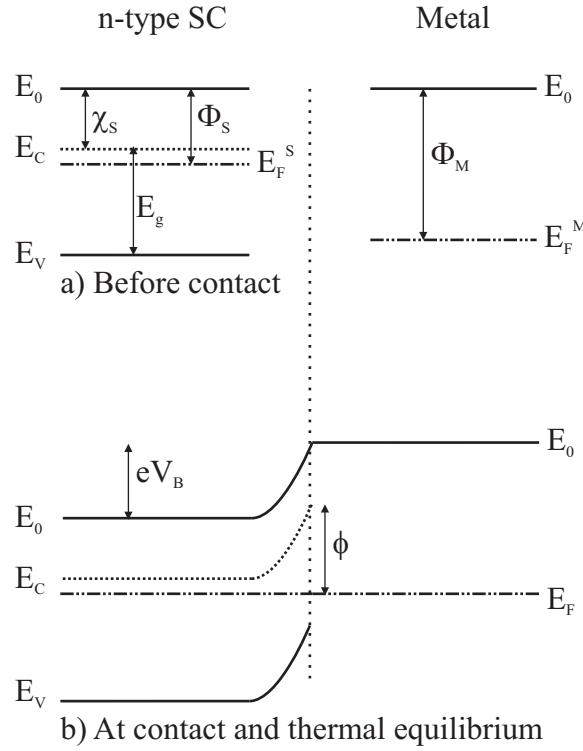


Figure 1.10: Formation of a Schottky barrier for an n-type semiconductor and metal.

which means fast switching is possible. The Schottky diode is widely used in high frequency applications. Whether or not a Schottky barrier forms depends on the work function of the metal, the band gap of the intrinsic semiconductor and the type and concentration of dopants in the semiconductor.

The Schottky barrier ϕ_B for a metal with a workfunction Φ_M and an n-type semiconductor having an electron affinity χ (see Figure 1.10) is given as

$$\phi_B = \Phi_M - \chi. \quad (1.9)$$

For a junction between a metal and a p-type semiconductor the barrier height is given as

$$\phi_B = \frac{E_g}{q} + \chi - \Phi_M, \quad (1.10)$$

with the semiconductor band gap E_g .

The current through a metal-semiconductor Schottky barrier is due to three distinct mechanisms [Van Zeghbroeck, 2006]. Firstly, there is the diffusion current of carriers from the semiconductor into the metal and secondly the current which is due to thermionic emission of high energy carriers. Both can be written as

$$J = q v N_c \exp\left(-\frac{\phi_B}{V_t}\right) \left(\exp\left(\frac{V}{V_t}\right) - 1\right), \quad (1.11)$$

which is a function of the density of carriers N_c next to the interface and a characteristic velocity. $V_t = kT/q$ is the thermal voltage. For the diffusion current, the velocity v equals the carrier mobility times the electric field at the interface between the metal and the semiconductor. In the case of thermionic current, the velocity is the Richardson velocity v_R

$$v_R = \sqrt{\frac{kT}{2\pi m}}, \quad (1.12)$$

which can be understood as the average velocity with which the carriers approach the metal semiconductor interface. The third component of current in a metal-semiconductor Schottky barrier is the current due to tunnelling through a barrier of length L

$$J = q v_R n \Theta. \quad (1.13)$$

Here, n is the density of all available carriers. Θ is the tunnelling probability and can be expressed as

$$\Theta = \exp\left(-\frac{4}{3} \frac{\sqrt{2q m^*}}{\hbar} \phi_B^{1/2} L\right). \quad (1.14)$$

Usually only one of the three current mechanism dominates.

1.8.2 Bismuth-Metal Contacts

A Schottky barrier can form when a semiconductor and a metal are brought into contact. Bismuth however is not a semiconductor and on the other hand is not a ‘normal’ metal either. The following describes the case when a bismuth semimetal (bulk material) is brought into contact with a gold metal electrode in analogy to the Schottky diode. Gold was chosen since it is a typical metal used when forming electric contacts.

Figure 1.11 shows schematically the formation of a bismuth-gold contact. When bismuth and gold are brought into contact, the Fermi levels equalize and band bending of the bismuth valence band and conduction band occurs at the interface. Unlike other metals, in bismuth the bottom of the conduction band is close to the Fermi level (0.023 eV [Dinger and W., 1972; Isaacson and Williams, 1969]). The band bending for a bismuth-gold junction however is around 0.88 eV due to the difference in the workfunctions (workfunction of gold 5.1 eV and workfunction for bismuth is 4.22 eV [Stöcker, 1994]). This is the built-in potential eV_B . A barrier φ for electrons of 0.85 eV is formed at the interface which equals the built-in potential minus the difference between Fermi level and conduction band in bismuth. No such barrier exists for the holes.

The bismuth-gold contact therefore resembles a case not unlike the previously presented Schottky diode (Figure 1.10). Here, as well as for the Schottky diode, a barrier for the transport of electrons is formed at the interface. Bismuth is a

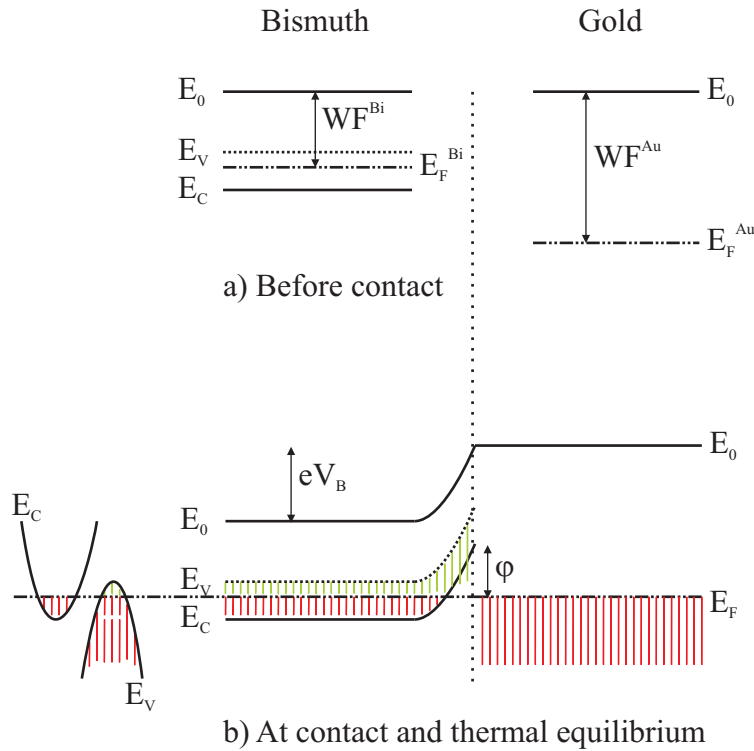


Figure 1.11: Band diagram for a semimetal bismuth and gold contact before (a) and after contact (b).

semimetal with equal number of electrons and holes. Now even though a barrier for the electrons exists, the absence of a barrier for the holes still allows current to flow across the junction even without an applied voltage to reach equilibrium.

Applying a negative voltage to the bismuth decreases the effective barrier until eventually the barrier is overcome. In the case of previously mentioned bismuth cluster device, contact to an electrode is made on either side of the active bismuth device. This means two bismuth-gold junctions are connected back to back across the same current path. Now applying a voltage means that even though the barrier on one side is lowered, the other side will see the barrier increased.

1.9 Tunnelling Conduction

The contact area over which a connection is made from a bismuth cluster ensemble to the test circuit is very small (one cluster diameter). In addition, the existence of an oxide shell around one cluster or the existence of an oxide barrier at one of the contacts can not be neglected. The chance that tunnelling conduction occurs through bismuth cluster contacts is assisted by both facts. Consider a large contact area, where many clusters make contact with a metal. Not all of the clusters might exhibit the same thickness oxide shell, which means that the chance of a low barrier somewhere in that contact area is much greater. Having

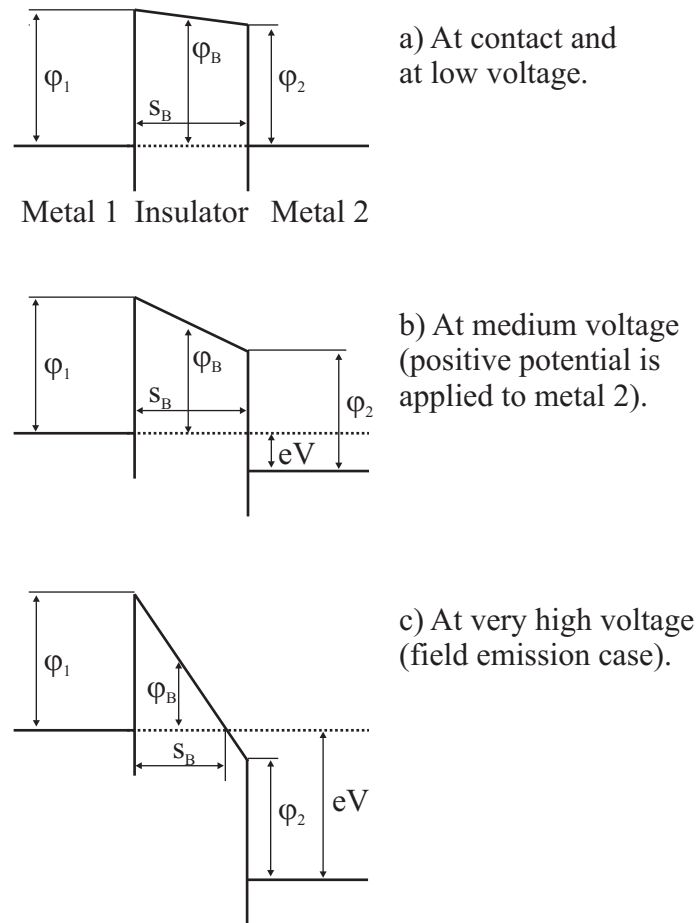


Figure 1.12: Tunnel Junction. Two different metals are separated by an insulator.

at least one low barrier (or even no barrier) at the cluster ensemble electrode interface no tunnelling conduction is observed.

1.9.1 Simmons' Theory

The following section summarizes the tunnelling theory from one metal (or electrode) through a barrier to another metal (electrode). Metal to metal tunnelling was first completely theoretically analysed by G. Simmons [Simmons, 1963b; Simmons and Unterkofler, 1963; Simmons, 1963a]. This theory is still used to explain the tunnelling conduction in scanning tunnelling microscopes. The advantage of this theory is that it allows the extraction of the barrier information like barrier height and barrier width from a fit to the current-voltage characteristics as will be explained below.

Assuming two metals (the electrodes) are separated by an insulating film, usually a metal oxide (see Figure 1.12), the current between them can only flow by means of two distinct mechanisms. Firstly, the electrons in one electrode have a high enough thermal energy to surpass the potential barrier and flow into the conduction band of the other electrode. Or, for a thin enough insulating film,

current can flow by tunnelling of electrons from one electrode to the other through the barrier. Considering $T = 0$, then only the latter effect takes place.

Simmons has shown [Simmons, 1963a] that the net current density for a generalized barrier can be written as

$$J = J_0 \left(\varphi_B \exp(-A\sqrt{\varphi_B}) - (\varphi_B + eV) \exp\left(-A\sqrt{\varphi_B - eV}\right) \right), \quad (1.15)$$

with the average barrier height relative to the negative electrode φ_B and the barrier width s_B .

$$A = \frac{2\beta s_B}{\hbar} \sqrt{2m} \quad \text{and} \quad J_0 = \frac{e}{4\pi^2 \beta^2 \hbar s_B^2},$$

wherein β is a dimensionless correction factor of order unity. Equation 1.15 can be simplified into three distinct cases depending on the applied voltage.

Small Voltages

For very small voltages $eV \simeq 0$ (Figure 1.12a) the average barrier height φ_B is independent of the applied voltage and equals the zero voltage barrier height $\varphi_0 = (\varphi_1 + \varphi_2)/2$. Then, the equation for the current density 1.15 can be simplified into

$$J = J_L V, \quad (1.16)$$

with

$$J_L = \frac{e^2 \sqrt{2m\varphi_B}}{4\pi^2 \beta \hbar^2 s_B} \exp(-A\sqrt{\varphi_B}).$$

As can be seen in Equation 1.16 the current density is a linear function of the applied voltage V . For very small voltages a tunnel junction is Ohmic.

Medium Voltages

For a medium applied voltage $eV < \varphi_0$ (Figure 1.12b) the average barrier height φ_B is given as $(\varphi_1 + \varphi_2 - eV)/2$. The current density then can be simplified to

$$J = J_L (V + \gamma V^3), \quad (1.17)$$

with

$$\gamma = \frac{(Ae)^2}{96\varphi_0} - \frac{Ae^2}{32\varphi_0^{3/2}}.$$

Strictly speaking, the expression 1.17 is valid only for β taken as unity. However, the error is of about 6% at a voltage of $eV = \varphi_0$ and decreases rapidly for voltages $eV < \varphi_0$ [Simmons, 1963a]. For $eV = 0.75 \varphi_0$ it is about 1%.

In the medium voltage case, the zero voltage barrier height and the barrier width can be found by solving Equation 1.17 for s_B and φ_0 :

$$s_B = s_0 = \hbar \left(\frac{e}{m} \right)^{1/2} \left(\frac{3\gamma}{2} \right)^{1/4} L^{1/2}, \quad (1.18)$$

$$\varphi_B = \varphi_0 = \frac{(\varphi_1 + \varphi_2)}{2} = \left(\frac{e^2}{96\gamma} \right)^{1/2} L^{1/2}, \quad (1.19)$$

with

$$L = \ln \left((96\gamma)^{1/2} \left(\frac{\hbar}{e} \right)^3 \pi^2 \frac{J_L}{m} \right).$$

High Voltages

For high applied voltages $eV > \varphi_0$ (Figure 1.12c) the average barrier height is reduced to $\varphi_1/2$ and even the barrier width is reduced to $s_B = s\varphi_1/(\varphi_1 - \varphi_2 + eV)$. Eventually, the voltage is high enough so that the Fermi level of electrode 2 is lower than the conduction band of electrode 1. In this case, tunnelling from electrode 2 in electrode 1 is not possible since there are no empty states in electrode 1 to tunnel to. As for electrons tunnelling from electrode 1 into electrode 2, all states in electrode 2 are empty. This is analog to field emission from a metal into vacuum. Then, the current density can be simplified to

$$J = \frac{e^3}{8\pi^2\hbar\beta^2} \frac{E^2}{\varphi_1} \exp \left(-\frac{2\beta\sqrt{2m}\varphi_1^{3/2}}{e\hbar E} \right), \quad (1.20)$$

with the electric field strength in the insulator $E = V/s$. For Equation 1.20 the correction factor β can no longer to be considered unity; $\beta = 23/24$ [Simmons, 1963a].

1.9.2 Further Theories on Tunnelling Junctions

There are various other theories that discuss the $I(V)$ dependence for tunnelling conductance. Only two of them will be presented here briefly since they resemble a similar case to a bismuth cluster network connected to metal electrodes.

Firstly, the theory used by Ozturk et al. [Ozturk et al., 2006] looked at the conductance of interconnected gold nanorods. The separation between two electrodes is bridged by a large number of the nanorods. It was found that the conductance through the nanorods separated by barriers is:

$$G = \frac{I}{V} = \sigma_0(T) \exp \left[\frac{eV}{N_b k_B T} \right], \quad (1.21)$$

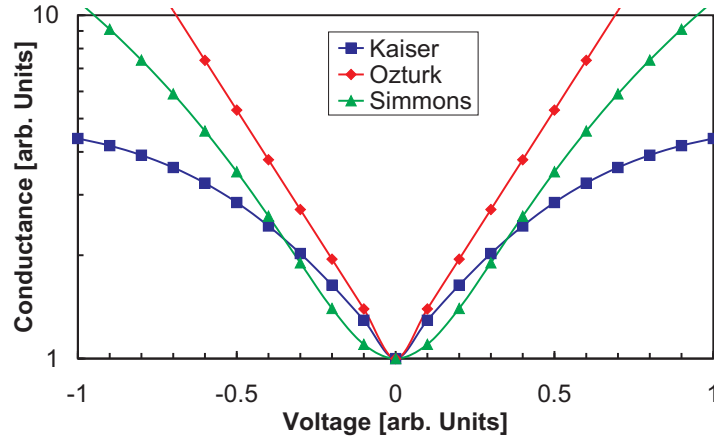


Figure 1.13: Comparison between the different theories.

where V is the applied voltage across that interconnect, N_b is the number of barriers along the length of the interconnect, $k_B T$ is the thermal energy and $\sigma_0(T)$ is the zero bias conductance. Note that N_b is not the number of nanorods forming the interconnect but much smaller. This suggested that a large number of nanorods were fused having no barrier between them.

Secondly, Kaiser et al. [Kaiser and Park, 2005] investigate conducting polymers. Here the separate ‘particles’ thought of were ‘metallic islands’ within the polymer strain between which the conductance through the polymer via tunnelling occurs. They noticed similarities (despite different conduction mechanism) for different nanoscale structures. For the observed non-linear current-voltage characteristics, a phenomenological expression has been proposed that accounted for a variety of data and was consistent with numerical calculations extending Sheng’s model [Sheng, 1980] for fluctuation assisted tunnelling. This generic expression for conductance can be written as:

$$G = \frac{I}{V} = \frac{G_0(T) \exp(V/V_0)}{1 + h [\exp(V/V_0) - 1]} \quad (1.22)$$

where $G_0(T)$ is the zero bias conductance and h is the ratio between the zero bias conductance and the saturation conductance $G_h(T)$. Similar to the theory used by Ozturk et al. [Ozturk et al., 2006], the conductance follows an exponential increase, but saturates to a fixed value G_h as $V \rightarrow \infty$.

Figure 1.13 shows a comparison of the functional form of the three theories for tunnelling conduction mentioned. The conductance is taken as $G = I/V$ with $G_0 = 1$ for all three cases. Note that for the Simmons data the medium voltage case is assumed and $\gamma = 10$. For the Ozturk and Kaiser cases V_0 is given by $V_0 = N_b k_B T = 0.3$ and the saturation in conductance for the Kaiser functional form is determined by $h = 0.2$. The conductance across a tunnelling barrier according to Simmons follows a parabolic function. According the theory used

by Ozturk et al. [Ozturk et al., 2006], the conductance increases exponentially when increasing the applied voltage. For the Kaiser case, this exponential increase is slowed and reaches a saturation conductance G_h for $V \rightarrow \infty$.

References

- Avnir, D., Biham, O., Lidar, D. A., and Malcai, O. (1998). Is the geometry of nature fractal? *Science*, 279:39.
- Awasthi, A., Hendy, S. C., Zoontjens, P., and Brown, S. A. (2006). Reentrant adhesion behavior in nanocluster deposition. *Phys. Rev. Lett.*, 97:186103.
- Baranger, H. U., Jalabert, R. A., and Stone, A. D. (1993). Weak localization and integrability in ballistic cavities. *Phys. Rev. Lett.*, 70:3876.
- Barber, D. J. and Freestone, I. C. (1990). An investigation of the origin of the colour of the lycurgus cup by analytical transmission electron microscopy. *Archaeometry*, 32(1):33.
- Beenakker, C. W. J. and van Houten, H. (1991). Quantum transport in semiconductor nanostructures. *Solid State Physics*, 44:1.
- Berry, M. V. (1987). Quantum chaology. *Proc. R. Soc. London A*, 413:183.
- Brown, S. A. (2007). URL. www.phys.canterbury.ac.nz/research/nano/.
- Busani, R., Folkers, M., and Cheshnovsky, O. (1998). Direct observation of band-gap closure in mercury clusters. *Phys. Rev. Lett.*, 81(18):3836.
- Cronin, S. B., Lin, Y. M., Black, M. R., Rabin, O., and Dresselhaus, M. S. (2002). Thermoelectric transport properties of single bismuth nanowires. In *The 21st International Conference on Thermoelectrics: ICT Symposium Proceedings, Long Beach, CA*, page 243.
- Dinger, R. J. and W., L. A. (1972). Cyclotron resonance and the cohen nonellipsoidal nonparabolic model for bismuth. III. Experimental Results. *Phys. Rev. B*, 7:5215.
- Dunbar, A. D. F., Partridge, J. G., Schulze, M., and Brown, S. A. (2004). to be published.
- Dunbar, A. D. F., Partridge, J. G., Schulze, M., and Brown, S. A. (2006). Morphological differences between Bi, Ag and Sb nano-particles and how they affect the percolation of current through nano-particle networks. *European Physical Journal D*, 39(3):415.
- Flüeli, M. (1989). *Observation des Structures Anormales de Petites Particules d'Or et d'Argent par Microscopie Electronique à Haute Résolution et Diffraction d'Electrons par un Jet d'Agrégats d'Argent*. PhD thesis, École Polytechnique Fédérale De Lausanne.

- Francis, G. M., Kuipers, L., Cleaver, J. R. A., and Palmer, R. E. (1996). Diffusion controlled growth of metallic nanoclusters at selected surface sites. *Appl. Phys. Lett.*, 79:2942.
- Fromhold, T. M. (1997). Fractal resistance in a transistor. *Nature*, 386:124.
- Gourley, S. (2002). Electronic properties of cluster deposited bismuth nanowires. Master's thesis, University of Canterbury.
- Gouyet, J. (1996). *Physics and Fractal Structures*. Springer Verlag, New York.
- Grimmett, G., editor (1989). *Percolation*. Springer Verlag.
- Gutzwiller, M. C. (1990). *Chaos in Classical and Quantum Mechanics*. Springer Verlag, New York.
- Haberland, H. (1994). *Clusters of Atoms and Molecules I*, volume 52 of *Springer Tracts in Chemical Physics*, chapter 3. Springer, Berlin.
- Hall, B. D. (1991). *An installation for the study of unsupported ultrafine particles by electron diffraction with application to silver: observation of multiply twinned particle structures*. PhD thesis, École Polytechnique Fédérale De Lausanne, Lausanne.
- Hyslop, M. (2002). *Electron diffraction studies of unsupported clusters*. PhD thesis, University of Canterbury, Christchurch.
- Isaacson, R. T. and Williams, G. A. (1969). Alfvén-wave propagation in solid-state plasmas. III. Quantum oscillations of the Fermi surface of bismuth. *Phys. Rev.*, 185:682.
- Jalabert, R. A., Baranger, H. U., and Stone, A. D. (1990). Conductance fluctuations in the ballistic regime: A probe of quantum chaos. *Phys. Rev. Lett.*, 65:2442.
- Kaiser, A. B. and Park, Y. W. (2005). Current-voltage characteristics of conducting polymers and carbon nanotubes. *Synthetic Materials*, 152:181.
- Kaufmann, M. (2006). *Electron diffraction studies of unsupported antimony clusters*. PhD thesis, University of Canterbury, Christchurch.
- Ketzmerick, R. (1996). Fractal conductance fluctuations in generic chaotic cavities. *Phys. Rev. B*, 54(15):10841.
- Kubatkin, S. E., Danilov, A., Olin, H., and Claeson, T. (2000). Anomalous Coulomb blockade in nanoconstricted quench-condensed Bi films. *Physica B*, 280:401.

- Lai, S., Guo, J., and Petrova, V. (1996). Size-dependent melting properties of small tin particles: Nanocalorimetric measurements. *Phys. Rev. Lett.*, 77:99.
- Lin, Y. M., Cronin, S. B., Ying, J. Y., and Dresselhaus, M. S. (2000a). Transport properties of Bi nanowire arrays. *Appl. Phys. Lett.*, 76(26):3944.
- Lin, Y. M., Sun, X., and Dresselhaus, M. S. (2000b). Theoretical investigation of thermoelectric transport properties of cylindrical Bi nanowires. *Phys. Rev. B*, 62(17):4610.
- Mandelbrot, B. B. (1977). *The Fractal Geometry of Nature*. W. H. Freeman and Co., New York.
- Micolich, A. P., Taylor, R. P., Davies, A. G., Bird, J. P., Newbury, R., Fromhold, T. M., Ehlert, A., Linke, H., Macks, L. D., Tribe, W. R., Linfield, E. H., Ritchie, D. A., Cooper, J., Aoyagi, Y., and Wilkinson, P. B. (2001). Evolution of fractal patterns during a classical-quantum transition. *Phys. Rev. Lett.*, 87:036802.
- Micolich, A. P., Taylor, R. P., Davies, A. G., Fromhold, T. M., Linke, H., Newbury, R., Elhert, A., Macks, L. D., Tribe, W. R., Linfield, E. H., and Ritchie, D. A. (2002). The dependence of fractal conductance fluctuations on softwall profile in a double-layer billiard. *Appl. Phys. Lett.*, 80:4381.
- Nakamura, K. (1993). *Quantum Chaos – A new Paradigm of Nonlinear Dynamics*. Cambridge University Press, Cambridge.
- Newman, M. E. J. and Ziff, R. M. (2000). Efficient monte carlo algorithm and high-precision results for percolation. *Phys. Rev. Lett.*, 85(19):4104.
- Oxford (2006). Oxford dictionary. URL. <http://www.askoxford.com>.
- Ozturk, B., Blackledge, C., Flanders, B. N., and Grischkowsky, D. R. (2006). Reproducible interconnects assembled from gold nanorods. *Appl. Phys. Lett.*, 88:073108–1.
- Partridge, J., Scott, S., Dunbar, D., Schulze, M., Brown, S. A., Wurl, A., and Blaikie, R. (2003a). Self-assembled cluster nanowires. In *Symposium on Microtechnologies for the New Millennium*, volume 411, Gran Canaria. SPIE5118.
- Partridge, J. G., Brown, S. A., Dunbar, A. D. F., Kaufmann, M., Scott, S., Schulze, M., Reichel, R., Siegert, C., and Blaikie, R. J. (2004). Template-assembled antimony cluster mesowires and nanowires. *IEEE Transactions on Nanotechnology*, 3:61.

- Partridge, J. G., Scott, S., Dunbar, A. D. F., Schulze, M., Brown, S. A., Wurl, A., and Blaikie, R. J. (2003b). Formation of electrically conducting mesoscale wires through self-assembly of atomic clusters. *IEEE Transaction on Nanotechnology*, 3(1):61.
- Reichel, R., Partridge, J. G., and Brown, S. A. (2006a). Nanoscale and microscale lithography methods and resultant devices. New Zealand Patent Application No. 541209/547784. Patent Application lodged 8 July 2006.
- Reichel, R., Partridge, J. G., Dunbar, A. D. F., Brown, S. A., Caughley, O., and Ayesh, A. (2006b). Construction and application of a uhv compatible cluster deposition system. *Journal of Nanoparticle Research*, 8:405.
- Rintoul, M. D. and Torquato, S. (1997). Precise determination of critical threshold and exponents in a three-dimensional continuum percolation model. *Journal of Physics A*, 30:L585.
- Sachrajda, A. S., Ketzmerick, R., Gould, C., Feng, Y., Kelly, P. J., Delage, A., and Wasilewski, Z. (1998). Fractal conductance fluctuations in a soft-wall stadium and a sinai billiard. *Phys. Rev. Lett.*, 80:1984.
- Schmelzer Jr., J. (2001). Finite-size effects in cluster films. Master's thesis, University of Canterbury.
- Schmelzer Jr., J., Brown, S. A., Wurl, A., Hyslop, M., and Blaikie, R. J. (2002). Finite-size effects in the conductivity of cluster assembled nanostructures. *Phys. Rev. Lett.*, 88:226802.
- Schulze, M., Gourley, S., Brown, S., Dunbar, A., Partridge, J., and Blaikie, R. J. (2003). Electrical measurements of nanoscale bismuth cluster films. *European Physical Journal D*, 24:291.
- Sheng, P. (1980). Fluctuation-induced tunneling conduction in disordered materials. *Phys. Rev. B*, 21(6):2180.
- Simmons, J. G. (1963a). Generalized formula for the electric tunnel effect between similar electrodes separated by a thin insulating film. *J. Appl. Phys.*, 34(6):1793.
- Simmons, J. G. (1963b). Low-voltage current-voltage relationship of tunnel junctions. *J. Appl. Phys.*, 34(1):238.
- Simmons, J. G. and Unterkofler, G. J. (1963). Potential barrier shape determination in tunnel junctions. *J. Appl. Phys.*, 34(6):1828.
- Smith, G. E., Baraff, G. A., and Rowell, J. M. (1964). Effective g factor of electrons and holes in bismuth. *Phys. Rev.*, 135:A1118.

- Stauffer, D. (1985). *Introduction to percolation theory*. Taylor & Francis, London.
- Stein, G. (1979). Atoms and molecules in small aggregates. *The Physics Teacher*, 17:503.
- Stöcker, H. (1994). *Taschenbuch der Physik*. Verlag Harri Deutsch, 2nd edition.
- Sze, S. M. (1985). *Semiconductor Devices*. John Wiley & Sons.
- Taylor, R. P. (1994). The role of surface gate technology for algaas/gaas nanostructures. *J. of Nanotechnology*, 5:183.
- Taylor, R. P., Martin, T., and Fromhold, T. M. (2004). Fractal conductance fluctuation in the diffusive scattering regime. *Phys. Rev. Lett.* to be submitted.
- Taylor, R. P., Micolich, A. P., Newbury, R., Fromhold, T. M., Ehlert, A., Davies, A. G., Macks, L. D., Trench, C. R., Bird, J. P., Linke, H., Tribe, W. R., Linfield, E. H., and Ritchie, D. A. (2001). Semiconductor billiards - a controlled environment to study fractals. *Physica Scripta*, T90:41.
- Taylor, R. P., Newbury, R., Sachrajda, A. S., Feng, Y., Coleridge, P. T., Dettmann, N., Zhu, N., Gou, H., Delage, A., Kelly, P., and Wasilewski, Z. (1997). Self-similar magnetoresistance of a semiconductor sinai billiard. *Phys. Rev. Lett.*, 78:1952.
- Tian, Y., Meng, G., Biswas, S. K., Ajayan, P. M., Sun, S., and Zhang, L. (2004). Y-branched Bi nanowires with metal-semiconductor junction behaviour. *Appl. Phys. Lett.*, 85(6):967.
- Tian, Y. T., Meng, G. M., Phillips, F., H., S. S., and Zhang, L. D. (2006). Step-shaped bismuth nanowires with metal-semiconductor junction characteristics. *Nanotechnology*, 17:1041.
- Van Zeghbroeck, B. (2006). Principles of semiconductor devices. URL. <http://ece-www.colorado.edu/~bart/book/contents.htm>.
- VEECO (2006). URL. www.veeco.com.
- WebElements Ltd (2006). Webelements periodic table of the elements. URL. www.webelements.com.
- Wurl, A. (2003). *Electron diffraction studies of unsupported bismuth clusters*. PhD thesis, University of Canterbury.

Design of a UHV-Compatible Cluster Apparatus

This chapter provides a complete description of the ultra high vacuum (UHV) compatible cluster apparatus that was built and commissioned during this PhD thesis. The characterization and testing of this system follows in Chapter 3.

2.1 Introduction

Previously, cluster sources [Ganteför et al., 1990] were mainly dedicated to gas phase studies of cluster properties. It is only relatively recently that systems have been designed to facilitate cluster deposition in order to study the properties of clusters on surfaces. Goldby et al. [Goldby et al., 1997] designed a UHV cluster source for the deposition of mass-selected metal clusters with controlled landing energy. Baker et al. [Baker et al., 1997] developed a system for in-situ studies such as scanning tunnelling microscopy or synchrotron radiation experiments. To date there has been no report in the literature of a cluster deposition system specifically designed and optimised for the fabrication of cluster-assembled nano devices.

Our UHV-compatible cluster apparatus consists of four different stages as illustrated in Figure 2.1. The first stage is the source, where formation of clusters takes place assisted by a stream of inert gas. In our cluster apparatus, two interchangeable cluster sources are available; an Inert Gas Aggregation Source (IGA) and Magnetron Sputtering Source. See Section 2.2 for design of both types of cluster sources. Sections 3.3 and 3.4 have details on the modes of operation for the IGA and Magnetron Sputter Source respectively. The second stage is a differential pumping system that is used to remove excess gas and to form a molecular beam of clusters. In the third stage, clusters can be size selected using a mass-selection system [von Issendorff and Palmer, 1999]. Finally, in the deposition

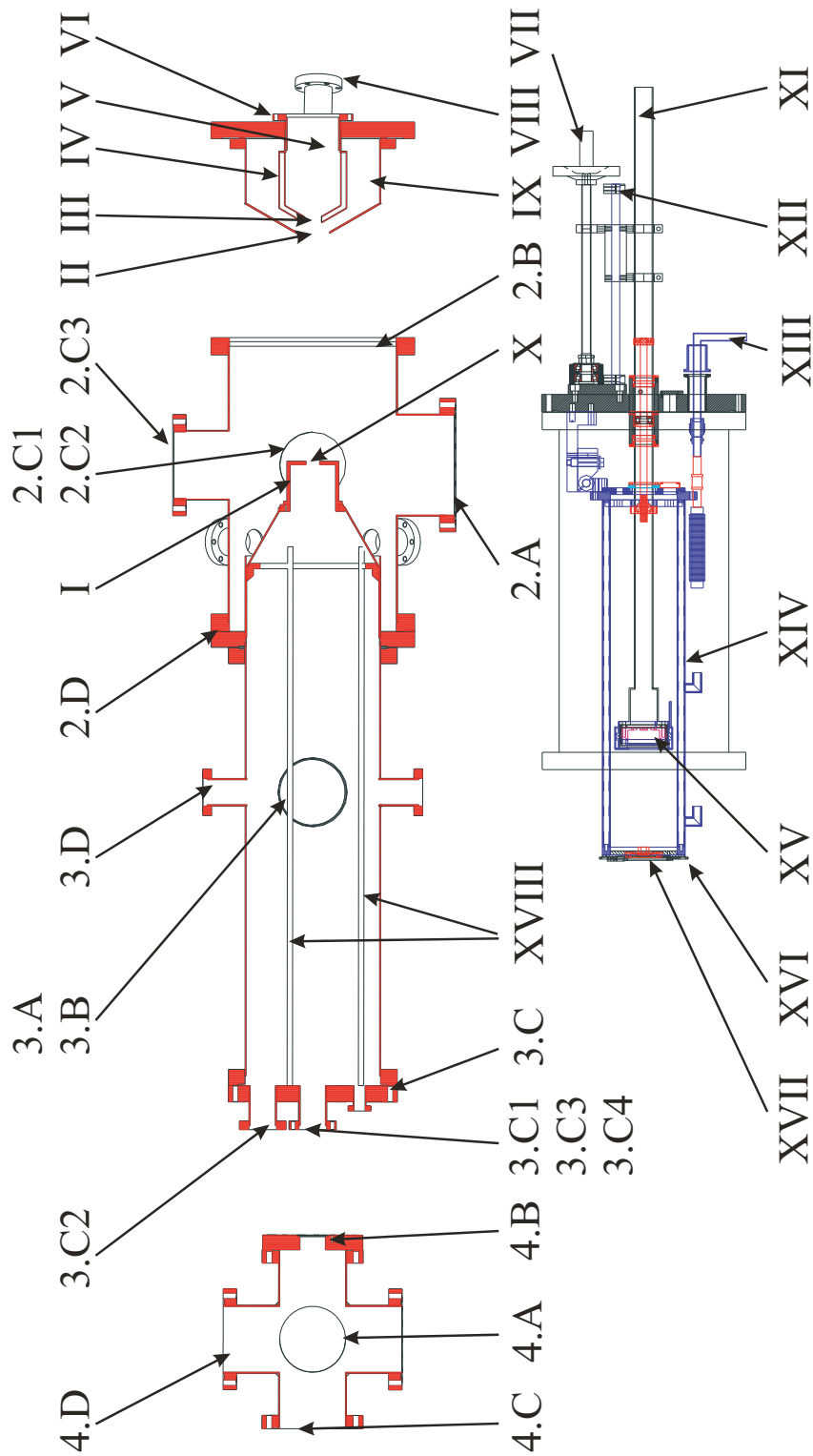


Figure 2.1: Schematic drawing of the UHV-compatible Cluster Apparatus with two interchangeable cluster sources. The labels are explained and used throughout the text.

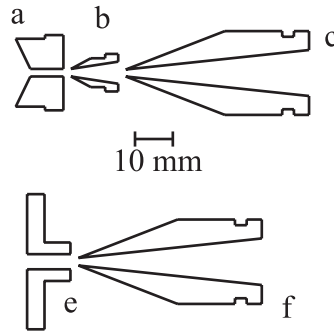


Figure 2.2: Schematic of size and shape for the nozzles used with the Inert Gas Aggregation in the case of Antimony (nozzles [a], [b] and [c]) and used with the Magnetron Sputter Source (nozzles [e], [f] and [c]).

chamber or fourth stage, the beam of clusters is directed towards an electrically contacted sample.

The clusters are entrained in a beam from the source through the mass filter (Section 2.4) into the deposition chamber and are deposited onto electrically contacted samples (Section 2.5). The provision of electrical feedthroughs and a cryostat (Section 2.5.1) for device characterisation are a key feature of the present system. The apparatus provides high deposition rates, large beam spots, size selection and cluster size characterisation, and a high degree of flexibility in terms of positioning of different elements in the system and types of sources available (Section 2.6).

The emphasis in this research group is on the production of relatively high fluxes of clusters, since the intention is that the deposition times should be short so that (ultimately) large numbers of devices can be made in a day. The focus is currently on relatively large clusters since the devices that the clusters were incorporated into were defined mainly by optical lithography i.e. with contacts and other feature sizes $> 1 \mu\text{m}$ [Schmelzer Jr. et al., 2002; Partridge et al., 2003]. Cluster sizes are typically 20-40 nm diameter using the IGA source and $> 3 \text{ nm}$ mean diameter using the magnetron sputter source. During this thesis electron beam lithography was used to reduce the sizes of the devices of interest, and consequently the attention shifted to clusters of smaller sizes.

In designing the system, ConFlat (CF) flanges were chosen so that after baking the system, ultimate base pressures in the ultra-high vacuum range are possible, decreasing the effects of oxidation and contamination significantly.

2.2 Cluster Source Stage

At the moment, two interchangeable sources are available. An inert gas aggregation source (IGA), relying on thermal evaporation, provides a fast and reliable way of producing high flux cluster beams of low melting point materials. A mag-

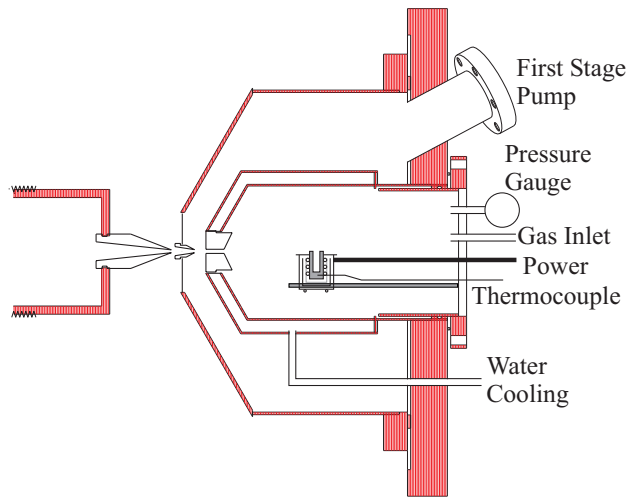


Figure 2.3: Schematic and nozzle placement for the inert gas aggregation source.

neutron sputtering source, combining magnetron sputtering and gas condensation, generates clusters from higher melting point materials (including semiconducting materials). The design also allows the future addition of other kinds of sources e.g. PACIS (Pulse Arc Cluster Ion Source) [de Heer, 1993; Ganteför et al., 1990] and laser vaporisation [Ganteför et al., 1990]. Design details of IGA and magnetron sputter source are discussed below. The details on the modes of operation for the IGA and magnetron sputter source can be found in Sections 3.3 and 3.4 respectively.

2.2.1 Inert Gas Aggregation Source

Figure 2.3 shows schematically the inert gas aggregation source. The inert gas aggregation source consists of two chambers, a source and an outer, additional pumping stage, separated by a barrel-shaped aperture (nozzle [a] in Figure 2.2). The walls of the inner chamber are cooled with water. This design [Hall, 1991; Yokozeki and Stein, 1978; Flüeli, 1989] has successfully been used in the older high vacuum system in our group as mentioned previously (Section 1.4) to achieve deposition rates up to 1000 \AA/s .

There is no active pumping on the inner source chamber. The outer source stage is pumped with an Edwards two-stage rotary pump (E2M18) with a pumping speed of $17.0 \text{ m}^3/\text{hr}$. A skimmer-like aperture (nozzle [b] in Figure 2.2) separates the outer source stage from the second stage. Another skimmer (nozzle [c] in Figure 2.2), mounted in a threaded holder, separates the second stage from the third stage. The 10 mm long thread allows precise adjustment of the distance between the second and third aperture. By un-tightening of the thread, the tip of the third nozzle can be brought into closer proximity to the mouth of the second nozzle. Tightening increases the separation between the third nozzle tip and second nozzle mouth.

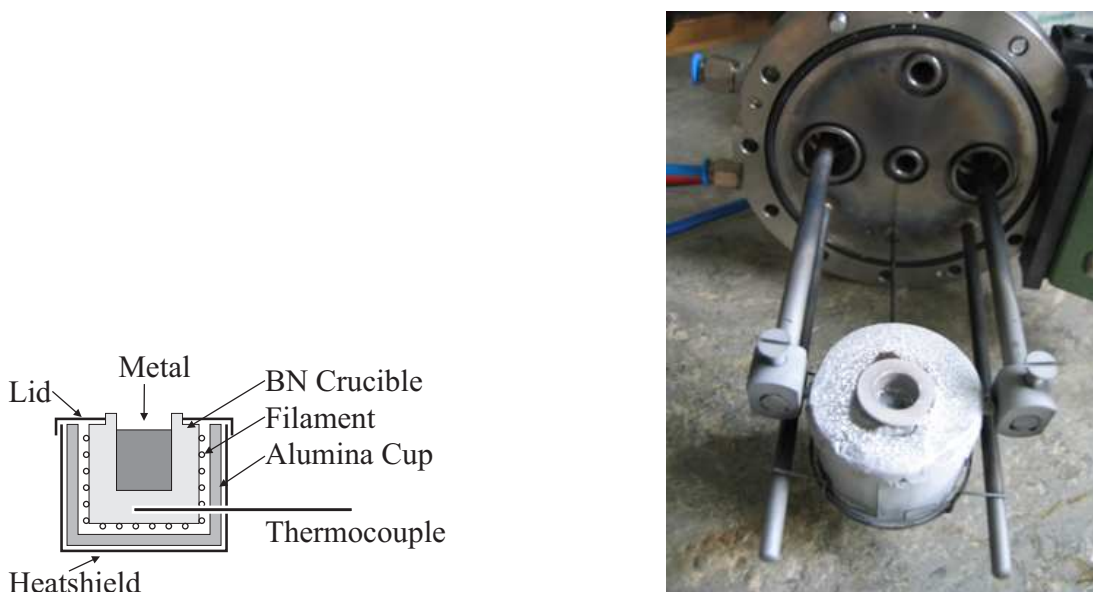


Figure 2.4: Schematic crucible design (left) used for the formation of bismuth and antimony clusters with the IGA source and crucible mounted on the source back plate (right).

Figure 2.4 shows a schematic of the assembled crucible. A boron nitride crucible filled with metal (the cluster material) is resistively heated with a tungsten filament. An alumina cup isolates the filament from the surrounding tantalum heat shield. The temperature is measured with a K-type thermocouple sitting in a hole in the boron nitride cup just underneath the hot metal. The tantalum cap on top of the heat shield fits tightly around the inner crucible preventing any material from entering the heat shield arrangement and heat loss to the source chamber.

The temperature of the crucible is controlled using a commercial temperature controller (Omega CN1601). With this particular controller and the K-type thermocouple, it is possible to set a set point between 0 and 1000 °C, and a ramp rate between 1 and 9999 °C/hr. The controller gives out a voltage between 0 and 10 V corresponding to the actual temperature and set temperature and the PID settings. The PID are proportional, integral and derivative values to determine how the set temperature is reached. The PID values can be adjusted manually or using a built in auto-tune mode. The output voltage of the temperature controller drives a HP 6259B DC power supply, which is used to heat up the crucible and the metal.

The crucible design (Figure 2.4) was used for the production of antimony and bismuth clusters. To melt the metal and produce clusters the crucible has to be heated to about 650 °C for the production of antimony clusters and to about 850 °C for the production of bismuth clusters. This means, without appropriate cooling the source chamber walls would get hot as well. As this would heat the inert gas, cooling of the metal vapour would not be sufficient to form a

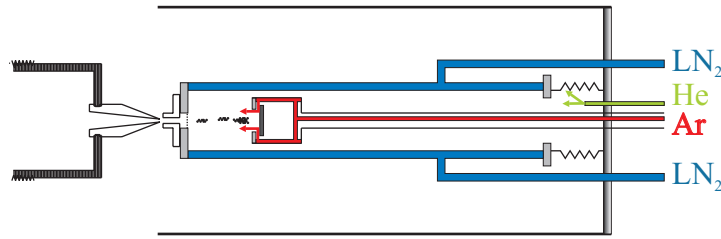


Figure 2.5: Schematically Magnetron Sputter source.

supersaturated region and therefore no cluster formation would occur. For that reason, the source chamber walls as well as the source back plate are cooled with water. The source chamber walls can also be cooled with liquid nitrogen. The water cooling around the source backplate then is to prevent the source seal (a viton o-ring) from freezing.

Two MKS 1179A mass flow controllers (one for helium and one for argon) are used to regulate the inert gas flow. A controller, made in the Electronic Workshop of the Physics and Astronomy Department at the University of Canterbury, was used to set the inert gas flow for each gas and the total flow to the desired value and measure it.

2.2.2 Magnetron Sputtering Source

Our magnetron sputter source was developed in collaboration with the group at the University of Freiburg [Haberland, 1992; Haberland et al., 1992; Haberland et al., 1993; Haberland et al., 1994]. Atoms are sputtered off a metal (or semiconducting) target by magnetron sputtering in a gas (process gas) plasma. Clusters form in the vapour above the target assisted by inert gas.

A stream of inert gas (carrier gas) carries the clusters through a variable aperture [d] (not shown in Figure 2.2). This makes it possible to adjust the pressure in the aggregation tube and has therefore an influence on cluster growth and formation. In order to achieve a more collimated beam (as later discussed in Section 3.3.3) a barrel-shaped aperture (nozzle [e] in Figure 2.2) has also been fitted on the exit side of the adjustable aperture [d]. When using the barrel aperture [e] (typically 9 mm long, 4 mm diameter), the variable aperture [d] was set to an opening of about 3 mm which was found optimal during testing. A skimmer-like aperture [c] (the same nozzle as is used for the IGA source) separates the second stage from the mass filter stage. Again, the distance between [e] and [c] can be easily changed using the threaded holder of [c].

Figure 2.5 shows schematically the design of the sputter source. The magnetron sputter source stage has no active pumping. The magnetron sputter head is operated at pressures of about 1 Torr with a mixture of argon and helium. Since typically discharge powers are around 100 to 300 W, the walls of the sputter source are cooled with liquid nitrogen. However, to prevent the seal (a viton

o-ring) on the sputter head from freezing, the sputter head is water-cooled. A variable aperture [d] at the end of the source chamber allows control of the pressure within the source. The distance between the magnetron head and this aperture can be varied. The flow control is the same as for the inert gas aggregation source.

2.3 Differential Pumping

The second stage of the UHV compatible cluster apparatus is pumped with a Pfeiffer roots pump (WKP 1000A) with a pumping speed of 1070 m³/hr, connected by an 8" CF flange [Port 2.A in Figure 2.1], and can be isolated using a pneumatically controlled gate-valve. The source stage connects to this chamber via a 12" CF flange [Port 2.B]. Three 6" CF flanges [Port 2.C1, 2.C2 and 2.C3] allow easy access to the apertures for maintenance and allow the accumulation of cluster material on the apertures to be viewed through a view port. (This window also provides an opportunity for photo-ionisation of the clusters). Additionally, there are four spare 2.75" CF flanges available on the second stage.

The differential pumping reduces the pressure from about 1 Torr in the source chamber to about 10⁻⁶ Torr in the deposition chamber by pulling away most of the excess inert gas. It also collimates the clusters into a beam. The pressures in the different stages are a function of the pumping speed, the amount and type of gas and the diameter of the apertures correspondingly.

At present, relatively large apertures (see Figure 2.2) are used to ensure large cluster fluxes. Therefore pressures in the deposition chamber are in the mid 10⁻⁶ Torr range during deposition (due to the inert gas flow), and in the low 10⁻⁷ Torr range with no gas flow (without baking the system). A discussion of how size, shape and distance of the nozzles effects the cluster formation and the shape of the beam can be found in Section 3.3.3.

2.4 Mass Selection Stage

The third (mass-selection) stage connects to the second stage via a 10" CF flange [Port 2.D]. This stage hosts the von Issendorff & Palmer mass filter [von Issendorff and Palmer, 1999]. A Pfeiffer turbo pump (TMU521) with a pumping speed of 520 l/s (for nitrogen) is connected via a 6" CF flange [Port 3.A]. It can be isolated with a pneumatically controlled gate-valve. An additional 6" CF flange [Port 3.B] allows several different options, e.g. to hold the cryostat and the sample holder, or to host a Wiley-McLaren-TOF (Time of Flight Mass spectrometer) [Wiley and McLaren, 1955]. At the end of the mass filter stage, on a 10" CF flange [Port 3.C], are four 2.75" CF flange ports. The on-axis centre port [Port 3.C1] can be used for straight-through depositions (no mass-selection of clusters); whereas the off-axis ports at the same height [Port 3.C3 and 3.C4], can be used for mass-selected

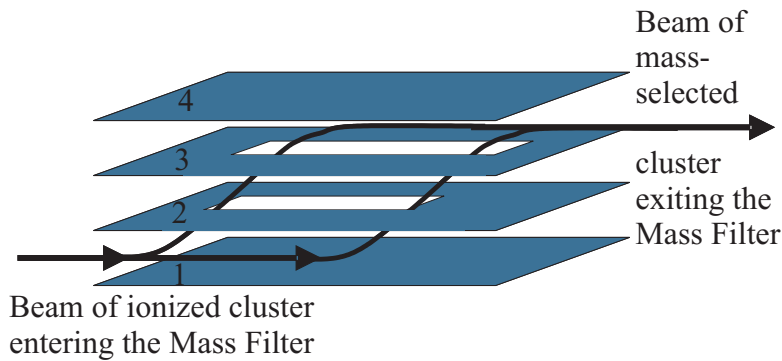


Figure 2.6: Schematic design for the von Issendorff & Palmer mass selection system.

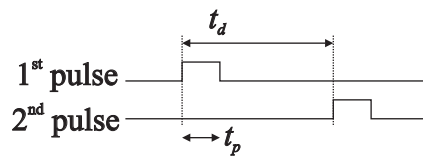


Figure 2.7: Mode of operation for the von Issendorff & Palmer mass selection. Two high voltage pulses are applied to plate 2 and plate 3 (see Figure 2.6). The timing t_d determines the masses selected.

cluster depositions. Two of the 2.75" CF flanges (ports 3.C2 and either 3.C3 or 3.C4) and three 1.33" CF flanges are used for electrical feedthroughs to the plates of the mass filter. There are two further 2.75" CF flanges available on that stage [Port 3.D], which are usually used to mount pressure gauges and/or a residual gas analyser.

2.4.1 Mass-Filter

The following is a brief introduction to the modes of operation of the mass-selection filter; details can be found elsewhere [von Issendorff and Palmer, 1999].

Figure 2.6 shows the mass filter schematically. A focussed beam of ionised clusters enters the mass filter between plate 1 and plate 2. A short high voltage pulse (t_p - pulse time — see Figure 2.7) is applied to plate 2. This accelerates the beam of clusters laterally, perpendicular to its original direction towards plate 2. To guarantee that all ions gain the same momentum and therefore all ions of the same mass will gain the same velocity perpendicular to the beam axis, the length of pulse is short enough so that no clusters can leave the acceleration region during the pulse.

The ions then drift through a field free region (between plate 2 and plate 3) and pass into the deceleration region (between plate 3 and plate 4). There a high voltage pulse is applied to plate 3 which is identical to the acceleration pulse. The time the ions need to travel from the acceleration region to the deceleration region depends on their mass. This means that the time between pulses t_d (delay time — see Figure 2.7) defines which ions will leave the mass selector through the

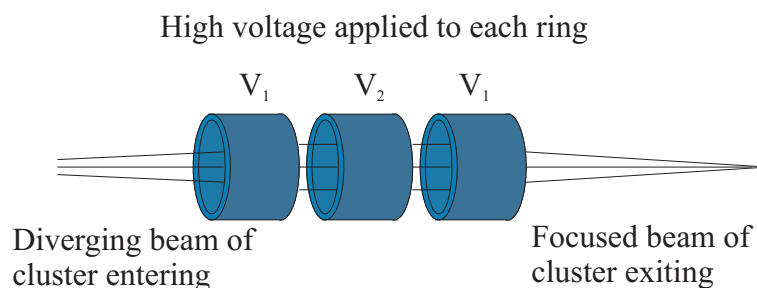


Figure 2.8: Schematically the focusing of a diverging beam of ionized clusters using einzel-lenses.

exit aperture. In practice, the selected mass is changed by varying the frequency of the pulses, while maintaining a constant ratio t_p/t_d . Ions of the selected mass lose all of their velocity perpendicular to the original beam axis and regain their original flight direction, but are now offset in position. The mass-selected ions leave the mass filter chamber through an off-axis port [Port 3.C3 or 3.C4] into the deposition chamber and onto the sample. Ions of other masses are deposited on the exit aperture or elsewhere within the system.

As soon as the acceleration region is filled with clusters again, the next acceleration pulse is applied. Thereby, a very high overall transmission can be reached with an almost continuous beam of size-selected clusters.

For measuring the overall mass spectrum of a cluster source, a faraday cup can be placed at the exit of the mass filter (at the off-axis port of the mass filter chamber). The signal strength at the faraday cup is proportional to the number of ions of the mass selected.

The previously described process needs a focussed beam of ionized clusters. Focussing the beam can be achieved by varying the nozzles and their separation between them (see Section 3.3.3) or using the einzel lenses (Figure 2.8). Two sets of einzel lenses are included i.e. on-axis in front of the entrance to the mass filter plates for focussing into the mass filter entrance and off-axis after the exit from the plates to collimate the beam of mass-selected clusters. As for the ionization, it is simplest just to use the magnetron sputter source, since it already produces charged clusters due to the efficient charge transfer processes in the sputter discharge. However, if the inert gas aggregation source is preferred, ionization with electron or photon beams is necessary.

In the present system, the von Issendorff & Palmer mass filter [von Issendorff and Palmer, 1999] is implemented with an acceleration region of 26 mm, a drift region of 30 mm and an overall length of 385 mm. The deceleration region is 26 mm, too. The mass filter plates are suspended on insulating brackets mounted on four cylindrical rods (VIII in Figure 2.1); they are mounted on the 10" CF end flange of the mass filter stage [Port 3.C]. A bevelled annulus mounted at the end of the 4 rods 'docks' with a similarly shaped plate on the inside of the chamber, allowing simple assembly and positioning of the system. Provision is made for

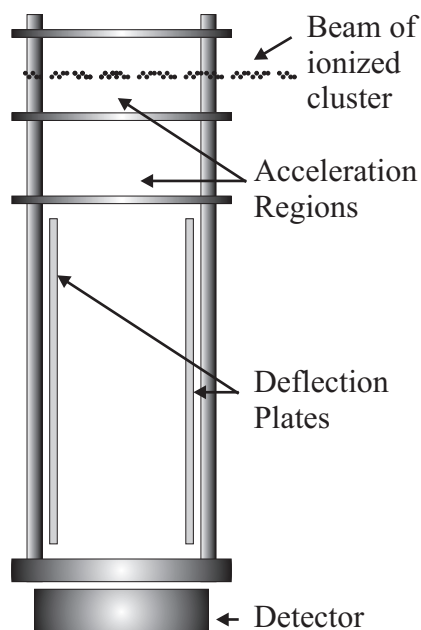


Figure 2.9: Schematically TOF.

mounting an Axial Molecular Beam Ioniser at the end of the whole assembly, so that it is positioned immediately behind the second stage skimmer. This ioniser will be used for the neutral clusters produced by the IGA source. All testing of the mass filter to date was done using ionised clusters produced in the sputtering source.

2.4.2 TOF

While the von Issendorff & Palmer mass filter is the preferred option for both deposition and characterising the cluster beam, we have found it useful to characterise the beam using a home-built TOF of the Wiley-McLaren type [Wiley and McLaren, 1955; Kaufmann, 2006], too. This TOF can be mounted on the 6" CF flange on the mass filter chamber [Port 3.B] (the von Issendorff & Palmer mass filter must be removed, of course) or on the deposition chamber [Port 4.D].

Figure 2.9 shows schematically the layout of the TOF. A beam of ionized clusters enters the TOF between the top and the middle plate. An electric field between the top and the middle plate deflects the ionised clusters towards the detector. The deflection is perpendicular to the original velocity direction of the clusters. The field also accelerates the clusters and a second acceleration region (between the middle and the bottom plate) can be used. After the acceleration, the clusters enter a drift region. Heavy clusters or very fast clusters which might not have lost all their initial velocity direction can be deflected towards the detector using the deflection plates. A more detailed description on the functionality of this particular TOF can be found elsewhere [Kaufmann, 2006].

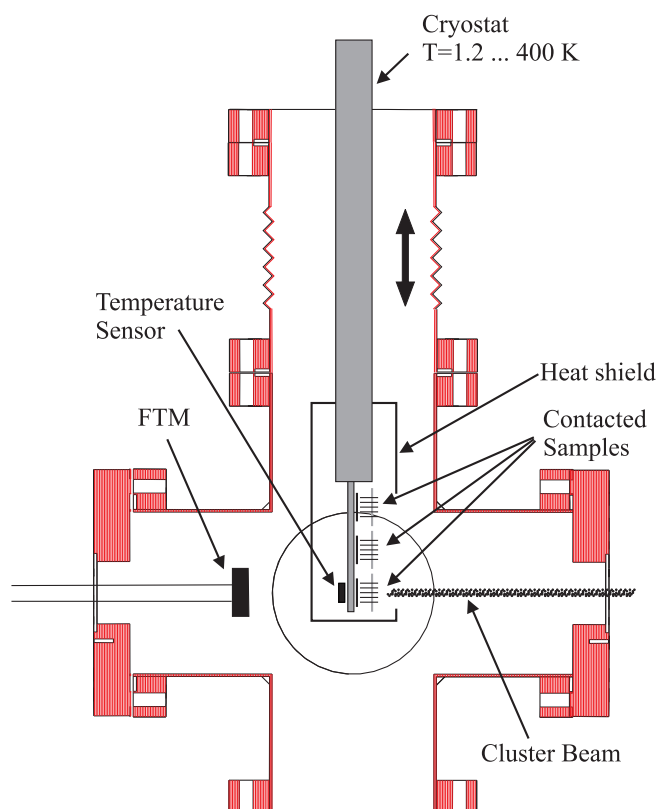


Figure 2.10: Schematic for the deposition chamber.

2.5 Sample Stage

The deposition chamber is connected to the cluster system through 2.75" CF tubes and a size-reducing flange [Port 4.B]. A 2.75" CF gate-valve allows the deposition chamber to be isolated from the rest of the system and serves as a crude shutter.

Figure 2.10 shows schematically the deposition chamber or sample stage. A 6" CF six-way cross serves as the deposition chamber. This chamber can be pumped to ultra-high vacuum and consequently cluster device assembly can occur in a very clean environment. Hence limiting water layer formation on the substrates and reducing oxidation, which was observed for cluster devices [Schulze et al., 2003] in the HV system previously used in our group. A UHV environment significantly reduces this problem.

The deposition chamber stage is pumped with a Pfeiffer turbo pump (TPH270) with a pumping speed of 270 l/s (for nitrogen) [Port 4.A]. The cluster deposition rate is monitored with a quartz crystal film thickness monitor (FTM) [Port 4.C]. A cryostat cold finger, mounted on a 6" CF translational drive with 10 cm movement range [Port 4.D], holds the samples. While monitoring the deposition rate, the sample stage is retracted and once the desired deposition rate is set, the appropriate sample is moved into the beam. There are two additional 6" CF flanges

available, e.g. to host the Wiley-McLaren TOF mass spectrometer, and to mount pressure gauges and/or a controlled leak rate gas inlet system.

A key feature of the present system is the provision of a cryostat and electrical feedthroughs to the deposition chamber. This allows the in-situ preparation of electrical device samples as well as in-situ testing of the cluster assembled devices. Electrical characterization can be done before, during and after the deposition. In addition, the cryostat allows temperature dependent electrical studies in-situ.

2.5.1 Cryostat

As can be seen in Figure 2.10, a cryostat cold finger, mounted on a translational drive, holds the samples. Therefore, they can be moved in and out of the beam. The gate valve [Port 4.B] between the mass filter stage and the deposition chamber allows the beam to be blanked while moving the samples in and out of the beam using the translational drive.

Both contacted and uncontacted samples are mounted on the cold finger of the cryostat. The cryostat used is a Janis ST400 continuous flow cryostat. Continuous flow cryostats, like this one, are a fast and flexible way of reaching low temperatures. They can be operated in any orientation (horizontal [Port 3.B] or vertical [Port 4.D]), accessing a temperature range of 1.2 K to 475 K.

Temperature stabilities of 50 milli-Kelvin can be achieved using a CryoCon Model 32 temperature controller to adjust the temperature. This controller is able to read two temperature sensors and to control two heaters at a time. Currently, a 25 Ω resistive heater is positioned at the base of the cold finger. The temperature is read using a diode at the base of the cold finger. However, the cold finger has a certain length and only the base is cooled/heated. There is a temperature gradient along the length of the cold finger. To access the temperature of the sample another diode is mounted on the backside of the cold finger at an actual sample position.

At present, the main function of the cryostat is to allow temperature-dependent electrical characterisation of cluster devices without exposing them to the atmosphere; this is important to prevent oxidation of the devices.

Figure 2.11 shows the sample holder used to electrically contact the samples during the deposition. The cryostat cold finger has three sample mounts for contacted samples. Uncontacted samples can be fitted over the whole length of the cryostat cold finger.

The contacted samples sit in an 10×10 mm² recess. Contact to each sample is made to ten spring-loaded pushpins. The pushpins are linked to a breakout box via a ten pin electrical feed through fitted on the base plate of the cryostat. The pins of the feedthrough are connected to the sample pins with ten cryogen compatible copper wires with a UHV compatible coating arranged in five twisted pairs. On the breakout box each pin is connected to a BNC plug

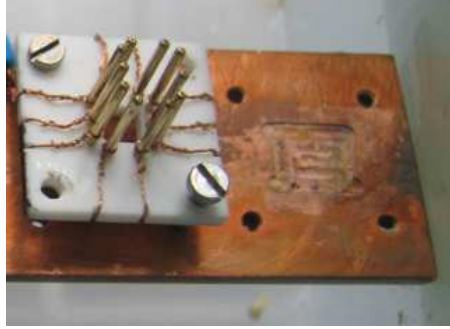


Figure 2.11: The 10 pin sample holder mounted on the cryostat cold finger.

representing one contact on the sample. The electrical measurement instruments (see Section 2.5.2) can then be linked via BNC cables to perform various different electrical measurements on the sample, i.e. electrical circuits can be set up including the cluster sample as a device. The sample mount is different to the one previously used in the HV system (Section 1.4). The choice of materials for this new sample holder means that the design of the sample mount is UHV compatible. At present, since there are three electrical feedthroughs, it is possible to have three contacted samples on the cold finger at the same time.

2.5.2 Electrical Measurements

For experiment during this thesis, clusters are deposited into lithographically defined devices. The samples can be electrically contacted during the deposition. Three contacted samples can be mounted simultaneously, allowing sequential fabrication of three devices under the same or different conditions, as desired.

Voltages for a pair of contacts are measured with Keithley 2000 multimeters and Keithley 6514 electrometers measure the current. They are connected to a computer via a GPIB interface and a Labview programme is used for data acquisition. For the onset of conduction, a constant voltage is applied and the resistance versus time is monitored. During deposition up to two pairs of independent contacts can be monitored. $I(V)$ characteristics of all devices are obtained both prior to deposition (to confirm all pairs of contacts are open circuit, i.e. have $R > G\Omega$) and once there is a connection between a set of contacts. The voltage supply used was built in the Electronic Workshop of the Physics and Astronomy Department at the University of Canterbury. It allows for constant voltage supply as well as ramped voltage supply. A triangular ramp as well as a saw-tooth ramp are available and amplitude and frequency can be chosen.

The programme for the data acquisition is also used for temperature measurement from the temperature controller. Furthermore, there are current- and voltage- amplifiers as well as Lock-In amplifiers (for frequency measurements) available.

2.6 Modes of Operation

There are several configurations of the equipment that can be used depending on the experimental requirements:

1. In the ‘standard configuration’ described previously the von Issendorff & Palmer mass filter is in place, the deposition chamber is mounted on the off-axis port [Port 3.C3 or Port 3.C4] of the mass filter stage, and mass selected clusters are deposited on samples mounted on the cryostat cold finger which is mounted on the deposition chamber [Port 4.D].
2. If a higher flux of clusters is required without mass-selection the deposition chamber can be mounted on the on-axis port [Port 3.C1] of the mass filter stage. It is still possible to measure the mass distribution, if a faraday cup is positioned at the off-axis port [Port 3.C3 or Port 3.C4].
3. For a similar flux to 2 it is also possible to measure the mass distribution of the clusters using the Wiley-McLaren TOF at the mass filter stage [Port 3.B]. However, then the von Issendorff & Palmer mass filter has to be removed.
4. To achieve extremely large deposited fluxes and very large beam spot sizes the cryostat cold finger can be moved to the mass filter stage [Port 3.B]. In this configuration, no monitoring of mass distribution is possible (but source conditions can be selected to provide clusters of prescribed mass within a narrow mass distribution). In the future, a new end flange on the mass-filter chamber and a new larger deposition chamber would enable the TOF to be mounted in the deposition chamber together with the cryostat cold finger thus allowing monitoring the mass distribution as well as depositing in the high flux, large beam spot regime.

In all configurations, the diameter and spacing of all apertures is variable in order to control the range of source flow rates, pressures and temperatures, which together control the deposition rate and the mass distribution of the clusters produced.

References

- Baker, S. H., Thornton, S. C., Keen, A. M., Preston, T. I., Norris, C., Edmonds, K. W., and Binns, C. (1997). The construction of a gas aggregation source for the preparation of mass-selected ultrasmall metal particles. *Rev. Sci. Instrum.*, 68(4):1853.
- de Heer, W. A. (1993). The physics of simple metal clusters: experimental aspects and simple models. *Rev. Mod. Phys.*, 65:611.
- Flüeli, M. (1989). *Observation des Structures Anormales de Petites Particules d'Or et d'Argent par Microscopie Electronique à Haute Résolution et Diffraction d'Electrons par un Jet d'Agrégats d'Argent*. PhD thesis, École Polytechnique Fédérale De Lausanne.
- Ganteför, G., Siekmann, H. R., Lutz, H. O., and Meiwes-Broer, K. H. (1990). Pure metal and metal-doped rare-gas clusters grown in a pulsed arc cluster ion source. *Chem. Phys. Lett.*, 165:293.
- Goldby, I. M., von Issendorff, B., Kuipers, L., and Palmer, R. E. (1997). Gas condensation source for production and deposition of size-selected metal clusters. *Rev. Sci. Instrum.*, 68(9):3327.
- Haberland, H. (1992). Apparatus and process for producing a thin layer on a substrate. United States Patent Application No. 5,110,435. filed May 5, 1992.
- Haberland, H., Insepov, Z., Karrais, M., Mall, M., Moseler, M., and Thurner, Y. (1993). Thin film growth by energetic cluster impact (eci): comparison between experiment and molecular dynamics simulations. *Materials Science and Engineering*, B19:31.
- Haberland, H., Karrais, M., Hall, M., and Thurner, Y. (1992). Thin-films from energetic cluster impact - a feasibility study. *J. Vac. Sci. Technol.*, A10:3266.
- Haberland, H., Mall, M., Moseler, M., Qiang, Y., Reiners, T., and Thurner, Y. (1994). Filling of micron-sized contact holes with copper by energetic cluster impact. *J. Vac. Sci. Tech.*, A12:2925.
- Hall, B. D. (1991). *An installation for the study of unsupported ultrafine particles by electron diffraction with application to silver: observation of multiply twinned particle structures*. PhD thesis, École Polytechnique Fédérale De Lausanne, Lausanne.
- Kaufmann, M. (2006). *Electron diffraction studies of unsupported antimony clusters*. PhD thesis, University of Canterbury, Christchurch.

Partridge, J. G., Scott, S., Dunbar, A. D. F., Schulze, M., Brown, S. A., Wurl, A., and Blaikie, R. J. (2003). Formation of electrically conducting mesoscale wires through self-assembly of atomic clusters. *IEEE Transaction on Nanotechnology*, 3(1):61.

Schmelzer Jr., J., Brown, S. A., Wurl, A., Hyslop, M., and Blaikie, R. J. (2002). Finite-size effects in the conductivity of cluster assembled nanostructures. *Phys. Rev. Lett.*, 88:226802.

Schulze, M., Gourley, S., Brown, S., Dunbar, A., Partridge, J., and Blaikie, R. J. (2003). Electrical measurements of nanoscale bismuth cluster films. *European Physical Journal D*, 24:291.

von Issendorff, B. and Palmer, R. E. (1999). A new high transmission infinite range mass selector for clusters and nanoparticles beams. *Review of Scientific Instruments*, 70(12):4497.

Wiley, W. C. and McLaren, I. H. (1955). Time-of-flight mass spectrometer with improved resolution. *Rev. Sci. Instrum.*, 26(12):1150.

Yokozeki, A. and Stein, G. D. (1978). A metal cluster generator for gas-phase electron diffraction and its application to bismuth, lead, and indium: Variation in microcrystal structure with size. *J. Appl. Phys.*, 49(4):2224.

Evolution and Utilisation of the UHV-Compatible Cluster Apparatus

Whereas Chapter 2 explained in detail the current design of the UHV-compatible cluster apparatus, this chapter gives an overview on the evolution and utilisation of the apparatus. Before going into the details, a short introduction to gas flow in vacuum is given in Section 3.1. Then a section describing the evolution of the system and the improvements done and suggested during the course of this PhD as well as general operational procedures follow (Section 3.2). In Sections 3.3 and 3.4 the inert gas aggregation cluster source and magnetron sputter source are explained respectively. The key parameters in the formation of clusters and in the formation of a molecular beam of clusters are given. Each of the cluster source sections are closed by an overview to the different cluster materials used with that source and source conditions. Once formed into a beam, the clusters can pass through a mass-selection filter prior to the deposition onto electrical contacted samples. An overview to different experiments using the mass-selection is given in Section 3.5.

3.1 Gas Flow in Vacuum

Before details on pump selection, pump speed and formation of a molecular beam of clusters are explained, this section provides the reader with the necessary background theory. The following is nevertheless only a brief summary of gas flow at reduced pressures. For further reading see [Moore et al., 1998; O’Hanlon, 1989].

The flow of residual gas in vacuum is determined by the quantity of gas flowing, the type of gas, the temperature and the pressure. It can be roughly divided into two regions. In the high pressure region the gas flow is viscous and for low pressures molecular. The two regions can be more precisely characterised by the ratio of the mean free path λ of the gas molecules compared to the size (a linear

dimension) d of the system that holds them. This is called the Knudsen number

$$K = \frac{\lambda}{d} \quad (3.1)$$

which is dimensionless. The mean free path λ is a function of pressure P and temperature T

$$\lambda = \frac{RT}{\sqrt{2}\pi N_A d^2 P} \quad (3.2)$$

with the gas constant R and Avogadro's number N_A .

Having a Knudsen number $K < 0.01$, the flow is called continuum flow. Characterisation of the gas is then by its viscosity and the gas is called viscous. The gas flow can be turbulent or laminar. Dominated by inter-molecule collisions, the gas flow through a pipe depends on the pressure of the gas. The velocity of the gas is zero at the walls of the pipe and reaches a maximum velocity at the center of the pipe. Going to much lower pressures the mean free path of the gas molecules becomes comparable and larger than the container that holds the gas, $K > 1$. This is called molecular flow region and the gas flow is a statistical process. Viscosity is no longer defined and gas-wall collisions are predominant.

In any case, the volume V of gas passing a plane in time t at constant pressure P is the throughput Q

$$Q = \frac{d}{dt}(PV) = PS, \quad (3.3)$$

where S is the volume rate at which gas is transported across a plane and is called pump speed.

The transmission of gas through a tube can be characterized by the conductance C of the tube and is defined as:

$$C = \frac{Q}{P_2 - P_1} \quad (P_2 > P_1). \quad (3.4)$$

The conductance of a network of tubes can be expressed analog that of an electrical circuit:

$$C_{parallel} = C_1 + C_2 + C_3 + \dots, \quad (3.5)$$

$$\frac{1}{C_{series}} = \frac{1}{C_1} + \frac{1}{C_2} + \frac{1}{C_3} + \dots. \quad (3.6)$$

Equation 3.3 gives the basic definition of pump speed S of a vacuum pump. However, pumps are connected to a vacuum system via a connecting pipe. The conductance C of this pipe reduces the effective pump speed S_{eff} on the system according to

$$\frac{1}{S_{eff}} = \frac{1}{S} + \frac{1}{C}. \quad (3.7)$$

	1 mm nozzle	2 mm nozzle	3 mm nozzle	Typical run
Source	850	210	92	24
2nd stage	3.7×10^{-1}	3.7×10^{-1}	3.7×10^{-1}	5.1×10^{-3}
3rd stage	1.4×10^{-4}	5.7×10^{-4}	1.3×10^{-3}	1.4×10^{-4}
4th stage	6.5×10^{-8}	1.1×10^{-6}	5.4×10^{-6}	6.2×10^{-6}

Table 3.1: Calculated Pressures at various stages within the UHV apparatus for a gas flow of 100 sccm Ar assuming molecular flow and same sized (zero length) apertures in all the stages. In a typical run a nozzle size of 1.5 mm was used. All Pressures are in Torr.

In general, the conductance is a function of size and shape of the tube, type of gas, temperature as well as the flow regime. For a long round tube of length L , diameter D and air at 20 °C, the conductance in the continuum flow regime is

$$C(\text{liter sec}^{-1}) = 1.38 \times 10^6 \frac{D^4}{L} \frac{P_1 + P_2}{2}. \quad (3.8)$$

This solution holds in the absence of turbulence (laminar flow), fully developed flow (no position dependency), zero wall velocity and for incompressible gas only. For molecular flow, the conductance is independent of pressure and the conductance for air at 20 °C is given as

$$C(\text{liter sec}^{-1}) = 0.12 \frac{D^3}{L}. \quad (3.9)$$

For a zero length tube, i.e. an aperture with an opening area of A , the conductance in the molecular flow regime for a gas of molecular weight M is given as

$$C(\text{liter sec}^{-1}) = 0.03 \left(\frac{T}{M} \right)^{1/2} A, \quad (3.10)$$

which for air at 20 °C is simply

$$C(\text{liter sec}^{-1}) = 0.1 A. \quad (3.11)$$

Using the equations of molecular flow in vacuum the pressures in the different stages of the UHV apparatus can be calculated. Table 3.1 lists the calculated different stage pressures for different size apertures. Compared to the actual run conditions (last column) the calculated source pressures are much higher. This is due to the fact that the molecular flow regime is not applicable for those high pressures. However, the calculated pressures for the deposition chamber are comparable to the actual pressures. The calculated pressures for the second stage are independent of the size of the apertures. This is due to the fact that the second stage pump is a Roots pump with a very high pumping speed.

3.2 The UHV-compatible Apparatus

3.2.1 Evolution of the Apparatus

Previously, in our group a high-vacuum (HV) cluster system was used (see Section 1.4 for a brief overview and [Hyslop, 2002; Wurl, 2003; Kaufmann, 2006] for a detailed description). The UHV-compatible cluster apparatus was designed to overcome difficulties encountered while using the HV system. For instance only one sample at a time could be characterised and a narrow and highly inhomogeneous cluster beam meant that the alignment of the sample within the cluster beam proved to be difficult. Furthermore, oxidation of the cluster assembled devices was not uncommon [Schulze et al., 2003]. Compared to the HV system, the new apparatus provides more flexibility for the in-situ characterization of electrically contacted samples. Two cluster sources can be used (Sections 3.3 and 3.4 respectively). The provision of a mass-filter allows mass-selecting clusters prior to the deposition (Section 3.5).

In the first phases of operation of the UHV-compatible cluster apparatus a diffusion pump was used as the second stage pump. This was soon replaced by a roots pump. Although the diffusion pump was capable of handling a throughput of up to 300 l/s of gas, during operation the pressure above the diffusion pump inlet was high enough to cause it to choke. This limits the throughput dramatically. Roots pumps however are capable of operating at higher pressures with very high throughputs.

Another improvement to the UHV-compatible cluster apparatus, compared to the previously used HV system, is the addition of a designated deposition stage. As mentioned previously, the main chamber of the HV system remained at higher pressures even after the depositions. This was mainly because the high inert gas flow had to be maintained until the source was cooled down enough.

A separate deposition chamber allows for separation from the main system once the deposition is done and ultimately reduces the oxidation risks after deposition. The deposition stage can be separated from the main system via a gate valve, which makes it possible to change samples and/or cluster sources without having to shut down all parts of the apparatus. For instance, it allows for a higher sample output for similar cluster source conditions. And in addition, samples can be deposited subsequently with different clusters without having to expose them to air first.

For the sample holder a new design had to be commissioned. Previously, in the HV system the samples stage was made from plastic (see Section 1.4). To ensure true UHV conditions care had to be taken what material is used. Plastic, even though not critical if only high vacuum conditions are desired, is a major source of outgassing in an ultrahigh vacuum environment. This led to the design of the

sample holder as it is presented in Section 2.5.1. Similar material choices were made when designing the von Issendorff & Palmer mass filter (see Section 2.4.1).

Further small improvements were suggested while operating the UHV-compatible cluster apparatus and were implemented in the system built by NCD [NCD Ltd. , 2004]. For instance having a pump connected to a vacuum system with an inlet mouth bigger than the port on the system reduces the effective pump speed of this pump. In our UHV system the third stage turbo pump outlet is an 8" port whereas the port it connects to is only 6" with a length of about 10 cm. Even though this is a turbo pump with a pumping speed of 520 l/s (for nitrogen) at the pump inlet, because of the restriction the effective pump speed of this pump is reduced to about 360 l/s (Equation 3.7). Connected to an 8" port of the same length this effect can be reduced and a net pumping speed of 460 l/s can be achieved.

The third stage of the UHV compatible cluster apparatus also hosts the von Issendorff & Palmer mass filter [von Issendorff and Palmer, 1999]. During the operation of the mass filter, it was found that additional small 2.75" ports for electrical feedthroughs would be of advantage to connect for instance a Faraday cup or an ionizer.

The second and third nozzle can be changed or their separation adjusted without removing the whole source stage on port 2.B. Hereby, one of the second stage 6" ports [Port 2.C1, 2.C2 and 2.C3] can be opened and allows access to the nozzles. However, those ports only have an inner diameter of 100 mm making it difficult accessing the apertures. Increasing this port size to an 8" port would be preferable.

Since the just mentioned improvements are structural they can not easily incorporated into the existing system. A second generation of cluster apparatus was built by Nano Cluster Devices Limited [NCD Ltd. , 2004] where those suggestions were included in the design.

The UHV compatible cluster apparatus built and commissioned during this thesis is now an important part of our research group. Currently, three PhD students and two Post Docs are involved in active research using this cluster apparatus. For instance, the system is used to further conduct studies on bismuth clusters in V-grooves [Ayesh, 2008]. In addition to bismuth clusters and antimony cluster, copper clusters were successfully prepared and deposited onto samples. Recently, the development and design of a new IGA source started, which will be used to form semiconducting germanium clusters.

3.2.2 Pump selection

As explained previously, a designated deposition chamber is of advantage to protect the nearly formed cluster assembled devices from oxidation due to exposure to high pressure. The first choice of such a deposition chamber was a separate

system which however was occupied for the studies of diffusion of dimers of bismuth and tetramers of antimony on pyrolytic graphite [Scott, 2005]. Following the success and subsequent continuation for the diffusion study, a new deposition chamber had to be commissioned for the UHV apparatus.

Apart from selecting a versatile chamber with enough ports for future expansion a new pump had to be selected for the new deposition chamber. It had already been decided to replace the second stage diffusion pump with a more efficient roots pump. Further improvements in the pump down speed and overall base pressure were desired. The following gives an overview of the selection of the third stage turbo pump and the deposition stage turbo pump.

During a cluster deposition experiment, a certain amount of inert gas is let into the source stage. Ideally, this is the only source of gas into the system. In addition, the pump speeds of the corresponding stage pumps and the bore of the separating nozzles are known. Then, using Equations 3.3, 3.4 and 3.10 (for zero length nozzles) the corresponding ultimate base pressures in each stage can be determined (see Table 3.1). This of course neglects the first initial pump down and eventual outgassing from the chamber walls. However, with this simple model it was possible to determine that it is favourable to have larger pump speed pumps earlier within the differential pumping stages in the vacuum system. From there, the decision was made to attach the newly bought larger pump speed Pfeiffer turbo pump (TMU521) at the third stage of the system. Whereas the deposition chamber is pumped with the smaller Pfeiffer turbo pump (TPH270), which was previously used at the third stage. Details on the current pumping equipment can be found in Chapter 2.

3.2.3 Baking

Clusters form at a wide range of pressures and source conditions. The UHV-compatible cluster apparatus however was built with the purpose of the formation of electrical contacted cluster assembled films/wires/devices. From previous experiments (see Section 1.4) using the HV chamber it was found that oxidation of the cluster-assembled devices is fatal. One source of oxygen within a vacuum chamber is water. This can be seen in a RGA scan (solid line in Figure 3.1). The strongest peak here (except the helium peak) is water. The dashed line shows the system having a (minor) leak and will be discussed later.

When pumping down a vacuum system the major gaseous constituents within the chamber change. While it is a mixture of nitrogen and oxygen at first, after a short while water vapour is the most dominant, because of outgassing of water from the chamber walls. Several layers of liquid water are at the walls of the vacuum chamber and slowly evaporate into the chamber, preventing UHV conditions being reached quickly.

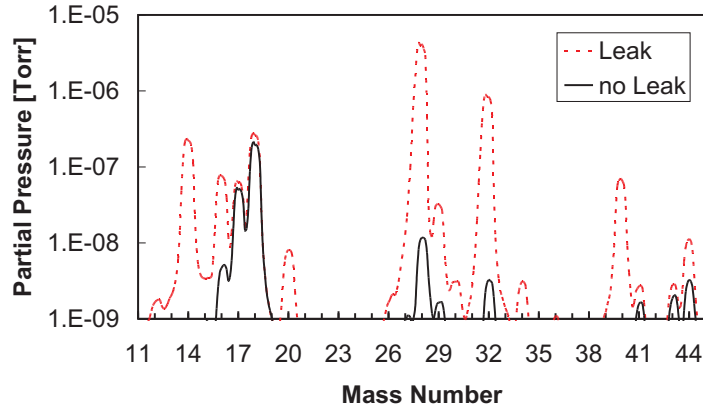


Figure 3.1: RGA scan showing a typical vacuum atmosphere after pumpdown (solid line). The peak at mass number 18 is the highest of the scan, indicating that water is one of the main constituent within the system. This is typically for unbaked vacuum systems. The dashed line shows a RGA scan for the vacuum system having a (minor) leak. It can be seen clearly that the peaks for oxygen at 32 and nitrogen at 28 have increased dramatically and dominate even the water peak.

The lower the pressure within a vacuum system the slower a new layer of water is able to form on a surface (e.g. the device of interest) inside the vacuum. For instance the time t_{ML} it takes to form a monolayer of water is about 25 seconds at a pressure of 10^{-6} Torr [Moore et al., 1998; O’Hanlon, 1989]. At a pressure of 10^{-9} Torr, the time t_{ML} is 25,000 seconds.

$$t_{ML} = \frac{4k_B T}{P \nu d_0^2}. \quad (3.12)$$

Here, P denotes the pressure inside the vacuum chamber, d_0 is the average size of the molecule and ν is the average velocity of the molecule. Equation 3.12 only applies for unity sticking and for uniform monolayer formation.

In order to achieve lower base pressures within the system it is therefore of advantage to be able to heat the chamber walls. This helps remove the water. Heater tape around the deposition chamber of the UHV compatible cluster apparatus allows baking the chamber prior to a deposition. This evaporates off the water, which then can be pumped away and therefore reduce the base pressure. Additionally, heater tape was installed around the second and third stage as well. This leads to an even lower ultimate base pressure, which is about one order of magnitude lower than without baking. Less water within the chamber means a cleaner environment for the formation of cluster-assembled devices.

3.2.4 Leak Testing

Water within a vacuum system is a source of oxygen. However it is a declining source and can be counteracted by baking the chamber walls of the vacuum system. Potentially far worse would be a replenishing source like a leak from the outside into the system which would bleed in oxygen. It is therefore necessary to regularly check a vacuum system for leaks.

For the system presented here, this is done using a helium gun and a residual gas analyzer (RGA). The RGA is a mass filter and can be set to only look for the mass of helium. Even very small amounts of helium can be easily detected. Helium is a trace gas in the atmosphere (only 5.3 ppm) and due its light weight travels very fast. Both makes it very useful as a leak test gas.

A vacuum system, once pumped down, would have almost no helium present within. If helium is sprayed around a possible leak site, it can enter the chamber through the leak and a sudden increase in the vapour pressure of helium can be registered at the RGA.

Nevertheless, this method is very time consuming since every possible leak site has to be tested. A possible leak site is for example any flange which has been opened since the last leak test. Since every port and flange has to be tested there is the risk that a possible leak is not found just because it has not been sprayed with helium. Therefore, leak testing has to be done regularly. A logbook of typical source conditions and chamber pressures helps to recognize a possible introduction of a new leak.

Figure 3.1 for example shows the comparison of two RGA scans. The solid line is a RGA scan of a ‘normal’ vacuum atmosphere while depositing clusters. The dashed line shows a RGA scan with the introduction of a small air leak to the UHV compatible vacuum system. Firstly, a leak increases the overall pressure within the vacuum system. This is indicated by the dashed line in Figure 3.1 to be above the solid line. Also, it can be seen for the dashed line that the dominant peak is no longer water (mass peak at 18) but the oxygen (peak at 32) and nitrogen (peak at 28) peaks. This could indicate that a leak is present. Large peaks at mass numbers 32 and 28 could also be argon and carbon dioxide respectively. However, an air leak is truly indicated by the 5:1 ratio of nitrogen to oxygen.

3.3 Inert Gas Aggregation Source

3.3.1 Introduction

One of the most commonly used cluster sources is the inert gas aggregation source (IGA), relying on thermal evaporation and aggregation of metallic vapour in the presence of an inert gas. The flow of inert gas such as argon or helium (or both)

cools the vapour creating a supersaturated region above the crucible. In this region, cluster formation takes place by homogeneous nucleation. The flowing gas carries the clusters out of the source chamber.

Inert gas aggregation sources provide a fast and reliable way of producing high flux cluster beams of (generally) low melting point materials. Following the prototype of this source [Sattler et al., 1980], several versions of this source were developed and a number of cluster deposition systems were discussed in the literature. Goldby et al. [Goldby et al., 1997] using an IGA, have deposited size-selected Pb and Ag clusters. Baker et al. [Baker et al., 1997] adapted their source to produce transition metal clusters.

3.3.2 Cluster Formation

Nucleation of clusters in an inert gas aggregation source occurs in the absence of nucleation seeds, which is known as homogenous nucleation. The following is a brief outline to the theory of cluster nucleation. A detailed description can be found elsewhere [Milani and Iannotta, 1999].

The difference in Gibbs free energy between a liquid droplet with radius r , density ρ and temperature T and the surrounding vapour is given by:

$$\Delta G(r) = 4\pi r^2 \gamma - \frac{4}{3}\pi r^3 \rho RT \ln(S), \quad (3.13)$$

where γ is the surface tension, R the molar gas constant and S the supersaturation ratio (this is the ratio between actual vapour pressure to saturated vapour pressure at temperature T). For a droplet, it is energetically favourable to grow only when the process decreases the free energy. This is the case only for supersaturated vapours ($S > 1$) and for droplets bigger than a critical radius r^* . Once a droplet is larger than r^* , it should grow without limit whereas droplet smaller than the critical value should shrink and evaporate.

In unsaturated vapour, there is always a distribution of droplets, which are formed randomly following a Boltzmann relation. In a supersaturated vapour, the population of droplets larger than the critical radius will grow.

Increasing the supersaturation will decrease the critical radius and improve the probability of randomly formed droplets larger than the critical radius. It therefore increases the cluster beam intensity.

3.3.3 Formation of a Molecular Cluster Beam

Once the clusters are formed within the source chamber they have to be transferred onto the contacted samples within the deposition stage further down the UHV compatible cluster apparatus. The following section outlines how the molecular cluster beam forms as shown using the IGA source as an example.

The pressures in the different stages are a function of the pumping speed, the amount and type of gas and the diameter of the apertures correspondingly (see Section 3.1 and discussion of pump selection in Section 3.2.2). For high source chamber pressures and low outer source stage pressures, the conductance C for an aperture at viscous flow is proportional to the area A of the aperture. Thus, for a bigger diameter first aperture the conductance through the aperture is higher. Reducing the first nozzle diameter (nozzle [a] in Figure 2.2), results in a higher source pressure, which is necessary for the formation of larger clusters. Increasing the length of this aperture, to a barrel or cylinder shape, gives a more collimated beam of clusters. Conversely, a short aperture in this location tends to cause large beam divergence.

The spread of the beam not only depends on the aperture, but also on the mass of the particles within the beam; the inert gas atoms and lighter clusters tend to diverge at the exit of the aperture more than heavier clusters due to thermal motion. However, having a more-collimated beam makes it more difficult to remove the inert gas from the beam, which mainly takes place at the second nozzle (nozzle [b] in Figure 2.2). This task becomes increasingly difficult as the beam divergence decreases i.e. for highly collimated beams. In order to compensate, the distance between the first and the second aperture can be increased. The shape of the second nozzle is skimmer-like. That means that the clusters (and the gas) at the centre of the beam pass through without being effected. Whereas the gas (and small clusters) at the outskirts of the beam are deflected backwards. Due to the lesser weight of the inert gas and higher thermic velocities, more gas atoms than clusters will be at the outskirts of the beam. Of course, reducing the diameter of this nozzle improves the extraction of the inert gas, but can also cut down the amount of clusters in the beam. At the third aperture (nozzle [c] in Figure 2.2), further collimation of the beam and extraction of inert gas occurs. The distance between the second and third apertures is readily adjustable using the threaded mount for the third aperture.

In Figure 3.2, source pressure versus the gas flow of argon is shown. Not surprisingly, the source pressure rises for increased argon flow. The source pressure mainly (but not exclusively) depends on the first nozzle in the system as it controls the pumping on the source chamber. Using Equation 3.8 and substituting C with Q using Equation 3.4 and assuming the pressure P_2 in the source is much higher than the pressure P_1 after the nozzle the relationship of P_2 versus Q (or gas flow) is found to be $P_2^2 \propto Q$. With Equation 3.3 this leads to a linear proportionality of the source pressure and the gas input, which is shown in Figure 3.2.

For high source pressures and low first stage pressures, the conductance C for an aperture at viscous flow is proportional to the area A of the nozzle (see Section 3.1). Thus, for a bigger diameter first nozzle the conductance through the nozzle is higher, which means that the source pressure is lower for the same

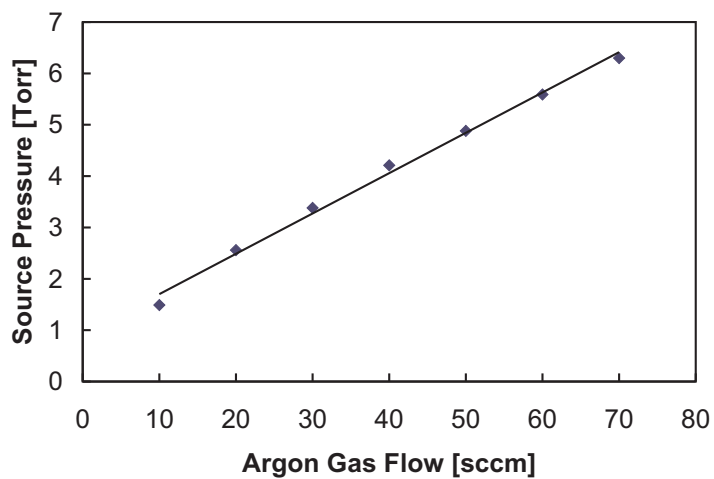


Figure 3.2: IGA source pressure versus gas flow of argon. Here the first nozzle was 9 mm long and had a diameter of 1.5 mm.

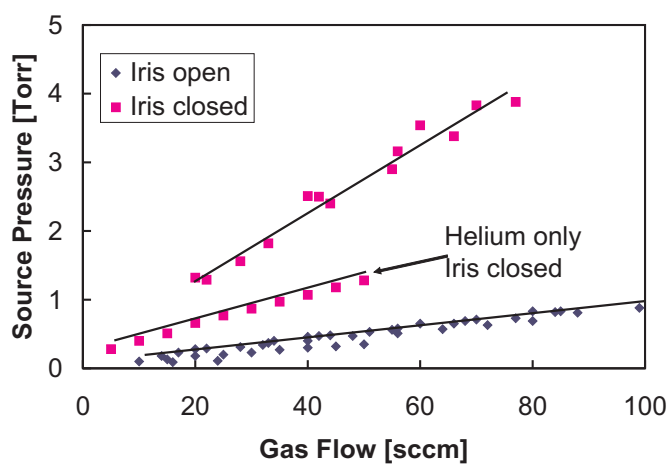


Figure 3.3: IGA source pressure versus gas flow for varying first aperture size.

amount of gas. This can be seen in Figure 3.3. Here an iris was used instead of a first nozzle. Open corresponds to an opening of about 8 mm and closed refers to an opening of about 1 mm. Clearly, it can be seen that the source pressure is lower for a larger diameter iris.

In addition, the conductance through an aperture depends not only on the area of the opening, it also depends on the mass of the gas flowing through (Equation 3.10), which can be seen in the case of the closed iris in Figure 3.3 for helium only gas flow. For the same amount of gas but different type of gas the pressure is lower the lower the molecular weight is of the gas passing through the aperture.

Taking into consideration the notes made in this section about the formation of a molecular beam of clusters it is possible using different size apertures and separation length between apertures to customize the beam spread of the cluster beam. Large beam spreads are favourable for cluster assembled devices since a more uniform deposition can be guaranteed. However, having a too large beam spread can reduce the deposition rate dramatically, since now the same amount of cluster material is spread wider. For experiments using the mass-filter or the time of flight spectrometer (see Section 3.5) a collimated beam of clusters is preferred.

3.3.4 Bismuth Clusters using the IGA

The low melting point of 271.3 °C [Stöcker, 1994] of bismuth and more importantly the high vapour pressure of bismuth at low temperatures [VEECO, 2006] make it an ideal candidate for cluster production using an inert gas aggregation source. This combined with the interesting properties bismuth exhibits as bulk and at the nanoscale (see Section 1.1.2) makes it an interesting material for the investigation of FCFs (Section 1.6) in cluster assembled nanoscale devices.

For a typical bismuth cluster deposition using the IGA presented here (Section 2.2), 99.999% bismuth pellets are placed into the crucible (see Figure 2.4). The source and the source backplate are mounted onto the system and the pumps are started. (Note that the IGA source stage includes an outer pumping stage which does not need to be removed for cleaning and replenishing the inner source.)

Once the pressure within the source stage is at around 1 Torr, the crucible is heated to 200 °C and a very small amount of argon (usually only about 10 sccm) is let into the system through the source. This is to evaporate off any water from the metal and pump down to base pressure.

Initially, the nozzles shown in Figure 2.2 were used. However later, it was found that having a much longer first nozzle a much more uniform bismuth cluster beam can be formed (see comments on the formation of a molecular cluster beam in Section 3.3.3). Figure 2.2 shows the nozzles typically used. However, for bismuth depositions a 40 mm long nozzle with a 1.2 mm diameter hole was used.

Material	Temperature °C	Pressure Torr	Gas(es) sccm	Sizes nm
Antimony	650	6.4	Ar 60 He 0	30
Antimony	650	16.3	Ar 60 He 300	10
Bismuth	800	4.67	Ar 100	35
Bismuth	800	23.5	Ar 100	35

Table 3.2: Typical source conditions using the IGA source.

Electrically contacted or un-contacted samples are mounted onto the cryostat cold finger and placed within the deposition stage (Section 2.5), which then is pumped down to base pressure. After the base pressure is achieved, the crucible is further heated to melt the bismuth and to create a vapour of bismuth above the crucible. As mentioned previously (Section 3.3.2) clusters form within supersaturated vapour. In the case of bismuth and using the inert gas aggregation source presented (Section 2.2) this happens at a crucible temperature of about 800 °C and an argon flow of about 100 sccm. Choosing a different flow rate (higher or lower) also produces clusters. However, the crucible temperature needs to be adjusted to obtain a reasonable deposition rate. In addition, bismuth clusters can also be produced using an argon helium mixture or helium only as the inert gas. The cluster size (obtained by FE-SEM images) did not change significantly for the different source parameters used.

The inert gas is used as a carrier gas to form a molecular beam of clusters and the bismuth clusters are deposited onto electrically contacted or un-contacted samples at a deposition rate of typically 0.6 Å/s. For contacted samples the deposition was stopped once an onset of conduction could be observed by closing the gate valve between the third and fourth stage. In the case of un-contacted samples, the deposition was stopped when the desired film thickness was achieved. Typical source conditions for bismuth and resulting cluster sizes are listed in Table 3.2.

3.3.5 Antimony Clusters

Even though bismuth is the material of choice for the study of FCFs (Section 1.6), antimony was used as well to fabricate cluster assembled nanoscale devices. Antimony is a brittle metal and belongs to the same group of elements as bismuth. This means it has similar properties to bismuth. For instance, antimony is a semimetal as well. Antimony cluster devices provide a good comparison to bismuth cluster assembled devices.

Antimony clusters were produced similar to previously described bismuth clusters (Section 3.3.4). Pellets of antimony (99.999%) were placed in a crucible sim-

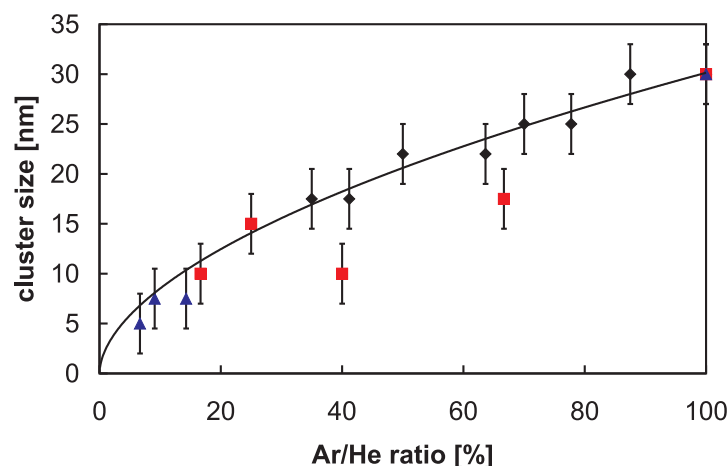


Figure 3.4: Size dependence of antimony clusters with helium/argon ratio. The line is a guide for the eye only. The symbols indicate different total amounts of argon. ▲ = 50 sccm Ar, ■ = 60 sccm Ar, ◆ = 70 sccm Ar.

ilar to Figure 2.4 and heated. Typical crucible temperatures were around 650 °C. It was found that antimony clusters can be produced having a crucible temperature lower than the melting temperature of antimony (melts at 630 °C). This is because antimony sublimates and can have a high enough vapour pressure even before reaching its melting point [VEECO, 2006]. The key factor for producing clusters using an IGA is a high vapour pressure at relatively low temperatures.

The nozzles used for antimony depositions are shown in Figure 2.2 (nozzles [a], [b] and [c]). Since having a much longer nozzle for [a] helped in the formation of bismuth clusters it was also tried for antimony cluster. However, this proved unsuccessful having a highly dispersed beam of antimony clusters.

The deposition for antimony cluster assembled nanoscale devices is similar to previously described bismuth cluster assembled nanoscale devices. Typical source conditions for antimony and resulting cluster sizes are listed in Table 3.2.

Antimony clusters can also be produced using an argon helium mixture or helium only as an inert gas. Interestingly and in contrast to bismuth clusters, increasing the helium to argon ratio changed the resultant cluster sizes. Figure 3.4 shows the variation of antimony clusters diameter versus argon to helium ratio. The clusters have diameters (obtained from FE-SEM images) ranging from 5 nm (He only) to 30 nm (Ar only). Using argon only, the cluster size did not change for Ar flow rates of 50 sccm, 60 sccm and 70 sccm.

It was found that antimony clusters with different sizes behave differently when being deposited. As can be seen in Figure 3.5, small antimony clusters strongly adhere to the plateaus between V-grooves on a SiO₂ coated silicon substrate, whereas large clusters bounce off. Further evidence for this surprising bouncing effect is that antimony clusters were found on the backside of an aperture,

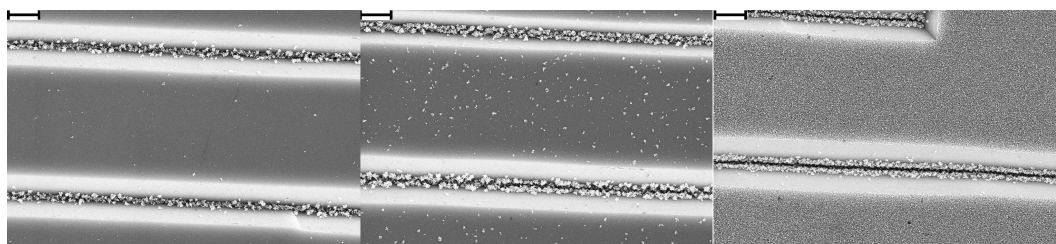


Figure 3.5: Antimony clusters produced using the IGA source at the apices of V-grooves and on plateaus between V-grooves for different cluster sizes (from left to right: 40 nm (Ar/He source flow-rates 60/0 sccm), 25 nm (Ar/He source flow-rates 60/30 sccm) and 15 nm (Ar/He source flow-rates 60/90 sccm)). The coverage of the plateaus between the V-grooves increases with decreasing cluster size. For 15 nm antimony clusters, the whole plateau is covered. Scale bar is 2 μm .

mounted 5 mm in front of the substrates. As can be clearly seen (in Figure 3.5), the plateau coverage increases with decreasing cluster size. Note, the addition of helium at a fixed argon flow rate should only slightly increase the cluster velocity; therefore this extra sticking effect is not due to a decreased velocity of the clusters. A more detailed investigation on the adhesion of clusters on various substrates can be found in Chapter 5.

3.4 Magnetron Sputter Source

3.4.1 Introduction

Another reliable way of producing clusters is the use of a magnetron sputter source. Haberland et al. [Haberland, 1992; Haberland et al., 1992; Haberland et al., 1993; Haberland et al., 1994] developed a source relying on magnetron sputtering and gas aggregation that allows the size of particles to be varied over a wide range. In this source, metal atoms are sputtered in an inert gas discharge using a high-pressure magnetron cathode. The gas atoms bombard the metal substrate sputtering away atoms. The sputtered atoms are decelerated by collisions with the inert gas in the liquid nitrogen (LN₂) cooled aggregation tube and aggregate to form clusters. Using a similar source, Goto et al. [Goto et al., 1997] have studied the dependence of alumina particles on the geometry and the temperature of the source exit. Hihara and Sumiyama [Hihara and Sumiyama, 1998] have investigated nickel clusters and their size-dependence on various different source parameters. Denby and Eastham [Denby and Eastham, 2001] have generated cluster fluxes of 5 nA using a magnetron source and a very simple mass-selection system.

Material	Power W	Pressure Torr	Gas(es) sccm	Sizes nm
Bismuth	12	0.47	Ar 100	< 10
Palladium	30	0.72	Ar 100	< 10
Silicon	30	0.41	Ar 200	32
Silicon	50	0.67	Ar 500	80 - 500

Table 3.3: Typical source conditions using the magnetron sputter source

3.4.2 Cluster Formation

The combination of magnetron sputtering and gas aggregation source can efficiently produce clusters. Nevertheless, only very few clusters are directly sputtered off the target. Mainly clusters are formed by homogeneous nucleation in the surrounding inert gas as described in Section 3.3.2. However, due to many charges present this process is strongly modified.

Significant fractions of the clusters are ionised due to efficient charge transfer processes in the sputter discharge. The mass distribution of the clusters produced in this source depends on the target material, the pressure in the aggregation tube, the sputter discharge power, the inert gas (gases) used and the aggregation length. Increasing the helium to argon ratio, for example, will lower the cluster size and increasing the aggregation length leads to a bigger mass distribution of clusters within the beam.

3.4.3 Cluster Experiments using the Magnetron Sputter Source

Unlike for the IGA source, where clusters of low melting point materials can be formed using the magnetron sputtering source clusters of high melting point materials (including semiconducting materials) can be produced. This allows for the formation of clusters of almost any material. However, a good contact between the target and the electrode is needed. So in the case of semiconducting targets a highly doped one is preferred with an Ohmic contact at the interface between the electrode and the target. The doping of the clusters is not necessarily the doping of the target, since the clusters form from atomic vapour and the vapour pressure is different for different materials.

Using the magnetron sputter source, bismuth clusters, palladium clusters and silicon clusters were investigated. Typical source conditions using the magnetron sputter source and resulting cluster sizes for the targets tested are listed in Table 3.3.

Bismuth

In addition to the bismuth clusters produced using the IGA source (Section 3.3.4), bismuth clusters were produced using the magnetron sputter source. A 2" diameter 99.999% bismuth target was placed on the sputter head and a sputter plasma ignited. However, having a low melting point material exposed to a high temperature plasma is difficult. Using too much power and the target melts. Using too little power and no plasma ignites. After the initial pump down and cooling of the source walls with liquid nitrogen, argon was bled into the source around the target and a plasma ignited. The stream of inert gas is also used to push the clusters out of the source and form a molecular beam of clusters (Section 3.3.3).

From Table 3.3 it can be seen that the bismuth clusters formed were smaller than the bismuth clusters produced using the IGA (Table 3.2). Even though the magnetron sputter source can produce small bismuth clusters which are partially ionised the inert gas aggregation source is still the source of choice due to the uncomplicated and reliable formation of bismuth clusters.

Palladium

Bismuth (as well as antimony) is a semimetal having a low electrical conductance. The properties (Section 1.1.2) of bismuth make it an interesting material to investigate FCFs. However, fabricating cluster assembled nanoscale devices with a low conductance material like bismuth or antimony it is problematic to measure the conductance. Palladium on the other hand is a high conductance material which can be used in comparison with bismuth or antimony cluster assembled devices. Palladium is a very desirable material for cluster production since bulk palladium is known to absorb hydrogen and by doing so 'swell'. Using this property in cluster assembled devices produces a highly sensitive hydrogen sensor [NCD Ltd. , 2004].

For this thesis a 2" diameter 99.95% palladium target was used. Palladium is an easy to sputter material and cluster sizes of less than 10 nm were produced. Table 3.3 shows the typical source conditions used to produce palladium clusters. Due to the uncomplicated production of palladium clusters using the magnetron sputter source and the fact that the sputter source produces ionised clusters, palladium clusters were used to further undertake studies using the von Issendorff & Palmer mass filter and the TOF (see Section 3.5).

Silicon

Bismuth as a semimetal has a conductance much lower than that of a typical metal like palladium, and more similar to a highly doped semiconductor. Forming semiconducting cluster assembled nanoscale device allows comparison of the conductance mechanism of bismuth cluster assembled nanoscale devices with well

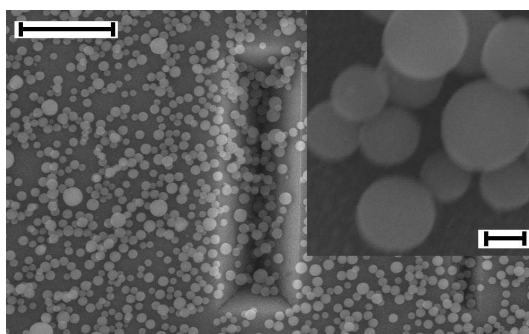


Figure 3.6: Silicon clusters produced with the magnetron sputter source (scale bar is $2\ \mu\text{m}$). Inset shows the silicon clusters magnified (scale bar is $100\ \text{nm}$).

known conductance properties of semiconductors. A highly doped p-type silicon 2" diameter 99.9999% target having a resistivity of $0.005\ \Omega\text{cm}$ to $0.020\ \Omega\text{cm}$ was used to produce semiconducting silicon clusters.

Having a semiconducting target however introduces problems. Even such highly doped silicon is still more resistive than for instance bismuth which has a resistivity of $107 \times 10^{-6}\ \Omega\text{cm}$ [Stöcker, 1994]. This can make it difficult to achieve the ignition of a plasma or a higher power has to be used. Another problem is that silicon is brittle and easily breaks. Sputtering produces very high temperatures which means the target material will expand. In addition, a tight fit is necessary to achieve good electrical contact with the sputter head.

Nevertheless, silicon clusters were produced and deposited onto uncontacted samples (see Table 3.3 for typical source conditions). However, the dispersion of the cluster beam was so wide that the samples had to be moved towards the exit of the sputter source right in front of the third aperture (nozzle [c] in Figure 2.2). Figure 3.6 shows silicon clusters deposited in front of the third aperture. As can be seen the clusters are very big (around $100\ \text{nm}$). In addition, the size varies with the biggest clusters having a diameter of $500\ \text{nm}$. In conclusion, silicon clusters were successfully produced using the magnetron sputter source. The molecular beam formed is highly disperse and a great cluster size variation was achieved. Contacted samples could not be produced using silicon clusters.

3.5 Mass Selection

3.5.1 Introduction

As mentioned in the previous sections clusters can be produced with sizes ranging from less than $3\ \text{nm}$ to up to $500\ \text{nm}$. Since many properties of clusters are size dependent over a very broad range of cluster sizes, it is of great interest to size-select clusters prior to deposition.

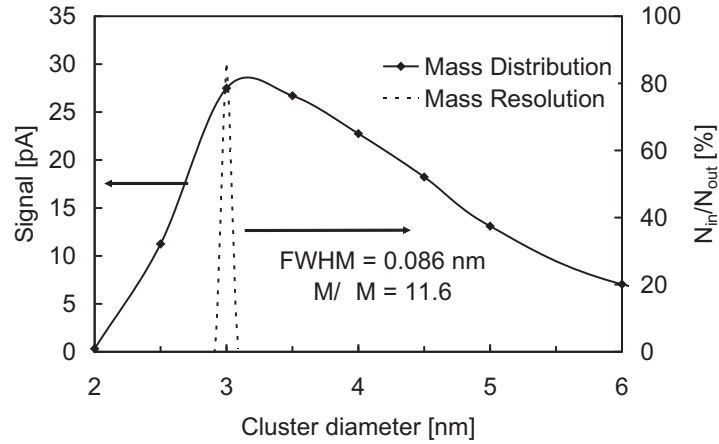


Figure 3.7: Mass distribution (diamonds) for palladium clusters using the magnetron sputter source for an acceleration voltage of 500 V. The line is a guide to the eye only. The dotted line shows the mass resolution obtained using SIMION simulation for ~ 3 nm Pd cluster. FWHM for the simulation is 0.086 nm, which corresponds to a mass resolution of 11.6. [Ayesh et al., 2006]

In order to fabricate devices on timescales of seconds or minutes, high-flux cluster beams are required. This means that there is a fundamental trade off between mass resolution and cluster flux. A high flux mass-selection system should therefore have a broad range with reasonable size-independent resolution and should be as efficient as possible, i.e. it should let most of the clusters with a given mass range through. Instead of selecting a particular size, it is favourable to size select a mass range.

3.5.2 Mass Filter

The mass filter used here [von Issendorff and Palmer, 1999] (see Section 2.4.1) combines relatively high resolution with high throughputs. We have achieved a cluster flux corresponding to a DC current of ~ 100 pA of mass selected Pd clusters. The mass resolution of this particular mass filter depends on the exit opening Δx and the spacing x (lateral displacement between the entrance and the exit) of the mass filter. In our case the theoretical value is $M/\Delta M = x/\Delta x \approx 12$. Since properties of the clusters under investigation here (> 3 nm) are usually only weakly size dependent, ultra-high mass-resolution is not required; in addition, since throughput is important in the present experiments, a system with a too high resolution is not desirable as almost all of the available flux would be eliminated in the mass filter stage.

Figure 3.7 shows the mass spectrum for palladium clusters obtained using the von Issendorff & Palmer mass filter (operated in configuration 1). Here the detector was a simple Faraday cup and electrometer combination and the mass distribution was obtained by varying the delay time and the pulse time, as dis-

cussed in Section 2.4.1. The mass distribution in Figure 3.7 was produced using an acceleration/deceleration voltage of 500 V. The clusters were produced using the magnetron sputter source with a sputter power of 30 W.

Extensive SIMION simulations have been performed [Ayesh et al., 2006] in order to understand and characterise the von Issendorff & Palmer mass filter. The mass resolution for 3 nm palladium clusters was determined from these simulations and is shown as the dashed line in Figure 3.7. For each cluster size (corresponding to a different pulse time and the delay time as given by the formulae in [von Issendorff and Palmer, 1999]), the simulation was performed using 700 clusters randomly distributed over the length of the mass filter and a 6 mm diameter beam width corresponding to the entrance and exit aperture diameters used in the experiments. This is a simple method of generating a continuous beam of clusters in the simulations. The calculated percentage of clusters which leave the mass filter is based on the number of clusters that exit the region between the acceleration plates (i.e. clusters that collide with the acceleration plates are not counted — note however that for correct choice of the pulse sequence the number of such clusters will be minimal).

The simulations show that the mass resolution $M/\Delta M$ is ~ 12 in good agreement with [von Issendorff and Palmer, 1999]. The FWHM for this simulation is 0.086 nm i.e. the resolution function for the system is far smaller than the width of the distribution of generated clusters and more than satisfactory in terms of production of cluster-assembled devices. Further results of experimental and simulation studies are discussed elsewhere [Ayesh et al., 2006].

3.5.3 Testing the TOF

Although the von Issendorff & Palmer mass filter is preferred to size select clusters prior to deposition, cluster size distributions can also be investigated using the TOF mass spectrometer [Kaufmann, 2006] as well. Palladium clusters produced using the magnetron sputtering source were used for this investigation.

Figure 3.8 shows the mass distribution of palladium clusters measured using the TOF (operated in configuration 3). For this particular spectrum, the TOF was run with only one acceleration region, with an acceleration voltage of 4 kV (see Section 2.4.2 for modes of operation). The clusters were produced using the magnetron sputter source with a sputter power of 25 W. It was found that the sputter power influences the cluster size: for higher power, larger clusters are produced. A more detailed description on the functionality of this particular TOF can be found elsewhere [Kaufmann, 2006].

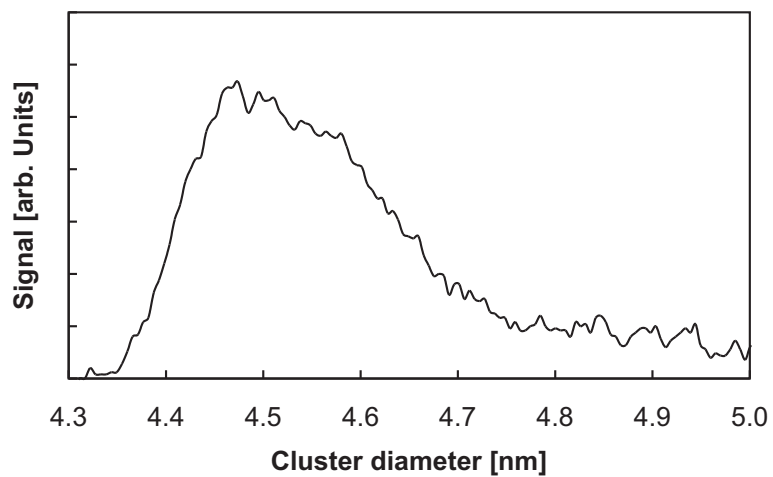


Figure 3.8: Time of Flight mass spectrum for palladium clusters produced with the magnetron sputter source. A single acceleration voltage of 4 kV was used to obtain this spectrum.

References

- Ayesh, A. (2008). PhD thesis, University of Canterbury, Christchurch. to be submitted.
- Ayesh, A., Lassesson, A., Brown, S., Dunbar, A., Kaufmann, M., Partridge, J., Reichel, R., and van Lith, J. (2006). Experimental and simulational study of the operation conditions for a high transmission mass filter. *Review of Scientific Instruments*. submitted.
- Baker, S. H., Thornton, S. C., Keen, A. M., Preston, T. I., Norris, C., Edmonds, K. W., and Binns, C. (1997). The construction of a gas aggregation source for the preparation of mass-selected ultrasmall metal particles. *Rev. Sci. Instrum.*, 68(4):1853.
- Denby, P. and Eastham, D. A. (2001). Efficient technique for producing high-brightness, size-selected cluster beams. *Appl. Phys. Lett.*, 79(15):2477.
- Goldby, I. M., von Issendorff, B., Kuipers, L., and Palmer, R. E. (1997). Gas condensation source for production and deposition of size-selected metal clusters. *Rev. Sci. Instrum.*, 68(9):3327.
- Goto, M., Murakami, J., Tei, Y., Yoshimura, K., Igarashi, K., and Tanemura, S. (1997). Formation of alumina fine particles by a magnetron sputtering gas aggregation method. *Z. Phys.*, D40:115.
- Haberland, H. (1992). Apparatus and process for producing a thin layer on a substrate. United States Patent Application No. 5,110,435. filed May 5, 1992.
- Haberland, H., Insepov, Z., Karrais, M., Mall, M., Moseler, M., and Thurner, Y. (1993). Thin film growth by energetic cluster impact (eci): comparison between experiment and molecular dynamics simulations. *Materials Science and Engineering*, B19:31.
- Haberland, H., Karrais, M., Hall, M., and Thurner, Y. (1992). Thin-films from energetic cluster impact - a feasibility study. *J. Vac. Sci. Technol.*, A10:3266.
- Haberland, H., Mall, M., Moseler, M., Qiang, Y., Reiners, T., and Thurner, Y. (1994). Filling of micron-sized contact holes with copper by energetic cluster impact. *J. Vac. Sci. Tech.*, A12:2925.
- Hihara, T. and Sumiyama, K. (1998). Formation and size control of a Ni cluster by plasma gas condensation. *J. Appl. Phys.*, 84(9):5270.
- Hyslop, M. (2002). *Electron diffraction studies of unsupported clusters*. PhD thesis, University of Canterbury, Christchurch.

- Kaufmann, M. (2006). *Electron diffraction studies of unsupported antimony clusters*. PhD thesis, University of Canterbury, Christchurch.
- Milani, P. and Iannotta, S. (1999). *Cluster Beam Synthesis of Nanostructured Materials*. Cluster Physics. Springer.
- Moore, J. H., Davis, C. C., and Coplan, M. A. (1998). *Building Scientific Apparatus*. Perseus Books, second edition edition.
- NCD Ltd. (2004). www.nanoclusterdevices.com.
- O'Hanlon, J. F. (1989). *A User's Guide to Vacuum Technology*. Wiley-Interscience.
- Sattler, K., Mühlbach, J., and Recknagel, E. (1980). Generation of metal clusters containing from 2 to 500 atoms. *Phys. Rev. Lett.*, 45:821.
- Schulze, M., Gourley, S., Brown, S., Dunbar, A., Partridge, J., and Blaikie, R. J. (2003). Electrical measurements of nanoscale bismuth cluster films. *European Physical Journal D*, 24:291.
- Scott, A. S. (2005). *Self-Assembly of Sb and Bi Nanostructures on Graphite*. PhD thesis, University of Canterbury, Christchurch.
- Stöcker, H. (1994). *Taschenbuch der Physik*. Verlag Harri Deutsch, 2nd edition.
- VEECO (2006). URL. www.veeco.com.
- von Issendorff, B. and Palmer, R. E. (1999). A new high transmission infinite range mass selector for clusters and nanoparticles beams. *Review of Scientific Instruments*, 70(12):4497.
- Wurl, A. (2003). *Electron diffraction studies of unsupported bismuth clusters*. PhD thesis, University of Canterbury.

Sample Preparation

In Section 1.7.2 a cluster sample design was presented for the investigation of FCFs in bismuth cluster assembled devices. This chapter describes the various steps in the preparation of such a sample. Section 4.1 shows the principal steps of making a cluster sample and presents the facilities used. In Section 4.2 the preparation techniques are explained in detail. The following section then (Section 4.3) describes different styles of samples used during the course of this thesis. They include PMMA-templated samples and percolating cluster-film samples.

4.1 Introduction

In order to electrically characterize nanoscale devices repeatable and controllable device test procedures have to be developed and adhered to. Accordingly, a standard device layout was developed. This layout integrates the cluster-assembled device structures into a lithographically defined electrical contact pattern which in turn, mates with a standard UHV compatible sample holder (see Section 2.5).

4.1.1 Sample Preparation Steps

Figure 4.1 shows schematically the preparation steps needed in order to form a cluster assembled device. For the samples a clean silicon wafer with 100 nm silicon oxide and 100 nm silicon nitride on top was used (Figure 4.1 a).

Then a hole was made into the oxide and nitride top layers to connect to the silicon wafer underneath. This hole called ‘via’ is chemically etched to be able to electrically contact the backside of the wafer and use the silicon substrate as a backgate for the cluster assembled device. Following the forming of the vias, the large scale contact pads (the device layout) were formed using optical lithography. This is step b) in Figure 4.1.

Figure 4.2 shows a typical device contact layout used. The large scale contacts consist of 10 contact pads. The middle pads in the top and bottom row of

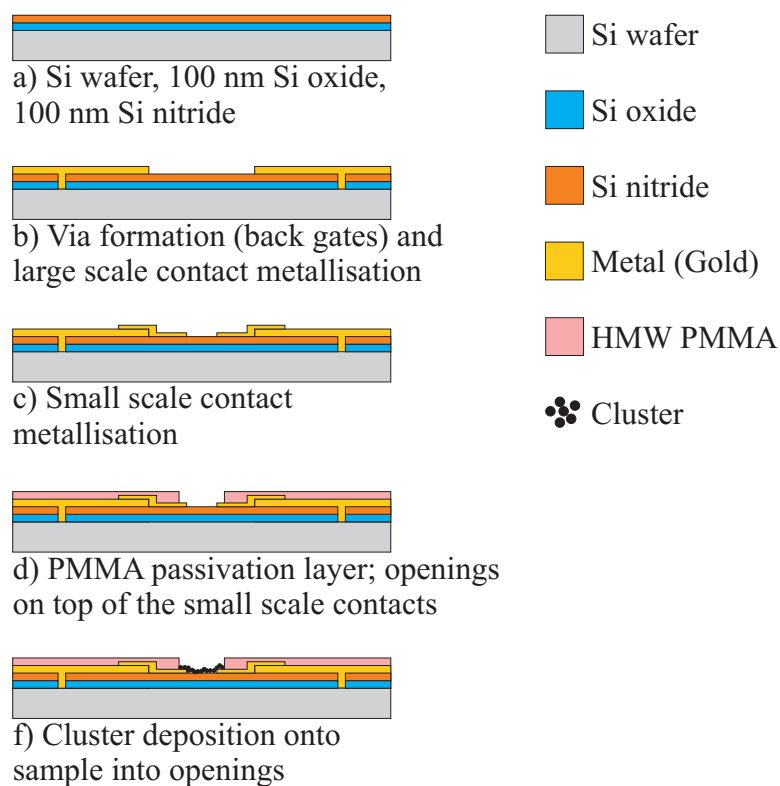


Figure 4.1: Schematic for the sample preparation of PMMA-templated slot samples and four point samples.

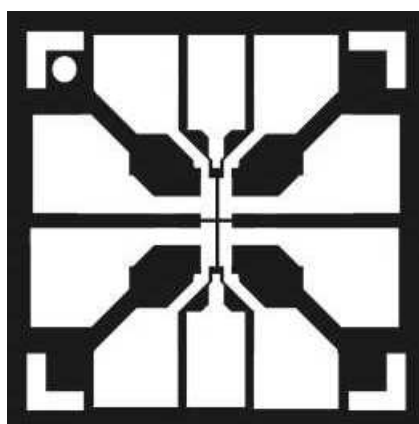


Figure 4.2: A typical large scale contact layout.

Figure 4.2 provide contact to the substrate. Each pair of corner contact pads are joined together. This is to ensure that the the pins of the UHV compatible sample holder (see Section 2.5) make good contact to the sample itself and to the nanoscale cluster device in particular. The small dot in the top left corner is to ensure a reference for identification of the individual cluster devices on the sample.

Optical lithography can easily achieve resolutions to a scale of $1\ \mu\text{m}$. As proposed (Section 1.7.2), the aim was to contact just a few bismuth clusters. Due to the smaller wavelength of electrons compared to UV light, smaller patterns can be achieved using electron beam lithography (EBL). For the formation of the small scale contacts (Figure 4.1 c) electron beam lithography was used.

Once the electrodes have been formed the sample needs to be passivated to avoid possible stray cluster connections across the sample. The cluster assembled devices (device of interest or DOI) are only to be formed between the small scale electrodes. For the passivation a PMMA film is formed on top of the samples having openings only above the small scale electrodes (Figure 4.1 d). The openings were formed using electron beam lithography. This concludes the sample preparation.

To form cluster assembled devices, the prepared samples were placed on a sample holder (Section 2.5) and positioned in the UHV-compatible cluster apparatus. Then bismuth clusters are deposited onto the samples (Figure 4.1 f). Once a cluster connection is made, testing of the cluster assembled device begins.

4.1.2 Facilities

Sample preparation was carried out using the fabrication facilities available in the Electrical and Computer Engineering Department and the Physics and Astronomy Department at the University of Canterbury. Apart from the following equipment, standard fabrication tools including spinners, hot plates and mask-aligners (Süss MA6 and MJB-3 models [Suss MicroTec, 2006]), which were used in the production of the contacted samples.

Reactive Ion Etcher

For the back-gate (via) etch (Figure 4.1 b), a Reactive Ion Etcher (RIE) (Oxford Plasmalab 80 Plus) [Oxford Plasma, 2006] was used. The RIE is a vacuum chamber which can be filled with various different gases or mixtures of gases at a controlled pressure and controlled temperature. Those gases include oxygen, argon, CHF_3 and others. Once the set pressure and temperature is achieved, a plasma is ignited which reacts with the surface atoms of the sample in such a way that they are removed (etched).

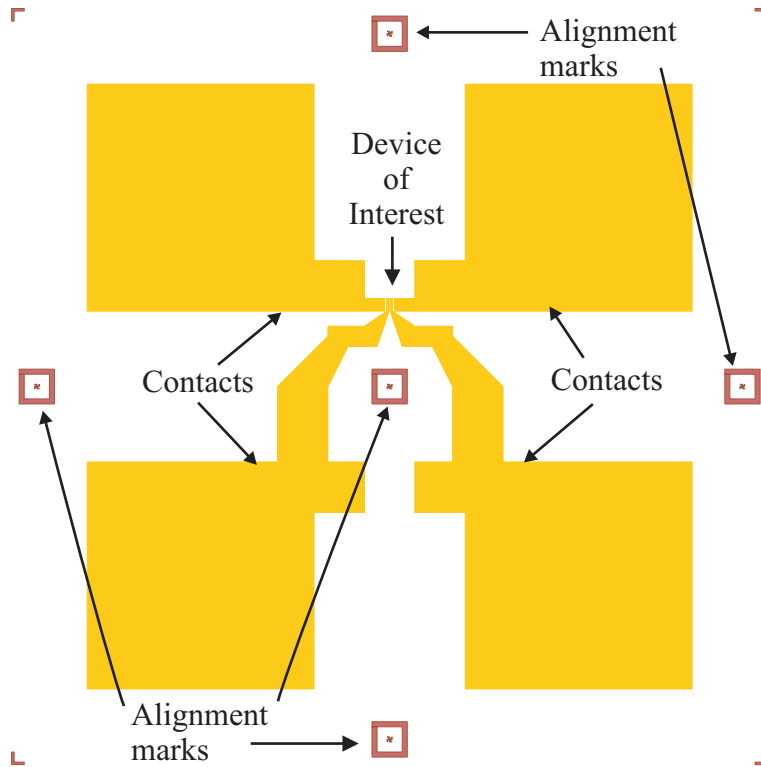


Figure 4.3: An EBL pattern. This pattern was used for the formation of the four point sample small scale contacts. Note the five alignment marks. This pattern is $0.3 \times 0.3 \text{ mm}^2$ in size.

Field Emission Scanning Electron Microscope – FE-SEM

For EBL, the desired patterns are written line by line into electron beam sensitive resist (PMMA) with an electron beam. The beam is controlled by the pattern generator which transfers a pattern file (Figure 4.3) onto the substrate and into the resist. For a fixed electron beam current, the dosage necessary to fully expose the resist can be adjusted by choosing an appropriate dwell time or area step size, which are interdependent according to Equation 4.1. The electron beam current is measured using a Faraday cup.

$$\text{Area Dose} = \frac{(\text{Beam Current} \times \text{Area Dwell Time})}{(\text{Area Step Size})^2}. \quad (4.1)$$

Figure 4.3 shows the EBL pattern used for the formation of the four point samples small scale contacts. The small scale contact pads shown overlap partially with the large scale pads shown in Figure 4.2. The five alignment marks shown in Figure 4.3 are used to align the next pattern (not shown) on top of the small scale contacts. The next pattern is to form an opening in the PMMA passivation layer over the area of interest.

In Figure 4.4, a pattern used for the small scale contacts for the slot samples can be seen. The large pads shown are not actually a part of the pattern but the centre of the large scale contact layout in Figure 4.2. Since EBL is a line

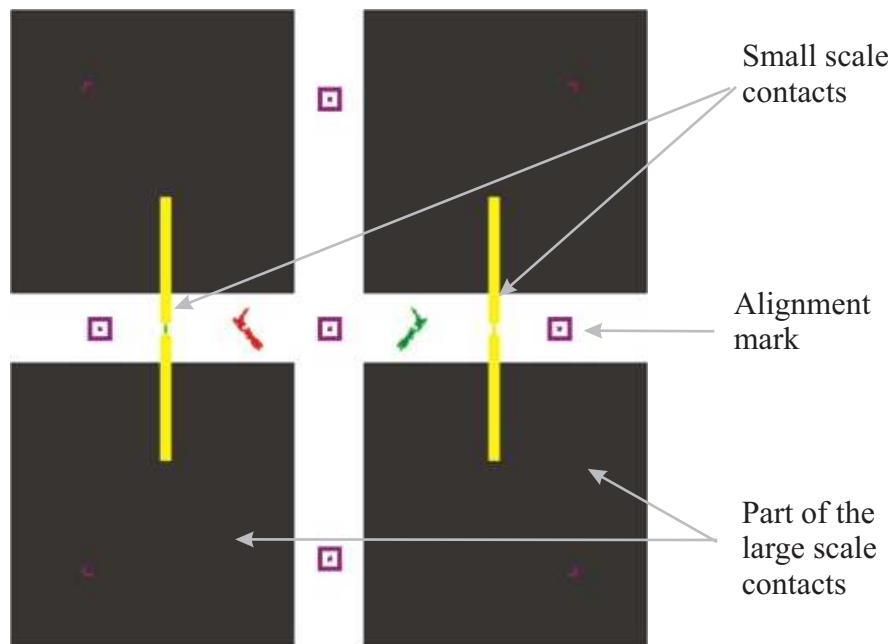


Figure 4.4: One of the patterns used to form the small scale contacts of the slot samples. Note the five alignment marks. This pattern is $0.3 \times 0.3 \text{ mm}^2$ in size.

by line writing process having a too large pattern results in a long writing time. Therefore, the small scale contact pattern only contained the contact fingers and the alignment marks. The five alignment marks shown in Figure 4.4 are used to align the opening in the passivation layer over the small scale contact fingers.

A LEO-32/Raith-150 Field Emission Scanning Electron Microscope and combined Electron Beam Lithography system [Goodberlet et al., 2001] was used for the electron beam lithography and pre- and post- deposition sample inspection necessary in this thesis. This FE-SEM is an electron microscope equipped with a fast pattern generator.

Atomic Force Microscope

An Atomic Force Microscope (AFM) (Dimension 3100) [VEECO, 2006] was used for post-deposition sample inspection. This instrument provided vital topographical information, e.g. cluster layer thickness, resist layer thickness, surface roughness and RIE etch-depth measurements.

Thermal Evaporator

For the various metal evaporations necessary for sample contacts, a Balzers BA510A thermal evaporator (Electrical Engineering Department) or an Edwards 306 thermal evaporator (Physics and Astronomy Department) were used [Balzers, 2006; BOC Edwards, 2006]. In a thermal evaporator metal is resistively heated

in a boat in vacuum to evaporate thin films of metal on a given substrate. The thickness of the film is monitored with a film thickness monitor (FTM).

Cleaning and Dicing of Substrates

The substrates used were either 4" or 3" commercially available silicon substrates [Silicon Quest International, 2006]. The 4" wafers are p-type <100> silicon with a resistivity of 0.01 - 0.02 Ωcm . They have a 100 nm thick thermally grown silicon oxide layer and a 100 nm thick silicon nitride top layer. The 3" wafers are n-type <110> silicon with a resistivity of 1 - 10 Ωcm and a thermally grown 100 nm thick silicon oxide top layer. Prior to all processing the wafers were cleaned using first acetone, then methanol and then isopropyl alcohol (IPA). Next, they were blow-dried with N_2 and baked at 95 °C for 30 min.

At the appropriate time, depending on what samples were made, the wafers were cut into $10.5 \times 10.5 \text{ mm}^2$ samples using a semiconductor dicing saw (Tempress Model 602). Before dicing, a thick photo resist layer was spun onto the layers. This layer prevents silicon fragments from adhering to the surface of the samples during the dicing process and is dissolved in acetone after the dicing is complete. The wafers could also be cut using a diamond-tip pen.

4.2 Preparation Techniques

4.2.1 Formation of Backgate Contacts

A UV-sensitive photo resist (AZ 1518 [AZ Electronic Materials, 2006]) was spun onto the clean substrates at 4000 rpm for 1 min. Afterwards the resist was soft-baked on a hotplate at 90 °C for 2 min. Then, using a mask-aligner, it was selectively exposed to UV light through a glass mask on which the desired pattern is represented in chrome. After the exposure the resist was developed in AZ 300 developer [AZ Electronic Materials, 2006].

In the backgate contact process step, areas of the insulating oxide (or nitride) layer have to be removed in order to reveal the underlying silicon substrate (Figure 4.1 b). This is usually done with either wet- or dry-etching. Wet-etching refers to an etch process with chemical solutions whereas dry-etching is performed in a vacuum apparatus using a reactive plasma. Dry-etching is the preferred method if anisotropic etching is required; it results in near-vertical etch profiles and is often more controllable than wet-etching. The wafers with the exposed and developed resist patterns were placed in the RIE system. Silicon oxide (or silicon nitride) was etched in our apparatus using plasma mix of CHF_3/Ar at -20 °C and 0.01 Torr. The etch rate was measured from test samples using AFM and found to be approximately 40 nm per minute.

During the etch process, the photo resist becomes hard baked. Therefore, following the etch process, the photo resist was removed using a piranha clean for 10 min. This is a mix of 1 part hydrogen peroxide to 5 parts sulfuric acid and this solution is effective in removing organic residues like photo resist. However, the piranha process leaves a thin oxide layer on the substrate which must be removed. The latter step was performed using a hydro fluoric acid dip (typically the samples were immersed in 10:1 H₂O:HF for 10 seconds).

4.2.2 Formation of Large Scale Contacts

The process of forming the large scale metal contacts again involved photolithography. The patterns for the large scale contact pads were exposed using a different mask (see Figure 4.2). To form the contact pads the wafers with the exposed and developed resist were mounted into the thermal evaporator. At a base pressure of 10^{-6} Torr first an adhesion layer of 5 nm Nichrome (80:20 nickel:chrome alloy) was thermally evaporated. This was followed by a layer of 50 nm gold.

Next, the resist and the metal on top of the resist were removed using acetone in a lift-off step. The metal remains only in the areas defined by the mask and the developed resist layer. The lift-off can be assisted prior to the evaporation, by adding an oxygen ashing process, in which an oxygen plasma etches the developed areas of the surface and removes any residues remaining after the development process in the resist.

Step b) in Figure 4.1 shows the result of the back-gate etch and the large scale metallisation. Between each resist-based step, the wafers were cleaned using first acetone, then methanol and at last isopropyl alcohol (IPA) followed by a blow dry with nitrogen.

4.2.3 Formation of Small Scale Contacts

The small scale contacts for the PMMA-templated samples were formed using electron beam lithography, which is similar to the previously described optical lithography. However, instead of using UV-sensitive photo resist, the resist now is sensitive to a beam of electrons. For the e-beam lithography, the Raith150 EBL System was used.

The e-beam sensitive resist used is made of a high molecular weight (HMW) polymer (poly-methyl methacrylate or PMMA) which breaks into smaller molecules when hit by the electrons. The smaller molecules of PMMA are easily dissolved with methyl isobutyl ketone (MIBK), leaving only the HMW PMMA. The molecular weight hereby refers to the weight of an individual PMMA molecule. In the case of HMW this is 996k (or 996,000 a.u.) [Sigma-Aldrich, 2006]. Apart from HMW PMMA low molecular weight PMMA (LMW PMMA) was also used hav-

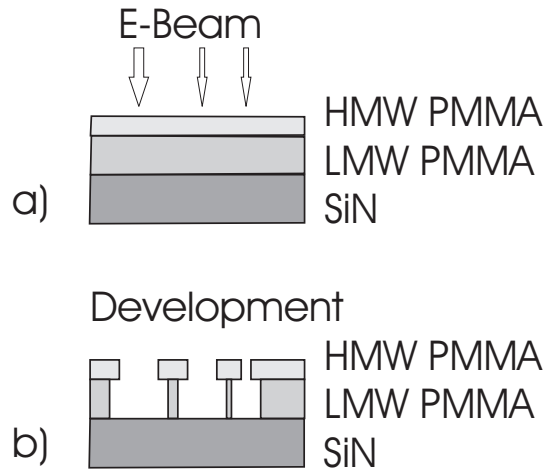


Figure 4.5: Bi-layer process

ing a molecular weight of 112,000 a.u. [Sigma-Aldrich, 2006]. The HMW PMMA was in solution in xylene (typically at 2.5% weight) and the LMW PMMA was in solution in chlorobenzene (typically at 4% weight). If not otherwise stated, HMW and LMW PMMA refer to those properties. Since LMW PMMA is more sensitive to MIBK, an undercut can be formed when a bi-layer of HMW PMMA on LMW PMMA is exposed to a beam of electrons and subsequently developed.

For forming the small scale contacts, a bi-layer process was used (see Figure 4.5). First, LMW PMMA was spun at 3000 rpm for 1 min onto the cleaned substrate and then baked in the oven at 185 °C for 30 min. Next, HMW PMMA was spun on top of the LMW PMMA and baked again at 185 °C for 30 min. The samples were then transferred into the Raith150 Electron Lithography System and the desired pattern was exposed. After exposing the resist was developed in 1:3 MIBK:IPA for 30 seconds and afterwards rinsed with IPA and blow dried with N₂. Diluting the MIBK in IPA allows for more control over the developing process and results in a smoother line profile. While developing, the bi-layer structure forms an undercut which later on facilitates the lift-off.

The next step was again a thermal evaporation of a 3 nm thick Nichrome and a 15 nm thick gold layer of metal onto the exposed and developed samples. The lift-off was done with acetone, leaving only metal at the desired areas. Figure 4.1 c) shows the result after the small scale contact formation.

Since e-beam lithography is a single write process the wafer could be cut into individual samples using the dicing saw or a diamond scribe prior to the e-beam lithography step.

4.2.4 Formation of the Passivation Layer

Figure 4.6 shows schematically the last step of the formation of a passivation layer and opening (Figure 4.1 d). Once again EBL was used. A HMW PMMA

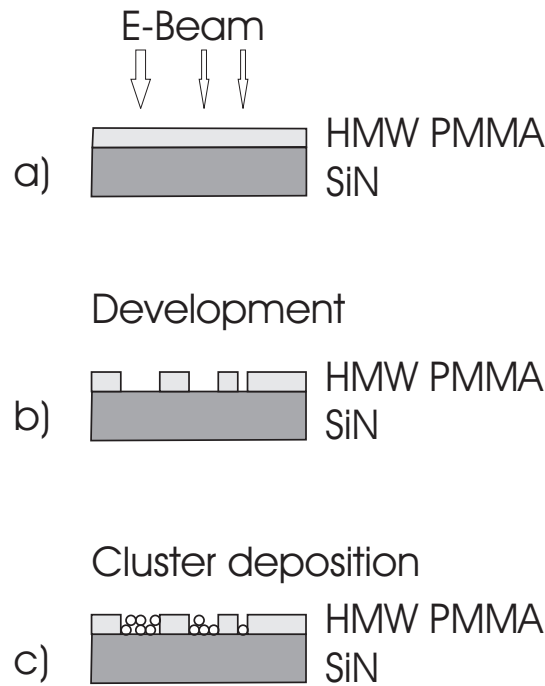


Figure 4.6: Process of the formation of a passivation layer.

was spun on the cleaned wafer (or sample) and baked at 185 °C for 30 min. This layer served as a passivation for the electrodes. The samples were transferred into the Raith150 Electron Lithography System and an opening on top of the small scale contacts was exposed. After exposing, the resist was developed in 1:3 MIBK:IPA for 30 seconds.

The opening within the PMMA passivation layer has to be exactly aligned over the small scale contacts formed in the last step. In photo-lithography, subsequent alignment steps make use of alignment marks to accurately position the next pattern on top of the previous pattern. Using EBL, an alignment mark has to be used as well to precisely align subsequent patterns. This has to be formed/written while forming the small scale contacts.

The whole pattern plus the alignment marks can be seen in Figure 4.4. However, compared to photolithography the alignment marks for EBL are very small. For the precise positioning of nanoscale openings, alignment patterns with similar dimensions to the nanoscale device have to be used. The windmill shaped EBL alignment mark in Figure 4.7 b) is 2 μm wide and high. Each of its ‘wings’ is an isosceles triangle. At least two alignment marks are necessary to allow for translational as well as rotational alignment. To make them easier to find, they are placed in a much bigger alignment box (Figure 4.7 a). The alignment box is 15 μm wide and high.

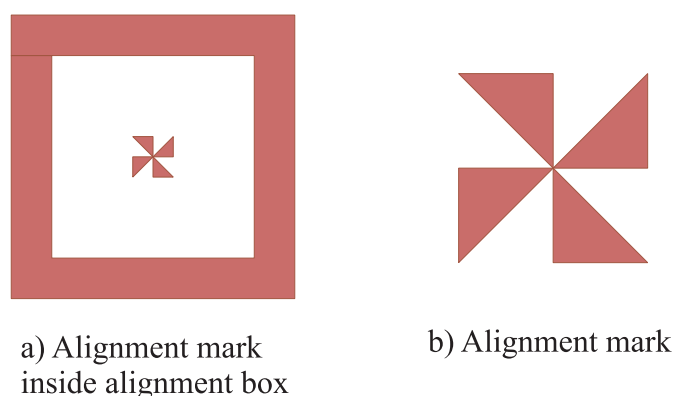


Figure 4.7: Alignment marks used to align the opening in the PMMA passivation layer on top of the small scale contacts.

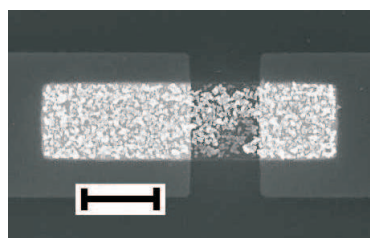


Figure 4.8: Example of a slot sample. The scalebar is $1\mu\text{m}$.

4.3 Sample styles

4.3.1 PMMA-templated Slot Samples

This section describes the usage of poly-methyl methacrylate (PMMA) passivated samples. On top of two narrow metal electrodes separated by a few 100 nm a pattern is exposed and developed into the PMMA passivation layer. These samples are referred to as slot samples and are the proposed sample style for the investigation of FCFs in bismuth cluster assembled devices (Section 1.7.2). Figure 4.8 shows a typical example.

The pattern for the slot samples consists of two fingers separated by a few hundred nanometres as seen in Figure 4.8. It was proposed (Section 1.7.2) that four FCF style devices could fit per sample. However it was found that sometimes the pushpins of the sample stage (Section 2.5) could scratch away the metal of the contact pad and the device was rendered useless. To ensure that a proper connection was made to the pads, the two corner pads (Figure 4.2) are joined which means the contacts could be tested prior to the deposition. This however led to a new design with just two devices per sample. The advantage of having two (or more) nanoscale devices on each sample prepared in the same cluster deposition is that it allows one to compare them with each other. For instance one device can be modified (larger/smaller opening or larger/smaller electrode separation).



Figure 4.9: Example of a four point sample. The scalebar is $1 \mu\text{m}$.

The passivation layer was proposed (Section 1.7.2) to reduce the probability of parasitic conduction across the sample. Only clusters landing within the opening between the contacts are making a connection and clusters landing elsewhere are electrically isolated. As is discussed later (Chapter 5), however it was found that clusters only adhere to the substrate and the metal contacts within the opening in the PMMA (step e) in Figure 4.1). They do not (or to a much lesser degree) adhere to the PMMA. This fact completely eliminates the possibility of parasitic conduction.

4.3.2 Four Point Samples

It was found that contact resistances between the clusters and the metal contacts are very high and dominate the conductance through the nanoscale device. In order to eliminate contact resistances a four point contact layout was used. This section describes the usage of PMMA-templated samples with four small scale contact electrodes (see Figure 4.9). These samples are referred to as four point samples.

The four point samples are similar to the slot samples. In comparison however, four point measurements can be performed. This eliminates the problems with the contact resistances between the clusters and the metal contacts. However, only one device was fitted on each sample in the centre of the large scale contacts (Figure 4.2). Nevertheless, two point resistance measurements can still be performed. In addition, by varying the contact separation between each of the electrodes, length dependent two point resistance measurements are possible. And due to the four point contact layout, up to 6 different such measurements on each sample are possible.

4.3.3 Percolating Film Samples

For this thesis, percolating film samples (Figure 4.10) were used as a measure of repeatable source conditions. This means whether and how fast an onset of conduction occurred for a given source condition. Only if the percolating film sample successfully onset, further deposition onto a nanoscale cluster device have been made. Primarily, the percolating film samples were used for percolation studies [Schulze et al., 2003; Gourley, 2002], hence the name. When a percolating net-

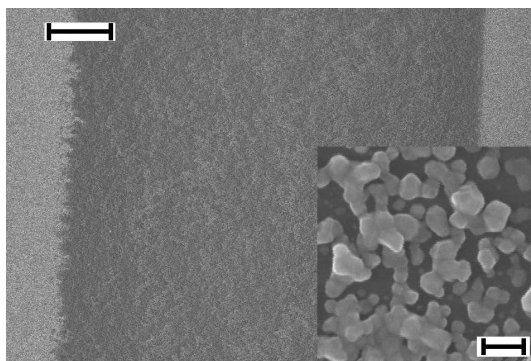
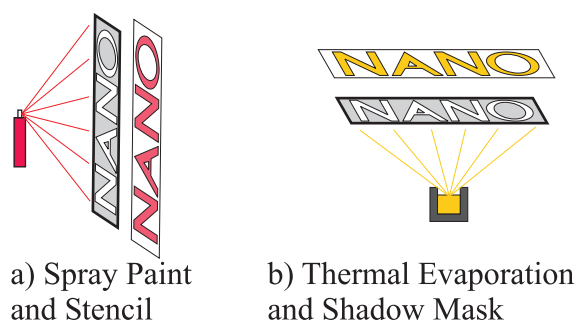


Figure 4.10: A simple percolating film sample with bismuth cluster. The inset shows a magnified area between the contacts. Clearly, the individual cluster can be seen. The scale bar is $10\ \mu\text{m}$ (inset scale bar is $100\ \text{nm}$).



a) Spray Paint and Stencil

b) Thermal Evaporation and Shadow Mask

Figure 4.11: Spray painting with a stencil and thermal evaporation using a shadow mask.

work or path fully extends from one electrode to the other an onset of conduction can be seen.

Fabrication

Percolation film samples are formed on 4" silicon nitride covered wafers (Figure 4.1 a). The percolation film samples have two large contact pads and two contact electrodes with a separation of $1\ \mu\text{m}$ and a width of $1\ \text{mm}$ as seen in Figure 4.10. The inset shows that the film of clusters is sub-monolayer, i.e. not a full coverage.

Unlike the formation of the large scale contacts explained in Section 4.2.2, the fabrication for the percolation film samples made use of a shadow mask. Similar to a stencil used for spray painting where the cut out pattern is transferred onto the paper in paint, the shadow mask transfers a pattern using thermally evaporated metal onto a substrate (see Figure 4.11). The shadow mask (with the desired pattern) was clamped on top of the wafer and mounted inside the thermal evaporator. At a base pressure of 10^{-6} Torr first a sticking layer of $5\ \text{nm}$ Nichrome (80:20 nickel:chrome alloy) was thermally evaporated. This was followed by a thermally evaporated layer of $50\ \text{nm}$ gold.

No further processing (i.e. lift-off and cleaning) was necessary after the shadow mask has been removed from the wafer. The wafer was straightaway cut into individual samples using the previously mentioned dicing saw or a diamond scriber.

The shadow mask can be reused and only eventually needs to be cleaned or have a new wire fitted which determines the electrode separation. The electrodes separation can easily be adjusted by choosing a different gauge wire.

Normally, either no back-gate was necessary or it was simply just scratched into the top layer using a diamond-tip pen and contacted using silver paint. The samples were ready to use after step b) in Figure 4.1.

References

AZ Electronic Materials (2006). URL. www.az-em.com.

Balzers (2006). URL. www.balzers.com.

BOC Edwards (2006). URL. www.bocedwards.com.

Goodberlet, J. G., Hastings, J. T., and Smith, H. I. (2001). Performance of the raith 150 electron-beam lithography system. *J. Vac. Sci. Technol. B*, 19(6):2499.

Gourley, S. (2002). Electronic properties of cluster deposited bismuth nanowires. Master's thesis, University of Canterbury.

Oxford Plasma (2006). URL. www.oxfordplasma.de.

Schulze, M., Gourley, S., Brown, S., Dunbar, A., Partridge, J., and Blaikie, R. J. (2003). Electrical measurements of nanoscale bismuth cluster films. *European Physical Journal D*, 24:291.

Sigma-Aldrich (2006). URL. www.sigmaaldrich.com.

Silicon Quest International (2006). URL. www.siliconquest.com.

Suss MicroTec (2006). URL. www.suss.com.

VEECO (2006). URL. www.veeco.com.

Adhesion of Atomic Clusters

The previous chapters gave an introduction how clusters (and their generic properties) can be used (Chapter 1), how the clusters used for this research were produced (Chapters 2 and 3) and how the samples were fabricated (Chapter 4) to ‘harvest’ the unique properties of clusters. Although it has been said that clusters are deposited onto contacted samples, the assembly method was not mentioned — yet. This chapter explains the key features of the assembly of clusters on PMMA templated samples.

To begin (Section 5.1), a review of cluster surface collisions is given. Since the samples have a PMMA passivation layer, Section 5.2 gives a short summary of the process of the exposure to an electron beam and the subsequent development of PMMA. Using the EBL, the PMMA passivation layer can be exposed to varying dosages. Underexposed PMMA only partially develops leaving behind rough residue. Clusters were deposited into partial exposed and developed PMMA to study the effect on the cluster assembly (Section 5.3). The roughness of the partially exposed and developed PMMA is analyzed in Section 5.4. Section 5.5 discusses the results and concludes this chapter.

5.1 Introduction

In atomic vapour deposition, the atoms are directed towards a surface on which they form a thin film. The growth of the new thin film can be either layer by layer or by island growth. Either way, the kinetic energy of the atoms is relatively small. In addition, the atoms have enough thermal energy to be able to diffuse around the surface before attaching themselves to step edges, impurities or even other atoms.

But what happens when a cluster approaches a surface? — Well, this question cannot be simply answered. Compared to atomic deposition, there are many more parameters involved for cluster depositions. For instance, the size of the clusters can vary and the kinetic energy per atom can cover up to 10 orders of magnitude.

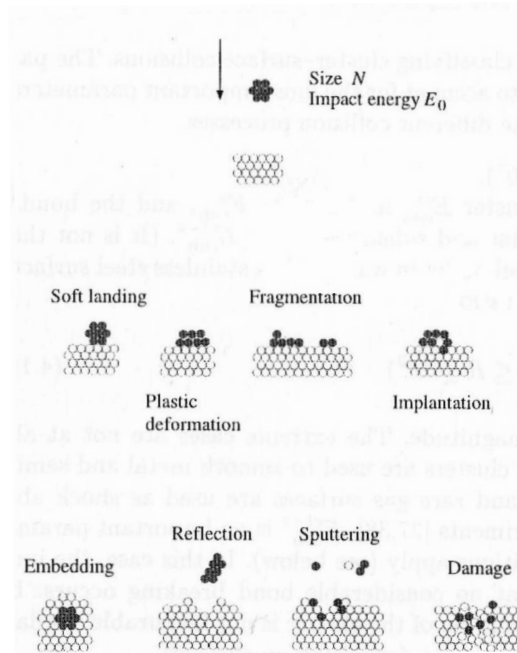


Figure 5.1: Fundamental processes in cluster surface collisions. [Harbich, 2000]

This leads to several different cluster surface interactions. For a detailed overview of the possible scenarios see [Harbich, 2000].

Figure 5.1 shows schematically the fundamental processes in cluster surface collisions. Depending on the momentum of an atomic cluster and its interaction with the surface, it can either soft land, fragment, implant itself or reflect. Soft-landing hereby refers to a low kinetic energy collision where the cluster sticks at the collision site and keeps its initial form. Fragmentation can occur for higher kinetic energy clusters, where the clusters plastically deforms and breaks up. Using even higher kinetic energy the cluster can penetrate soft substrates or reflect off hard substrates. The cases of fragmentation, implantation and reflection usually coexist. Smaller and slower clusters tend to adhere (soft-land), whereas heavier and faster clusters fragment/reflect/implant. This of course is only a qualitative statement without considering the cluster/surface interaction, which also determines whether or not the clusters will bounce or adhere. When colliding with a surface, the clusters (and the surface) can undergo plastic deformation. For instance, clusters can sputter away surface atoms, form impact craters or cause radiation damage.

Another important parameter in cluster surface collision is the cohesion energy. Figure 5.2 shows the reduced impact energy versus the relative binding energies (the cohesive energies) of the surface and the cluster. The fundamental processes in Figure 5.1 only become important for a certain impact energy range and cluster size as indicated in Figure 5.2.

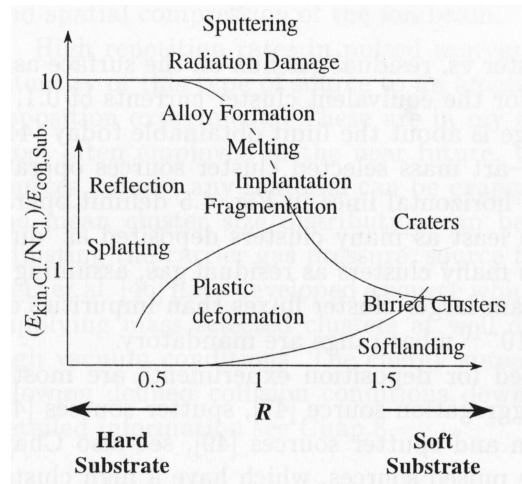


Figure 5.2: Mechanism diagram in cluster surface collisions. Reduced energy vs. relative binding energy $R = E_{coh}^{cl}/E_{coh}^s$. [Harbich, 2000]

Clusters produced using the previously described system (Chapter 2) are characterised as low energetic clusters. Using the inert gas aggregation source, bismuth clusters and antimony clusters were found having an impact velocity of ~ 50 m/s [Partridge et al., 2004].

5.2 PMMA Exposure and Residue

Electron beam lithography is a well established technique. Here are the major steps used to form an opening in the PMMA passivation layer. For the passivation layer a single HMW PMMA layer was used. HMW PMMA is a 2.5% solution of 996k PMMA in chlorobenzene. When spinning the solution at 3000 rpm, it forms a roughly 40 nm thick film of HMW PMMA after the subsequent bakeout at 185 °C for 30 min. The baking drives out the solvent leaving only the HMW PMMA film behind. The samples were then transferred into the Raith150 Electron Beam Lithography System. Here, they were exposed to a focussed beam of electrons. Typical exposure parameters were as follows: 10 kV of acceleration voltage for the electrons, a beam aperture of 30 μm , a distance to the sample of about 6 mm and a beam current of about 150 pA. The exposure dosage then can be adjusted by choosing an appropriate dwell time or area step size, which are interdependent according to Equation 4.1. The dosage is the key parameter characterising the exposure. If exposed, the HMW PMMA molecules break into smaller molecules. Only the small molecules of PMMA are developed away using MIBK. The resist was developed in 1:3 MIBK:IPA for 30 seconds which is sufficient to remove all of the exposed resist.

Figures 5.3 and 5.4 are FE-SEM images and show exposed and developed patterns in HMW PMMA using dosages of 80 $\mu\text{C}/\text{cm}^2$ and 140 $\mu\text{C}/\text{cm}^2$ respectively.

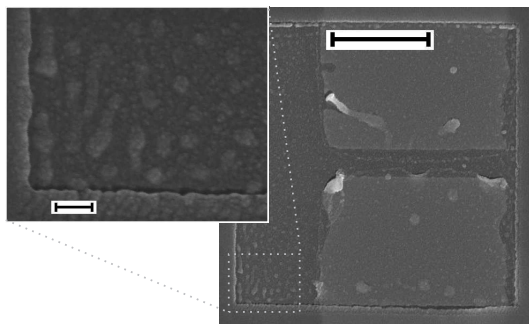


Figure 5.3: A FE-SEM image of a $3 \times 3 \mu\text{m}^2$ opening pattern in PMMA on top of two metal contacts exposed with a dosage of $80 \mu\text{C}/\text{cm}^2$. The left picture shows a detailed view of the edge of the resist at the corner of the opening pattern (the scalebar for the inset is 100 nm).

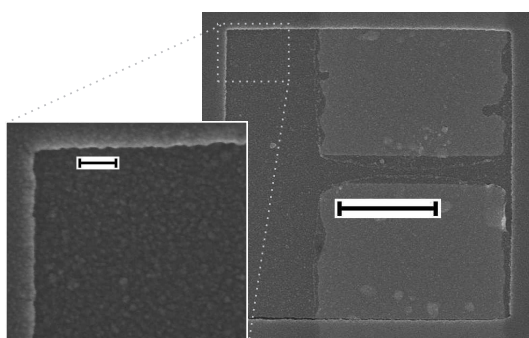


Figure 5.4: A FE-SEM image of a $3 \times 3 \mu\text{m}^2$ opening pattern in PMMA on top of two metal contacts exposed with a dosage of $140 \mu\text{C}/\text{cm}^2$. The left picture shows a detailed view of the edge of the resist at the corner of the opening pattern (the scalebar for the inset is 100 nm).

PMMA is a non-conducting polymer and when imaged using an FE-SEM the surface would charge. To be able to image the exposed and developed patterns using the FE-SEM, a thin gold film of about 5 nm was thermally evaporated onto the samples.

The insert in Figure 5.3 shows that exposing the 40 nm film of HMW PMMA with a dosage of only $80 \mu\text{C}/\text{cm}^2$ leaves some PMMA residue behind. This indicates that not all of the HMW PMMA was broken into small molecules. Using HMW PMMA as the electron beam sensitive resist, it is known that the exposed PMMA is difficult to fully remove. Even correctly exposed and developed PMMA leaves PMMA residue behind [Maximov et al., 2002]. However, a dosage of $140 \mu\text{C}/\text{cm}^2$ (see insert in Figure 5.4) was sufficient to completely convert the whole film of HMW PMMA inside the pattern to smaller molecules, which then were fully developed away. The granular structure of the film in Figure 5.4 is due to the evaporated gold film. Evaporated metal is not completely smooth. Nevertheless, the residue for the $80 \mu\text{C}/\text{cm}^2$ exposure might not be a problem for the cluster deposition.

5.3 Cluster Coverage vs PMMA Exposure

Above, it is shown that a dosage of $140 \mu\text{C}/\text{cm}^2$ leaves a clean aperture within the PMMA film and a dosage of $80 \mu\text{C}/\text{cm}^2$ leaves behind some residue. This section further examines the effect of varying the exposure dosage of HMW PMMA below $80 \mu\text{C}/\text{cm}^2$. Specifically, on how it effects a subsequent cluster deposition.

Before the cluster deposition, samples with HMW PMMA passivation layer were prepared which have $3 \times 3 \mu\text{m}^2$ partially exposed patterns in PMMA layer. The electron beam dosage was varied between $40 \mu\text{C}/\text{cm}^2$ and $80 \mu\text{C}/\text{cm}^2$ in steps of $5 \mu\text{C}/\text{cm}^2$. Those patterns were in the close vicinity of the actual device on the sample on the centre of the sample (less than 0.5 mm away). With an average cluster beam diameter of about 10 mm at the position of the sample a uniform coverage was guaranteed. For this study, antimony clusters and bismuth clusters were used. Both were produced using the IGA source.

5.3.1 Bismuth

The bismuth clusters used for this study were produced with a crucible temperature of $785 \text{ }^\circ\text{C}$ and an inert gas flow of argon of 100 sccm. This resulted in a source pressure of about 22.4 Torr which leads to the production of 30 to 40 nm diameter bismuth clusters. The total deposited thickness of bismuth clusters (as read off the rate deposition monitor) was $21 \pm 3 \text{ nm}$.

Figure 5.5 shows FE-SEM images of a $3 \times 3 \mu\text{m}^2$ pattern with partially exposed and developed PMMA. The resulting coverage for bismuth cluster deposition into those patterns increases with increasing dosage.

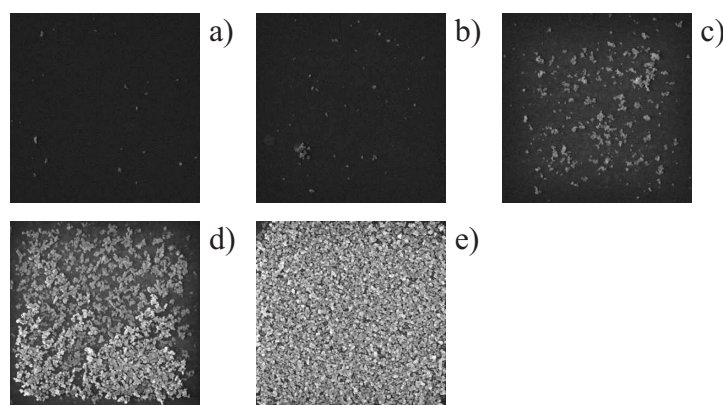


Figure 5.5: FE-SEM images showing qualitatively the variation in coverage of bismuth clusters for varying exposure dosages. a) $40 \mu\text{C}/\text{cm}^2$, b) $50 \mu\text{C}/\text{cm}^2$, c) $60 \mu\text{C}/\text{cm}^2$, d) $70 \mu\text{C}/\text{cm}^2$, e) $80 \mu\text{C}/\text{cm}^2$. The total deposited thickness was 21 ± 3 nm.

In the case of a dosage of $40 \mu\text{C}/\text{cm}^2$ (Figure 5.5 a), almost no bismuth clusters are visible. At a dosage of $60 \mu\text{C}/\text{cm}^2$, more clusters can be seen in the centre of the pattern, which again increases for the $70 \mu\text{C}/\text{cm}^2$ case. It seems that the exposure of HMW PMMA at the middle of the pattern is more effective than at the edges. This is understandable if secondary electrons are considered. Those cause further exposure within the PMMA and increase the effective dosage for the inner part of the patterns. PMMA exposure is a cumulative process.

From a dosage of $80 \mu\text{C}/\text{cm}^2$ onwards, a fully filled pattern is achieved. Note that the measured thickness (as read off the rate deposition monitor) is different from the actual thickness on the sample due to different bouncing characteristics of the clusters on the monitor and the substrate respectively.

5.3.2 Antimony

The antimony clusters used for this experiment were produced having a crucible temperature of $650 \text{ }^\circ\text{C}$, source pressure of 6.8 Torr and a mixture of 40 sccm helium and 40 sccm argon.

Figures 5.6 and 5.7 are FE-SEM images showing $3 \times 3 \mu\text{m}^2$ partially exposed and developed PMMA patterns. The dosages vary from 45 to $75 \mu\text{C}/\text{cm}^2$ and from 40 to $80 \mu\text{C}/\text{cm}^2$ in steps of $10 \mu\text{C}/\text{cm}^2$ respectively. The two figures (Figure 5.6 and Figure 5.7) are from two different depositions with slightly different total deposited thicknesses. The images in Figure 5.6 have a higher total thickness than the images in Figure 5.7. Similar to the case of bismuth, the resulting coverage of antimony clusters increases with increasing dosage.

Antimony clusters and bismuth clusters adhere differently to a given substrate. It is found empirically that antimony clusters are more likely to reflect and bismuth clusters tend to adhere. Nevertheless, if one antimony cluster happens

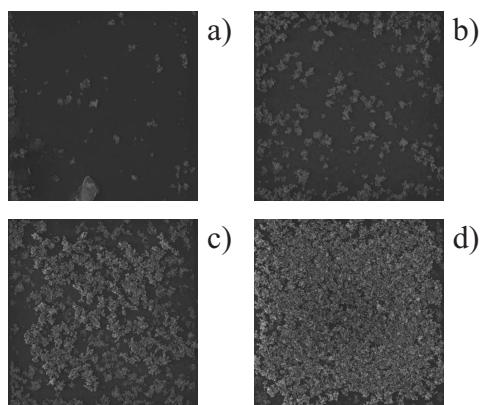


Figure 5.6: FE-SEM images showing qualitatively the variation in coverage of antimony clusters for varying exposure dosages. a) $45 \mu\text{C}/\text{cm}^2$, b) $55 \mu\text{C}/\text{cm}^2$, c) $65 \mu\text{C}/\text{cm}^2$, d) $75 \mu\text{C}/\text{cm}^2$. The total deposited thickness is 34 ± 3 nm.

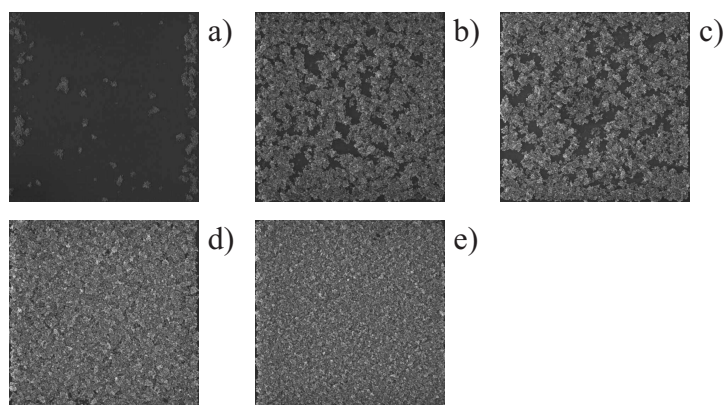


Figure 5.7: FE-SEM images showing qualitatively the variation in coverage of antimony clusters for varying exposure dosages. a) $40 \mu\text{C}/\text{cm}^2$, b) $50 \mu\text{C}/\text{cm}^2$, c) $60 \mu\text{C}/\text{cm}^2$, d) $70 \mu\text{C}/\text{cm}^2$, e) $80 \mu\text{C}/\text{cm}^2$. The total deposited thickness is 21 ± 3 nm.

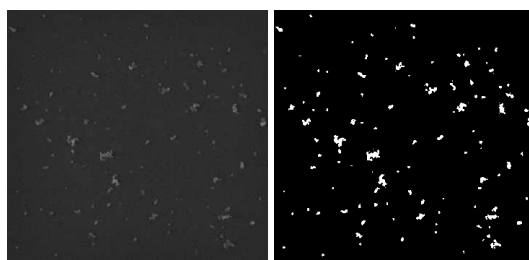


Figure 5.8: Bismuth clusters in a $3 \times 3 \mu\text{m}^2$ partially exposed patterns in PMMA for an exposure dosage of $55 \mu\text{C}/\text{cm}^2$. Left image shows the original FE-SEM image and right image is the binarised version of the same image.

to adhere it provides a 'soft-landing' site to further antimony clusters forming clumps of clusters (as can be seen in Figures 5.6 and 5.7).

5.3.3 Quantitative Study

The previous two sections qualitatively showed that cluster coverage increases with PMMA exposure dosage. To derive a quantitative relationship between the cluster coverage and the PMMA exposure the cluster coverage in the FE-SEM images in Figures 5.5, 5.6 and 5.7 are quantified using image processing.

Firstly, the images are individually converted into black and white images (binarised) by choosing a threshold grey value so that the shape of the cluster patterns within the image is still preserved (see Figure 5.8). As can be seen in Figure 5.8, the clusters in the original FE-SEM picture were transferred into white pixels whereas the surrounding substrate is converted into black pixels. Then, the number of black and white pixels is counted using image analysis software. The binarisation is done to be able to convert the number of white pixel to black pixel into a percentage surface coverage number.

Figures 5.9 and 5.10 show the results of this image analysis for the case of bismuth clusters and antimony clusters respectively. In both cases, increasing the exposure dosage results in increased cluster coverage as was found previously. A clear onset or strong increase can be seen in the coverage. At the exposure dosage, which corresponds to this onset, the whole thickness of the HMW PMMA film was turned into smaller molecules, which in turn could be developed away to expose the underlying substrate. Once the substrate is exposed, the coverage increases strongly. For bismuth clusters that onset was very pronounced at about $65 \mu\text{C}/\text{cm}^2$. Antimony clusters showed an onset only slightly lower at about $60 \mu\text{C}/\text{cm}^2$.

At a dosage of $140 \mu\text{C}/\text{cm}^2$ it is thought that all of the PMMA is developed away and full coverage can be assumed. The coverage for an exposure dosage of $140 \mu\text{C}/\text{cm}^2$ therefore is set to unity in the graphs.

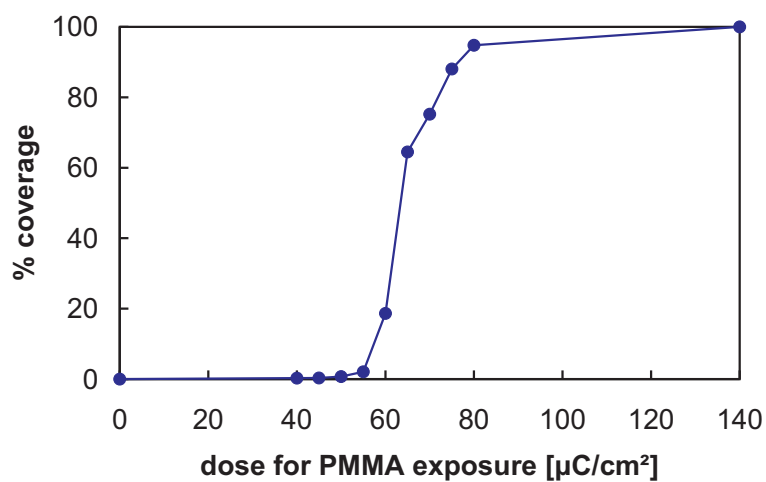


Figure 5.9: Variation in coverage (quantitatively) of bismuth clusters for varying exposure dosages. The total deposited thickness is 21 ± 3 nm.

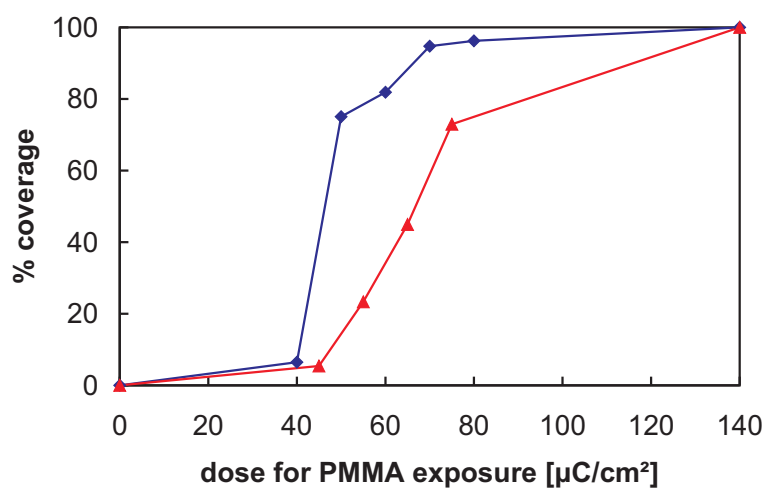


Figure 5.10: Variation in coverage (quantitatively) of antimony clusters for varying exposure dosages. The total deposited thickness is 54 ± 6 nm (\diamond) and 34 ± 1 nm (\triangle).

5.4 RMS Roughness vs PMMA Exposure

As is shown previously, the adhesion of clusters depends very strongly on whether the PMMA was partially exposed and developed. Partially exposed and developed PMMA is very rough. Using the AFM, the evolution of the rms (root mean square) roughness of partially exposed and developed HMW PMMA is investigated.

A HMW PMMA passivation layer was spun onto a silicon nitride top layer sample in the same fashion described previously (Section 5.3). Then the sample was transferred again into the Raith150 Electron Beam System and patterns were exposed only varying the dosage between each pattern. The electron beam dosage was changed between 40 and 80 $\mu\text{C}/\text{cm}^2$ in steps of 5 $\mu\text{C}/\text{cm}^2$. All 9 patterns were on the same sample. After the exposure, the patterns were developed in 1:3 MIBK:IPA for 30 seconds, rinsed with IPA and blow dried with N_2 .

Roughness studies of HMW PMMA were done using the Atomic Force Microscope (AFM) in the Electrical and Computer Engineering Department at the University of Canterbury (Section 4.1.2). A total of 11 AFM images were taken, one for each of the 9 patterns mentioned previously, one of an unexposed but developed HMW PMMA film and one of a cleaned silicon nitride substrate. The unexposed but developed pattern is assumed to have an exposure dosage of 0 and the cleaned silicon nitride substrate is assumed to have an exposure dosage of 140 $\mu\text{C}/\text{cm}^2$.

Figure 5.11 shows the AFM images of the partially exposed patterns. The image for a dosage of 0 (Figure 5.11 a) was taken at the edge of the sample of unexposed but still developed HMW PMMA. As for the highest dosage of 140 $\mu\text{C}/\text{cm}^2$, the image was taken of a clean silicon nitride top layer sample for comparison. As can be seen, unexposed PMMA is very smooth. Increasing the exposure dosage lead to an increase in roughness (see Figures 5.11 b-c). At a dosage of about 70 $\mu\text{C}/\text{cm}^2$ (Figure 5.11 e), the underlying substrate becomes visible. Similar to the samples prepared in Section 5.2, at 80 $\mu\text{C}/\text{cm}^2$ (Figure 5.11 f) there was still some PMMA residue left behind. The as cleaned silicon nitride top layer was very smooth having only small particles left behind.

The FE-SEM only produces 2D images (see Figures 5.3 and 5.4) and only allowed a qualitative statement. With the AFM it is possible to accurately measure heights. This allows qualitative statements about the images in Figure 5.11, to be converted into a more quantitative form. For each of the total 11 AFM images the height information was transformed into a rms roughness value using the AFM image software. The area over which the roughness value was determined was selected objectively. Occasionally, a small particle or surface defect or PMMA residue was found and was not included in the selected area when calculating the rms roughness.

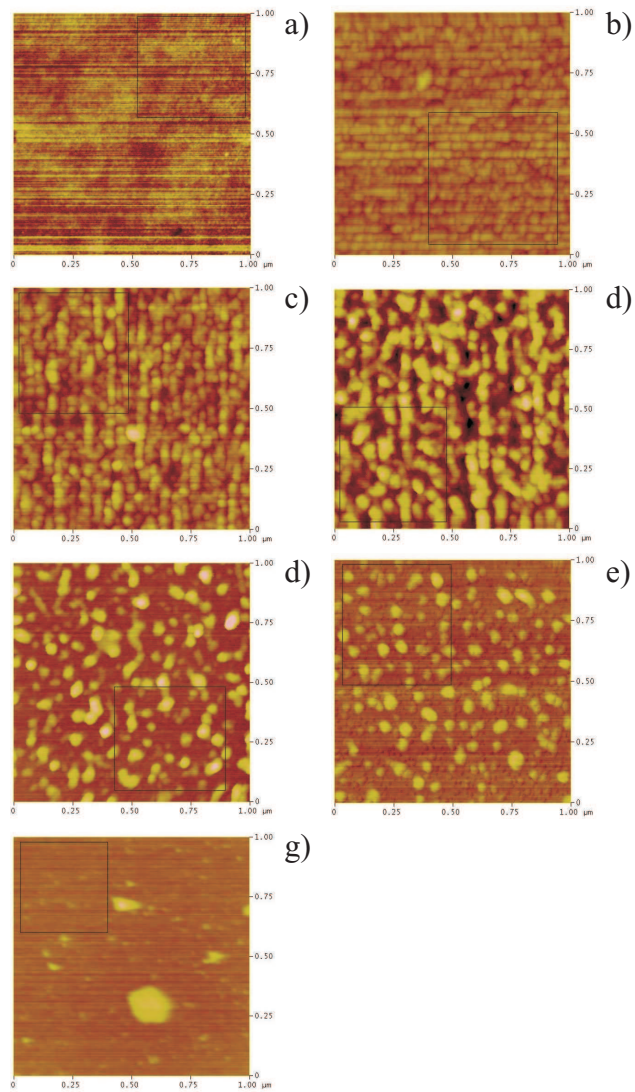


Figure 5.11: AFM images of partially exposed and developed HMW PMMA for varying exposure dosages. a) 0 or unexposed PMMA, b) 40 $\mu\text{C}/\text{cm}^2$, c) 50 $\mu\text{C}/\text{cm}^2$, d) 60 $\mu\text{C}/\text{cm}^2$, e) 70 $\mu\text{C}/\text{cm}^2$, f) 80 $\mu\text{C}/\text{cm}^2$, g) 140 $\mu\text{C}/\text{cm}^2$ or cleaned substrate.

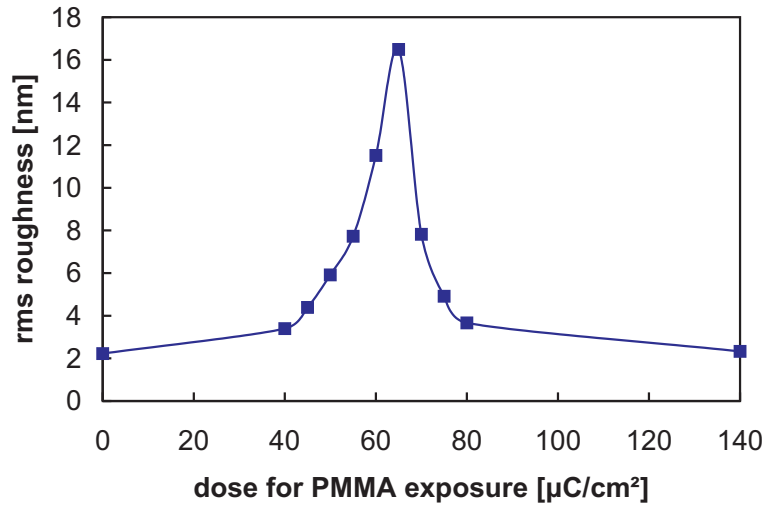


Figure 5.12: RMS roughness of HMW PMMA, as measured using the AFM imaging software, for varying exposure dosages.

Figure 5.12 shows the rms roughness values for the different exposure dosages found using this method. As can be clearly seen, the rms roughness for unexposed PMMA is the same as for a clean silicon nitride top layer sample. With increasing exposure dosage the roughness steeply increases and reaches a maximum at about $65 \mu\text{C}/\text{cm}^2$. For exposures higher than $65 \mu\text{C}/\text{cm}^2$ the underlying silicon nitride substrate becomes visible and the rms roughness value decreases.

5.5 Discussion and Conclusion

5.5.1 Discussion

It was found for cluster depositions of 30 to 40 nm bismuth clusters (and anti-mony clusters) that there is a high selectivity between the passivation layer of HMW PMMA and the substrate visible within the patterns. Furthermore, partially exposing and developing PMMA leaves resist residue behind. The cluster coverage for a given total thickness increases with increasing exposure dosage. The rms roughness for partially exposed and developed HMW PMMA peaks at a dosage of about $65 \mu\text{C}/\text{cm}^2$.

It can be argued that the increase in cluster coverage with dosage is to do with the increase in rms roughness at least until the maximum in the roughness value at $65 \mu\text{C}/\text{cm}^2$. A rougher surface automatically provides more first landing sites and then subsequent clusters can adhere (via soft-landing). However, the rms roughness decreases for further increase with exposure dosage. Which is expected too, since the underlying substrate is a commercially available silicon nitride top layer silicon wafer.

The cluster coverage increases further with increased exposure dosage for both bismuth and antimony. This cannot just be explained by roughness alone. In addition, unexposed HMW PMMA and clean silicon nitride both have a rms roughness value of about 2 nm. Clearly, the cluster coverages are strikingly different for silicon nitride (uniform coverage) and for the unexposed PMMA (clean surface). It is therefore clear that the surface material itself plays a major role on how and if a cluster adheres to it.

Considering this, it is possible to explain the further increase in coverage after the maximum peak in rms roughness. For exposure dosages higher than $65 \mu\text{C}/\text{cm}^2$ the underlying substrate becomes visible and changes the adhesion behaviour dramatically. For higher dosages, more substrate is available for the interaction with the clusters, hence increasing the coverage.

5.5.2 Simulational Studies

This section briefly outlines simulational studies of clusters with surfaces also showing reflection and adhesion of clusters. The simulation results led to an interpretation, which is based on plastic deformation.

In the simulation a 147-atom solid icosahedral cluster collides with a (111) fcc surface. All atomic interactions are described using a standard Lennard-Jones (LJ) potential. The interaction strength between the cluster and surface atoms was varied by multiplying the attractive term of the LJ potential with a prefactor C in the ranges of 0 and 1. A detailed description of the simulation can be found elsewhere [Awasthi et al., 2006].

Figure 5.13 shows the result for the simulation for various values of C . The velocity is in units of $(\varepsilon/m)^{0.5}$ with ε the LJ energy of one interatomic bond and m the atomic mass. For each of the points in Figure 5.13 fifty trial simulations with randomly selected cluster orientations were run. For each simulation it was determined whether the cluster adhered to the surface or reflected off the surface. The adhesion probability gives the percentage of clusters that adhered to the surface after the collision simulation.

As can be seen in Figure 5.13 the probability of adhesion for strongly interacting clusters (solid squares or $C = 0.7$) is always 1. Less interacting clusters (open squares or $C = 0.25$) reflect for high velocities. For all strength interactions, in the case of very low incident velocities soft-landing occurs, which means the clusters adhere. For a fixed value of C increasing the velocity means a change from elastic to plastic deformation.

At a velocity v_0 of $0.5(\varepsilon/m)^{0.5}$ the onset of a plastic deformation regime occurs. In the case of plastic deformation and for a fixed velocity the cluster interaction can be changed from adhesion to reflection by changing the interaction C from 0.7 to 0.2. As mentioned previously, the interaction term C determines the strength of the interaction between cluster and surface atoms. From the simulation results

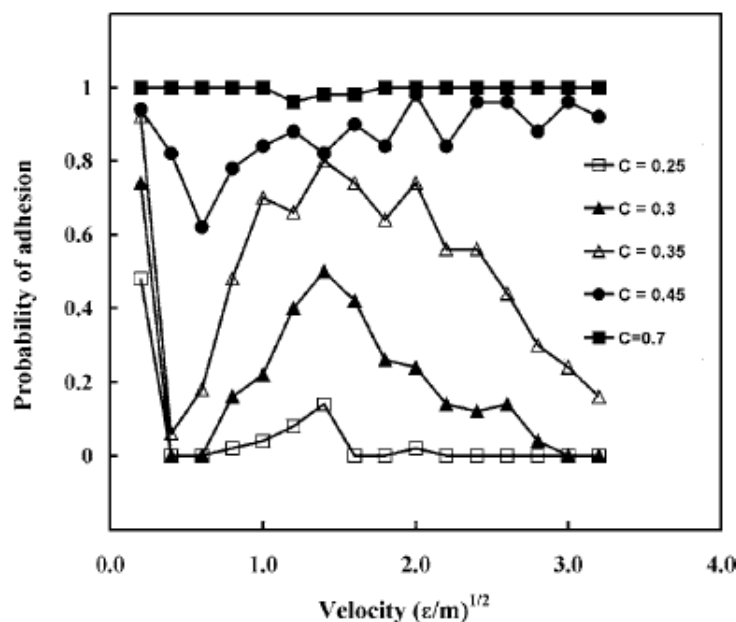


Figure 5.13: Adhesion probability of a cluster with varying impact velocity.

it can be seen that for high velocities the greatest differences in the probabilities of adhesion occur. That means that the reflection of clusters can be changed by changing the substrate the clusters collides with.

5.5.3 Conclusion

In conclusion, the cluster coverage for 30 to 40 nm bismuth clusters or for 30 nm antimony clusters can be influenced effectively by adjusting the exposure dosage of HMW PMMA. The cluster coverage of bismuth clusters and antimony clusters increases for increased exposure dosage of the PMMA layer less than $65 \mu\text{C}/\text{cm}^2$ due to the increase in roughness of the PMMA. The further increase of coverage, even though the roughness is decreasing, is due to the exposure of the silicon nitride substrate. Silicon nitride provides a higher adhesion probability which is greater than the adhesion probability of PMMA. This leads to a high selectivity between unexposed PMMA and clean substrate. The surrounding PMMA passivation layer is almost cluster free. A high selectivity is achieved between the slot (substrate and metal) and the PMMA.

With electron-beam lithography, not only rectangular openings but also arbitrarily shaped patterns can be written and formed in the PMMA. Using this and the previously mentioned high selectivity between the PMMA and the developed patterns one can create a map of New Zealand made of clusters.

Figure 5.14 shows the map of New Zealand filled with bismuth clusters and in Figure 5.15 the map of New Zealand is filled with antimony clusters. As for the bismuth case, almost no clusters can be found on the surrounding PMMA

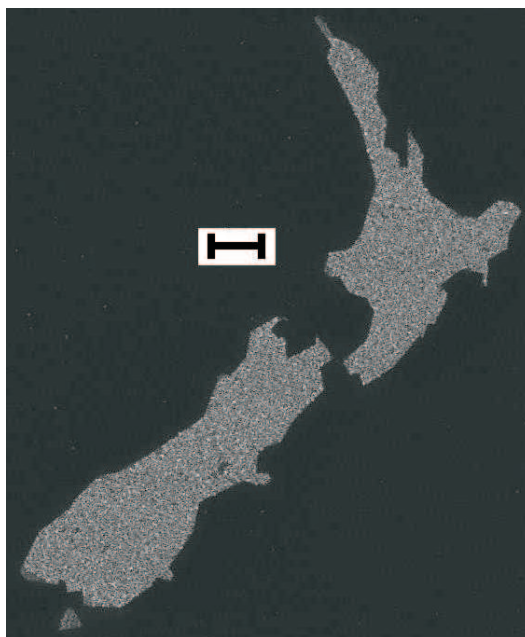


Figure 5.14: Bismuth clusters deposited into an aperture in HMW PMMA shaped like the map of New Zealand. The scalebar is 1 μm .

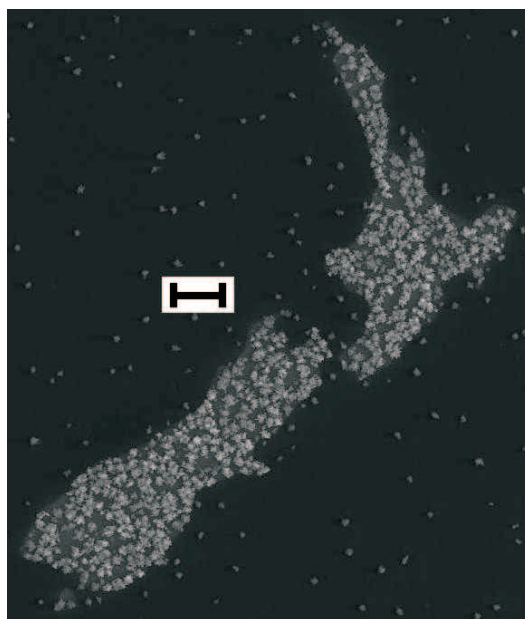


Figure 5.15: Antimony clusters deposited into an aperture in HMW PMMA shaped like the map of New Zealand. The scalebar is 1 μm .

layer. This is mainly because the bismuth clusters adhere readily to the substrate but not so to the PMMA. However, the antimony clusters self-assemble in a different fashion. Here, the clusters assemble mainly by soft-landing. This means, antimony clusters tend to adhere to themselves. So if for some reason an antimony cluster is trapped on a surface defect subsequent antimony clusters adhere to it more readily than to the surface. It is for this reason that the antimony clusters form clumps of clusters rather than a complete film of clusters like bismuth.

The assembly method presented here led to a novel way of fabricating cluster assembled devices [Reichel et al., 2006a]. Further investigation were done involving not only bismuth and antimony clusters but also copper clusters produced using the magnetron sputter source [Reichel et al., 2006b]. The adhesion of the clusters to different surfaces, which are common to device fabrication, were studied. The surfaces include silicon oxide and silicon nitride substrates as well as polymers like photo resist and electron beam resist. The results were compared to molecular dynamic simulations (see Section 5.5.2). It was found that reflection or adhesion of clusters on surfaces is a result of the plastic deformation of the cluster.

References

- Awasthi, A., Hendy, S. C., Zoontjens, P., and Brown, S. A. (2006). Reentrant adhesion behavior in nanocluster deposition. *Phys. Rev. Lett.*, 97:186103.
- Harbich, W. (2000). *Metal Clusters at Surfaces*, chapter 4: Collision of Clusters with Surfaces, pages 107–150. Cluster Physics. Springer-Verlag.
- Maximov, I., Zakharov, A. A., Holmquist, T., Montelius, L., and Lindau, I. (2002). Investigation of polymethylmethacrylate resist residues using photoelectron microscopy. *J. Vac. Sci. Technol. B*, 20(3):1139.
- Partridge, J. G., Brown, S. A., Dunbar, A. D. F., Kaufmann, M., Scott, S., Schulze, M., Reichel, R., Siegert, C., and Blaikie, R. J. (2004). Template-assembled antimony cluster mesowires and nanowires. *IEEE Transactions on Nanotechnology*, 3:61.
- Reichel, R., Partridge, J. G., and Brown, S. A. (2006a). Nanoscale and microscale lithography methods and resultant devices. New Zealand Patent Application No. 541209/547784. Patent Application lodged 8 July 2006.
- Reichel, R., Partridge, J. G., Natali, F., Matthewson, T., Brown, S. A., Lasseson, A., Mackenzie, D. M. A., Ayesh, A. I., Tee, K. C., Awasthi, A., and Hendy, S. C. (2006b). From the adhesion of atomic clusters to the fabrication of nanodevices. *Appl. Phys. Lett.*, 89(21):213105.

Electrical Measurements

Following the investigation of adhesion of clusters presented in Chapter 5 the focus is now shifted to the electrical characterisation of cluster assembled devices. In Section 6.1 key notes on the evolution of cluster assembled devices are given. It explains briefly the major steps prior to the electrical characterisation of cluster assembled devices as well as evolutionary changes in sample design.

In nanoscale devices the connection from the (contact) electrode to the cluster assembled structure plays a major role. Section 6.2 analyses the effect of silver contacts compared to gold contacts on the conduction of bismuth cluster films.

The sample design proposed (Section 1.7.2) did not prove to be successful for electrical measurements. It needed to be adjusted and modified to yield measurable cluster assembled devices. In Section 6.3 key changes to the design are presented for bismuth and antimony cluster devices before the results of the electrical measurements using slot samples are shown.

As seen in the conclusion of Chapter 5, using PMMA as a passivation layer it is possible to form arbitrary shaped patterns. One such arbitrary pattern is the design of a four point contact layout filled with clusters. The results on the electrical measurements of the cluster contact four point samples are given in Section 6.4.

A four point contact layout is of advantage when measuring nanoscale devices and a four point sample design with metallic contacts was used to measure four point resistances of cluster assembled devices (see Section 6.5).

Most nanoscale cluster devices investigated during this thesis had non-linear $I(V)$ characteristics. Section 6.6 discusses what causes non-linear $I(V)$ s for the investigated samples and explains for a few individual samples the conductance mechanism involved. An attempt to fit the $I(V)$ data to existing theory follows in Section 6.7.

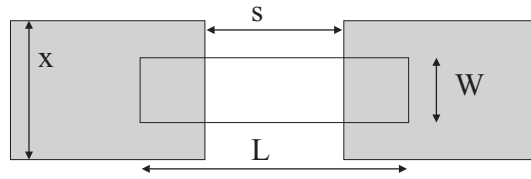


Figure 6.1: Schematic layout of a slot sample. x = electrode width; s = electrode separation, W = opening (slot) width, L = opening (slot) length.

6.1 Preliminary Samples

The sample layout intended to investigate FCFs was presented (Section 1.7.2) and it was shown how such samples are made (Chapter 4). However, proposing a sample design and making it still bears the problem that it has to be tested in real life on an actual system. Now even though FCFs samples were prepared, depositing clusters onto them and being able to measure something proved difficult.

In addition to the tests done to characterize the cluster apparatus, the layout of the electrically contacted samples was tested during cluster experiments and further refined. Figure 6.1 shows schematically the opening (slot) on top of two electrodes and the characteristic lengths: the contact electrode width x , the electrode separation s , slot width W , and slot length L . In the proposed sample layout (Section 1.7.2) the device was planned to have a contact separation s of a few 100 nm; ideally < 10 clusters wide. The width W of the opening in the passivation layer should ideally be such that only a chain of clusters (one cluster wide) can bridge the contact separation. The opening should be positioned on top of the small scale electrodes only having an opening pattern to just span the contact separation, i.e. $L \simeq s$.

To be able to exactly position the opening in the PMMA, sample alignment during the EBL writing process has to be perfect. As can be seen in Figure 6.1, adjustment for alignment errors can be made by widening the electrode width x and increasing the length L of the opening. Those adjustments allow for small alignment errors in the x- and the y-direction without changing the functionality of the proposed device. The electrode width x was increased to about $2 \mu\text{m}$ and the length of the opening L was increased to at least three times the contact separation s .

The increased width x of the contact electrodes however made it difficult to keep the contact separation s of a few 100 nm. With the EBL system used here it is possible to achieve features down to 17 nm [Goodberlet et al., 2001]. This is for patterning of thin metallic leads only. The contact separation s however is between two electrodes formed using EBL. Due to stray secondary exposure, the region of the small contact separation s is exposed so that the PMMA within this gap is developed away as well. In the subsequent metallisation a filament

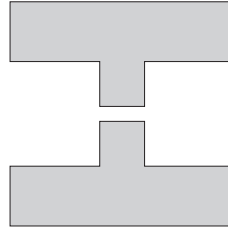


Figure 6.2: Schematic layout of a percolating film sample used during this thesis. Two electrodes are separated by a $100\ \mu\text{m}$ gap.

of metal would bridge the gap rendering the device useless. This meant that the contact separation s was increased to at least $250\ \text{nm}$. Further discussion on changes of contact separation s , opening width W and opening length L follow in Section 6.3.

6.2 Percolating Film Samples

For this thesis percolating film samples (Section 4.3.3) were mainly used to characterize the source conditions before additional depositions were made onto either slot samples or four point samples. They are different from the percolating film samples based on interdigitated contacts used previously (Section 1.4 and [Schulze et al., 2003; Gourley, 2002; Schmelzer Jr., 2001; Schmelzer Jr. et al., 2002]). The samples used for this thesis had just two electrodes with a separation of $100\ \mu\text{m}$ (see Figure 6.2). For a given source condition the percolating film sample should onset at the expected cluster thickness around the percolation threshold p_c . This is to indicate that ideal cluster source conditions were achieved. Usually, apart from the onset data no further measurement was done on the percolating film samples.

This section however, describes the usage of percolating film samples (Figure 6.2) for another purpose, i.e. to investigate the issue of contacting bismuth to gold contacts (see Section 1.8). Gold has a workfunction of $5.1\ \text{eV}$ and when in contact with bismuth a barrier for electrons is expected (Section 1.8). Different contact metals having different workfunctions could change the overall conductance through cluster assembled devices. To investigate the effect of the contact metal on the overall conduction simple percolating film samples were prepared (Section 4.3.3). Apart from the standard gold contacts, silver contacts were used. Silver has a workfunction of $4.26\ \text{eV}$ [Stöcker, 1994] which is close to the workfunction of bismuth of $4.22\ \text{eV}$ [Stöcker, 1994]. Being able to connect bismuth clusters to a contact metal with a lower workfunction should decrease the expected barrier height.

Sample	Time to Onset [sec]	Deposition Rate [Å/sec]	Final Thickness [nm]
Au1	245	0.70	17.2
Ag1	245	0.71	17.4
Au2	255	0.66	16.8
Ag2	270	0.66	17.8
Au3	270	0.68	18.4
Ag3	285	0.70	20.0

Table 6.1: Deposition details of the percolating film samples mentioned in Section 6.2.

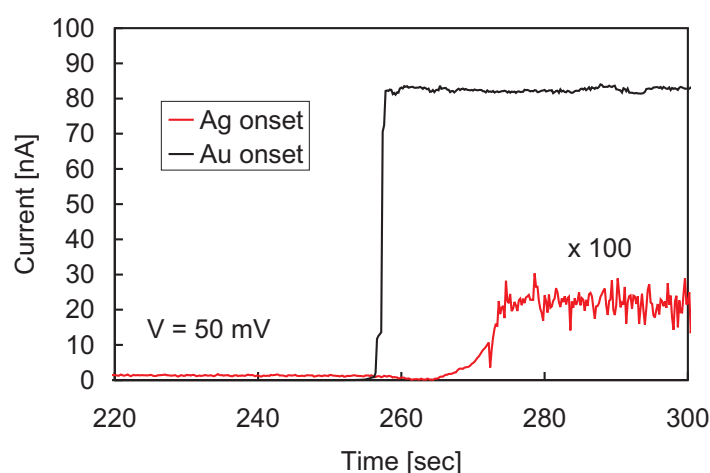


Figure 6.3: Onset curves for samples Ag2 (red line) and Au2 (black line). Note: the current for Ag2 is multiplied by a factor of 100 for clarification.

6.2.1 Deposition Details

Two electrically contacted samples per deposition run, one with gold contacts and one with silver contacts respectively, were deposited onto with bismuth clusters. An inert gas flow of 100 sccm of argon assisted the formation of bismuth clusters from the crucible. The crucible temperature was held at a temperature of about 790 °C. The source pressure during deposition was 24 Torr. Once an onset of conduction was achieved the deposition was stopped. Onset times, deposition rate and subsequent thickness of the films can be found in Table 6.1.

The onset of conduction in a percolating film sample marks the point when a percolating network spans from one side (contact 1) to the other (contact 2). Electrically, this is indicated by a steep decrease in resistance (sharp increase in conductance). The time between registering an onset and closing the shutter is less than 5 seconds (corresponds to a thickness of less than 0.5 nm). Figure 6.3 show typical onset curves. The resistance for the gold contacted sample decreased from about $10^{10} \Omega$ to just a few hundreds of $k\Omega$. The resistance for the silver contacted sample decreased as well, however only to about a few hundreds of $M\Omega$.

Sample	Onset Resistance [k Ω]	Final Resistance [k Ω]	Ratio
Au1	110	40	2.9
Ag1	205	24	8.6
Au2	610	83	7.3
Ag2	265000	NA	NA
Au3	919	460	2.0
Ag3	370	27	13.5

Table 6.2: Onset resistances and resistances after a 10 V ramp anneal.

Typically, the onset resistances of percolating film samples are in the range of a few hundreds of k Ω . Table 6.2 lists the initial resistances of all the investigated samples. The final resistances in that table are the post-annealed resistances as explained shortly.

Interestingly, as can be seen from Table 6.1, the onset time for all the percolating film samples are quite similar with no difference between the samples with different contact metals. The final thicknesses of the percolating films were between 17 nm and 20 nm. Having average cluster sizes of 25 nm to 30 nm this is a coverage of about 60% to 80%. The percolation threshold for an infinite large 2D lattice is $p_c = 0.5927461$ [Newman and Ziff, 2000]. For a continuum model $p_c = 0.676339$ for a 2D continuum of discs [Quintanilla et al., 2000], $p_c = 0.6254$ for 2D continuum of randomly oriented squares [Baker et al., 2002] or $p_c = 0.6666$ for a 2D continuum of aligned squares [Baker et al., 2002]. As mentioned previously, similar onset times for the percolating film samples indicate repeatable source conditions.

6.2.2 Annealing

Once deposited, $I(V)$ measurements and gate measurements were performed. However, the gate measurements did not show any effect. Several $I(V)$ measurements were taken, where subsequently the maximum voltage for the $I(V)$ characteristics was increased from 100 mV, to 1 V, 3 V, 5 V, 7 V and 10 V. It was noted that for increased maximum voltage sweeps the resistance was decreasing step-wise to a lower final value.

Figure 6.4 shows this phenomena for sample Ag1. Previously, a voltage ramp up to 3 V was performed on this sample and in Figure 6.4 the slope is linear for voltages less than 3 V. Once 3 V is exceeded, significant steps occur at 3 V and 4 V (with several more after that as well) indicating a lowering of the resistance. The $I(V)$ characteristics were linear after the maximum voltage was reached, i.e. no more steps were observed when decreasing the voltage. Note: Ag2 did not have a linear $I(V)$ and will be discussed separately later.

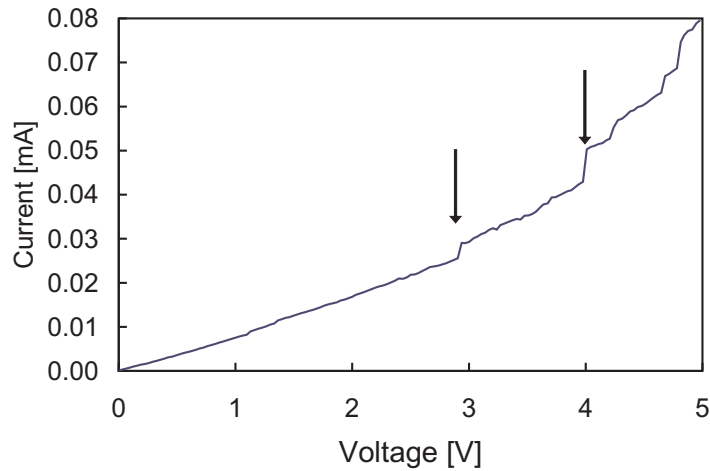


Figure 6.4: $I(V)$ characteristic for sample Ag1. Here, the voltage was ramped up to 5 V having previously only performed 3 V ramps. Arrows at 3 V and 4 V mark steps in the resistance.

Table 6.2 gives the initial resistances for the samples and their final resistance after a 10 V ramp. As can be seen, the samples had initial resistances below 1 M Ω (except sample Ag2). After the 10 V ramp the resistances decreased for all of the samples by at least a factor of 2 and in general down to resistances of less than 100 k Ω — apart from sample Au3 which had had a very high onset resistance to begin with.

If the film is considered a percolating network, the onset is characterized by the formation of several current paths. Since the paths consist of individual clusters bottlenecks form at the interconnect between clusters, which dominate the resistance due to scattering. Now, increasing the voltage also increases the current through the current paths and locally (at bottlenecks) resistive heating occurs. Local heating can then improve the conductance through the whole film by assisting in the coalescence of the two (or more) neighbouring clusters. Bismuth has a very low melting point of 271.3 $^{\circ}\text{C}$ [Stöcker, 1994], which means that even relatively low currents could melt the bismuth, especially at the high resistive bottlenecks of conduction.¹ The current needed to assist the coalescence is by no means the current through the whole film, but is much lower. At percolation it is considered that many parallel current paths exist where the high conducting paths would carry most of the current. However, local heating of a high resistive current path parallel would render it high conducting as well and the overall current through the cluster film increases.

The size of this effect depends on how many of such current paths exist within the percolating film. The relatively high onset resistance of sample Au3 for

¹For instance, a current of 2 μA could melt a bismuth cluster filled slot (3 $\mu\text{m} \times 200 \text{ nm} \times 50 \text{ nm}$) with a resistance of about 1 M Ω completely within 1 μs even using assuming heat loss to the silicon substrate.

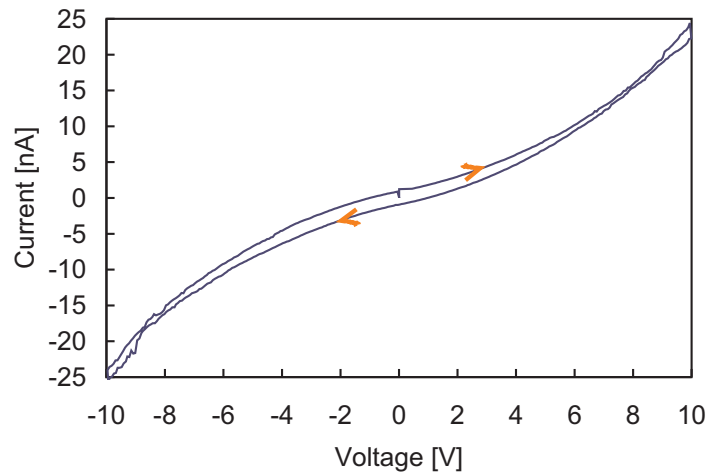


Figure 6.5: $I(V)$ characteristic for sample Ag2. It shows a non-linear $I(V)$.

instance indicates that at onset fewer current paths were formed than compared with the other samples (Table 6.1). Deposition of clusters is random and will certainly differ from sample to sample. Applying a high voltage improved (i.e. lowered) the resistance of the investigated percolating film samples (Table 6.1) by at least a factor of 2 (Table 6.2).

6.2.3 Sample Ag2

In this particular subset of samples (Table 6.2) the sample Ag2 is special. It had the highest initial resistance of all the samples. Indeed, it ‘only’ onset to 265 M Ω and it could be argued that it had not yet onset at all. But from Figure 6.3 it is obvious that at 270 seconds the current clearly changed to a higher value indicating an onset of some sort.

The high resistance had also some evident influence on the $I(V)$ of this sample. Whereas all the other samples (Table 6.2) showed linear $I(V)$ characteristics (after the maximum voltage was reached), sample Ag2 did not. Instead, the $I(V)$ is non-linear for all of the voltage ramps up to 10 V (Figure 6.5). For the discussion on the causes of the non-linearity in sample Ag2 see Section 6.6.

6.2.4 Conclusion

In conclusion, the onset time and onset resistance of percolating bismuth cluster films were not found to depend on the contact electrode material. A barrier that is expected to exist for bismuth-gold contacts due to the band banding at the interface should mean that gold contacted cluster films should exhibit a much higher resistance. The resistances reported here (Table 6.2) indicate that the

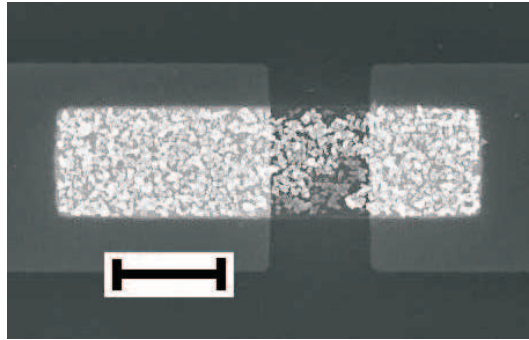


Figure 6.6: FE-SEM image of a bismuth cluster filled slot sample. This is slots#18 in Table 6.3. The scalebar is $1\mu\text{m}$.

expected barrier for the gold contacts either does not exist or that it does not influence the conduction.

This could be due to the fact that bismuth not only has electrons as carriers but has an equal number of holes. The expected barrier at the bismuth-gold interface however only exists for electrons; holes on the other hand can move freely across the bismuth-gold contact (Section 1.8.2). Holes, even though slower in mobility ($\mu_h \simeq 0.1\mu_e$ [Pratin et al., 1988]), also take part in the conduction. The reduction in the hole mobility should still effect the observed resistances by one order of magnitude assuming equal thickness of the film. However, looking at the difference in thicknesses (Table 6.1) it can be seen that they already deviate by 16% from each other and equal thickness can not be guaranteed for the samples investigated. Further, it was shown that high initial resistances can be reduced by applying a high voltage to the cluster film and annealing bottlenecks of conduction.

6.3 Cluster Filled Slots

Once a test percolating film sample had onset, bismuth cluster deposition was done on nanoscale slot samples. The sample layout proposed (Section 1.7.2) however, needs a few more changes (as mentioned in Section 6.1). The following section describes the cluster experiments to investigate FCFs and how the designs have changed throughout the investigation.

6.3.1 Bismuth Cluster Filled Slots

Bismuth cluster assembled devices were the main focus of this research. Table 6.3 lists the bismuth slot samples that will be discussed in this section.

The layout of the samples used in Table 6.3 has two slots per sample (Section 4.3), which meant that two large scale contact pads are used to connect to one small scale contact. During deposition both slots were monitored simulta-

Sample	Slot Width W	Contact Separation s	Cluster Film Thickness	Notes
First batch. Bi-layer PMMA.				
slots#A	3 μm	250 nm	8 nm	4.7 kOhm; lin
slots#B	3 μm	250 nm	26 nm	no onset
slots#C	1 μm	250 nm	15 nm	40MOhm; died
slots#D	3 μm	250 nm	32 nm	no onset
slots#E	1 μm	250 nm	NA	leaky
Second batch. Bi-layer PMMA.				
slots#1	3 μm	\sim 250 nm	57 nm	no onset
slots#2	3 μm	\sim 250 nm	39 nm	no onset
slots#3	3 μm	\sim 250 nm	49 nm	no onset
slots#4	3 μm	\sim 250 nm	80 nm	no onset; w/o V
slots#5	3 μm	\sim 250 nm	NA	test sample
Third batch. Single layer PMMA.				
slots#6	3 μm	\sim 250 nm	82 nm	no onset
slots#7	3 μm	\sim 250 nm	73 nm	onset? nlin
slots#8	3 μm	\sim 250 nm	NA	test sample
slots#9	3 μm	\sim 250 nm	61 nm	no onset
Fourth batch. Single layer PMMA.				
slots#10	3 μm	1 μm	85 nm	no onset
slots#11	3 μm	1 μm	95 nm	no onset
slots#12	3 μm	1 μm	125 nm	no onset
slots#13	3 μm	1 μm	85 nm	large L ; no onset
slots#14	3 μm	1 μm	85 nm	large L ; no onset; nlin
slots#15	3 μm	1 μm	85 nm	large L ; no onset;
slots#16	3 μm	1 μm	27 nm	large L ; 40k Ω /10k Ω
Fifth batch. Improved interface of contacts.				
slots#17	1 μm	1 μm	26 nm	90kOhm; lin
slots#18	1 μm	1 μm	21 nm	115MOhm; nlin
slots#19	1 μm	1 μm	20 nm	2.2GOhm; nlin
slots#20	1 μm	1 μm	24 nm	44MOhm; nlin
slots#21	1 μm	1 μm	19 nm	35MOhm; died
Sixth batch.				
slots#26	250 nm	1 μm	96 nm	no onset; nlin
slots#27	500 nm	250 nm	34 nm	onset
slots#28	500 nm	1 μm ; 500 nm	64 nm	onset
slots#29	500 nm	1 μm ; 500 nm	32 nm	onset

Table 6.3: List of the bismuth slot samples.

neously. Having no onset meant that neither of the two slots onset. Figure 6.6 shows an FE-SEM image of an actual bismuth cluster slot sample. Clearly it can be seen that the bismuth clusters form a film connecting the two electrodes. The following explains the reasoning behind the additional changes in layout made for those samples.

The first batch of samples shown here (Table 6.3) had a contact separation s of about 250 nm. W was 1 μm or 3 μm respectively for both slots on the sample. For the passivation layer itself a bi-layer PMMA was used. This is due to the fact that it originally was assumed that the cluster coverage on top of the PMMA would be the same as within the slot (Section 1.7.2). Since a bi-layer is about 200 nm high this would ensure that there is no cross connection between the clusters in the opening and the clusters on top of the PMMA. Later it was found that clusters adhere differently to different surfaces (Chapter 5) and only a single layer of PMMA was used from there on. Of the four testable samples in the first batch of samples (Table 6.3) two onset, i.e. showed a measurable current increase in a fixed time.

A second batch of bi-layer samples was prepared similar to the first, but the two slots on each sample having only slot widths W of 3 μm . Of all those samples none onset. Sample slots#4 was deposited onto without having a voltage applied, to see if the applied voltage itself prevents an onset to happen (the voltage applied could destroy newly created current paths). After the time which is needed for a percolating film sample to onset, sample slots#4 was moved out of the beam and checked for conduction. There was no measurable conduction even after sample slots#4 was deposited onto for twice as long as a percolating film sample. One of the samples (slots#5) was exposed to an atomic metal evaporation (just like the metallisation used to form the contacts). With a metal filling the opening, the sample was found to conduct thereby showing that the sample was prepared properly.

In the third batch the switch to single layer PMMA was done since the bi-layer was no longer needed due to the lack of clusters on top of the PMMA (Chapter 5). However, still no conclusive onset could be observed. The sample slots#7 showed a non-linear $I(V)$ characteristic after the deposition even though no onset was observed. Similar to the second batch, one sample was exposed to an atomic deposition filling the opening with metal. This sample was conducting, which means that the single layer process was also successful.

The next step (fourth batch in Table 6.3) was to change the separation width s of the contacts to 1 μm making them more similar to the percolating film samples (Figure 6.2), which always onset. Sample slots#13 had an opening with increased length L . Increasing L means that the overlap of the cluster ensemble with the electrode material is much greater. Having a greater contact area could improve the connection to the cluster ensemble. This is different from the initial idea (Section 1.7.2) where the cluster were thought to make contact to the electrodes

at the tip of the electrodes. Again, one of the samples (slots#14) had a non-linear $I(V)$ characteristic (post-deposition) even though no onset was observed. Only slots#16 in this batch showed an onset of conduction.

For the fifth batch, still keeping the separation s the same, the contact interface was improved by using a process to remove PMMA more efficiently. The contact interface is the area where the cluster ensemble contacts the electrode material. As was noted in Section 5.2 even correctly exposed and developed PMMA leaves PMMA residue behind [Maximov et al., 2002]. Therefore a very high exposure of $200 \mu\text{C}/\text{cm}^2$ was used to make the slot openings. Previously, an exposure of $80 \mu\text{C}/\text{cm}^2$ was used, which can leave PMMA residue behind (Section 5.2). An exposure of $140 \mu\text{C}/\text{cm}^2$ was shown to leave a clean smooth surface with a rms roughness of about 2 nm. The slot size W was $1 \mu\text{m}$. All the samples in this batch showed an onset.

For all the samples (Table 6.3), the large scale contact pads are about 50 nm high (Section 4.2) and can have rough edges. The small scale contacts are only 15 nm high (Section 4.2). Having rough and high edges on the large scale contacts could prevent a good interface between the small scale contacts and the large scale contacts. For the formation of the large scale pads of samples slots#18 to slots#21, a shadow mask was used as described in Section 4.3.3. This creates a slope on the large scale contacts. Having a sloped large scale contact means that the subsequent deposited small scale contact forms a good connection. In addition, a high exposure was used prior to forming the small scale contacts. The large scale layout used for samples slots#18 to slots#21 was the same as for the percolating film samples (Figure 6.2), which meant only one slot device could be placed on each sample.

All the samples of the fifth batch had measurable onsets. From Table 6.3 it can be seen that the onset thickness (as measured at the FTM) was about 20 nm to 24 nm. This is about 12% to 35% more than the thickness registered for the onset of percolating film samples (Table 6.1). For 30 nm bismuth clusters this corresponds to a coverage of about 60% to 80%. The post-deposition $I(V)$ curves were non-linear except for sample slots#17 which had clusters forming the small scale contact pads, i.e. the small scale contacts were not metal electrodes but clusters deposited at the same time as the clusters filling the opening. Sample slots#17 is similar to the cluster contact four point samples (Section 6.4) and will not be separately discussed here. Figure 6.6 shows an FE-SEM image of the cluster filled slot for the sample slots#18.

For the last bismuth batch the slot width W and separation width s was decreased, but still keeping a high exposure of to form the openings and small scale contacts. Instead of forming the large scale contacts by shadow evaporation (as was the case for the fifth batch) they were formed by optical lithography (Section 4.2). For the optical lithography and subsequent metallisation care was taken that no rough edges of the large scale contacts were formed. The samples

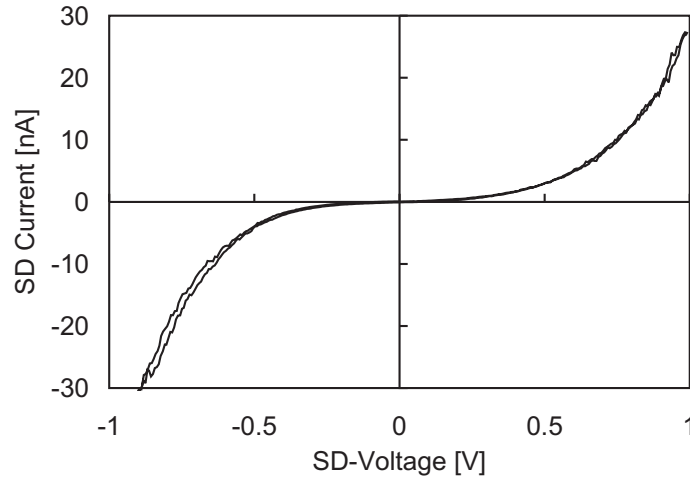


Figure 6.7: $I(V)$ for slots#7. Note, this sample did not show an onset, but still a post-deposition non-linear $I(V)$ was observed.

slots#26 to slot#29 had two slots per sample. For the last two samples the contact separation s of the two slots on the sample is different ($1\ \mu\text{m}$ and $500\ \text{nm}$ respectively). Except for sample slots#26 all samples showed an onset.

I(V)

Figure 6.7 shows the $I(V)$ characteristic of sample slots#7 in Table 6.3. Although many samples did not show an onset, a post-deposition $I(V)$ was always performed. For sample slots#7 a non-linear $I(V)$ was noted. In Figure 6.7 the zero bias conductance is very low. This explains why no onset could be seen since while depositing only a small voltage of about $50\ \text{mV}$ was applied. At that voltage the current flowing through the cluster network was only $100\ \text{pA}$. Small currents like that are detectable using the Keithley 6514 electrometer. However, during the deposition no sharp step in the current was observed. Previously, a sharp increase in current marked the onset of conduction and therefore the completion of a current path in percolating film samples.

The $I(V)$ characteristic of a slot sample that onset can be seen in Figure 6.8. Compared to the $I(V)$ in Figure 6.7 the zero bias conductance for sample slots#18 is much higher. This is understandable since this sample showed an onset of conduction during deposition. At a voltage of $50\ \text{mV}$ the current through this sample was $370\ \text{pA}$ more than three times the current registered for sample slots#7. In addition, at a voltage of $0.5\ \text{V}$ sample slots#18 showed a current of about $10\ \text{nA}$ whereas sample slots#7 only showed a lower current of about $4\ \text{nA}$. As will be discussed shortly (Section 6.5.4), $I(V)$ sweeps for samples which onset were not taken for too high voltages because the current flow could destroy the cluster device.

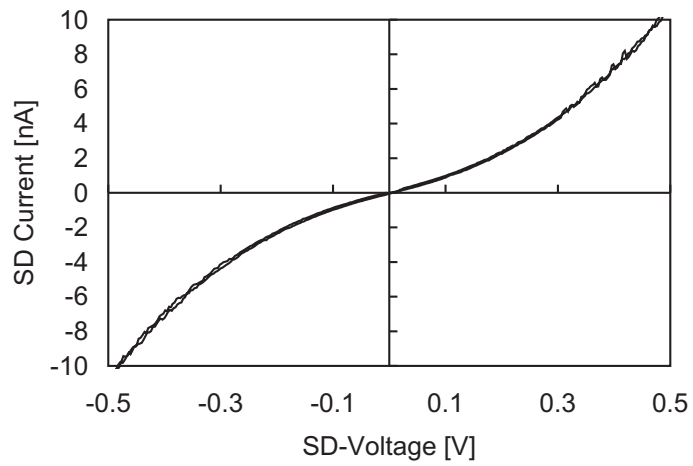


Figure 6.8: $I(V)$ for slots#18. This is the sample seen in Figure 6.6.

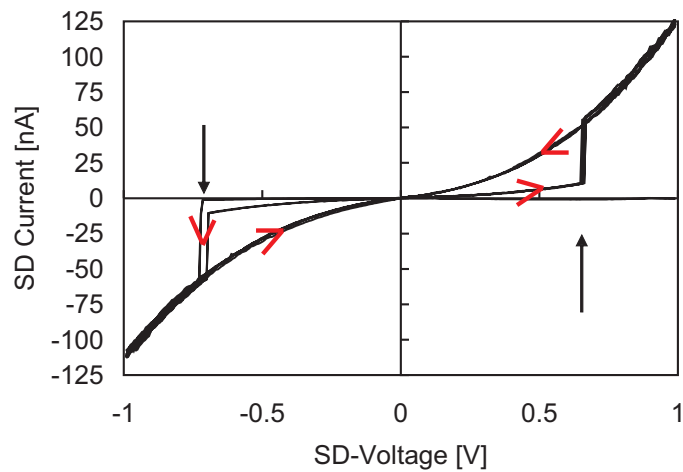


Figure 6.9: $I(V)$ for slots#26. Black arrows mark switching voltage and red arrows mark the direction of the sweep.

Like sample slots#7, sample slots#26 also did not show an onset and a subsequent post-deposition $I(V)$ was non-linear (Figure 6.9). In addition, it was noticed that the conductance through this wire could be switched on while ramping the voltage. At a voltage of about 0.75 V a step in the $I(V)$ can be seen. Below a voltage of 0.75 V two distinctive curves, a high conductance and a low conductance curve exist. The $I(V)$ for sample slots#26 in Figure 6.9 was swept several times continuously. Starting at $V = 0$ the voltage was increased and the current followed the low conductance path until a voltage of about 0.75 V was reached where the high conductance path is preferred. Sweeping backwards, the high conductance path remained even when the voltage is lowered past 0.75 V. Passing through $V = 0$ and going to negative voltages, the low conductance path is preferred until the voltage is high enough to switch to the high conductance path. Sweeping backwards after the maximum sweep voltage was reached, the current follows the high conductance path. This cycle repeats for the subsequent $I(V)$ sweeps. The low conductance only occurs for low voltages and the high conductance can only be accessed when a switching voltage is surpassed. At a voltage of 50 mV a current of 1 nA was registered for the high conductance and currents between 25 pA and 350 pA were measured for the low conductance curve. Unlike sample slots#26, sample slots#7 (Figure 6.7) remained in a low conduction state.

The case shown here (Figure 6.9) is a case of reversible switching. The case of irreversible switching was observed as well and will be described later (see Figure 6.20).

Gate Measurements

The idea of measuring FCFs using bismuth cluster assembled devices relied on the fact that by applying a gate voltage to such a device, the Fermi level in the bismuth could be altered so that FCFs can be observed. However, for the samples investigated during this thesis no response was observed that could be related to the changing of the applied gate voltage. Sometimes when the gate voltage was ramped a small increase in source drain conductance could be observed. Ramping the gate voltage in the opposite direction, the conductance was decreased by the same amount. This effect is due to a capacitive coupling of the substrate and the cluster assembled device.

Conclusion

Concluding the investigation for the bismuth slot samples, compared to percolating film samples an onset was difficult to observe. Only the latest batches of bismuth cluster filled slot samples showed an onset of conduction. However, observing no onset of conduction did not necessarily mean that no $I(V)$ could be taken.

Sample	Slot Width	Separation	Thickness	Notes
Antimony depositions.				
slots#22	1 μm	1 μm	44 nm	onset; nlin
slots#23	1 μm	1 μm	35 nm	500M Ω m; nlin
slots#24	250 nm	1 μm	80 nm	no onset
slots#25	250 nm	1 μm	80 nm	no onset

Table 6.4: List of the antimony slot samples.

Interestingly, of all the samples in Table 6.3 where $I(V)$ could be measured only two showed a linear $I(V)$ characteristic. Most of the observed $I(V)$ for the bismuth cluster filled slot samples were found to be non-linear. The two samples having a linear $I(V)$ were low resistance samples, whereas all non-linear $I(V)$ were observed for high resistance ($> \text{M}\Omega$) samples.

In the percolating film samples used to test the cluster source condition (Figure 6.2) clusters make contact to metal electrodes as well and conduct. The difference to the slot samples is that the overlap between the cluster ensemble and the contact, i.e. the area of contact, is very large for the percolating film samples and very small for nanoscale samples.

It could be argued that the non-linear $I(V)$ are due to PMMA residue, but samples that showed an onset exhibited non-linear $I(V)$ as well. The non-linearity of the $I(V)$ characteristics is further discussed in Section 6.6.

In summary, the formation of bismuth cluster filled slot samples was shown. The $I(V)$ of high resistance slot samples were found to be non-linear. Observing no onset of conduction does not necessarily mean that no cluster connection was formed nor that a $I(V)$ characteristic can be measured.

6.3.2 Antimony Cluster Filled Slots

The main focus of this research was the investigation of bismuth cluster assembled nanoscale devices. Antimony clusters exhibit similar interesting properties and were studied in our group intensively before [Kaufmann, 2006]. For comparison with bismuth filled slot samples, antimony samples were prepared. This is also due to the fact that the UHV cluster apparatus was used to extend previous studies of antimony clusters in the HV system [Partridge et al., 2004]. Table 6.4 lists the antimony cluster filled slot samples. For the testing of the antimony clusters the sample style was used which worked for bismuth successfully (batch 5 in Table 6.3). However, the results obtained are far different from the bismuth case. Even though two of the antimony sample onset, the onset time was nearly twice as long.

It was found that antimony clusters assemble differently compared to bismuth clusters. As was reported previously (Chapter 5) antimony clusters assemble via

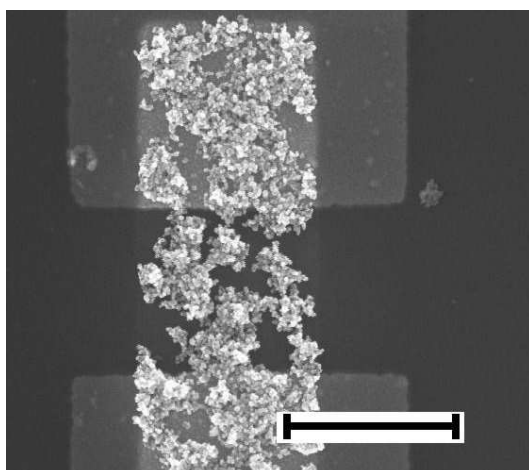


Figure 6.10: FE-SEM image of an antimony cluster filled slot sample. This is sample slots#22 in Table 6.4. The scale bar is 1 μm .

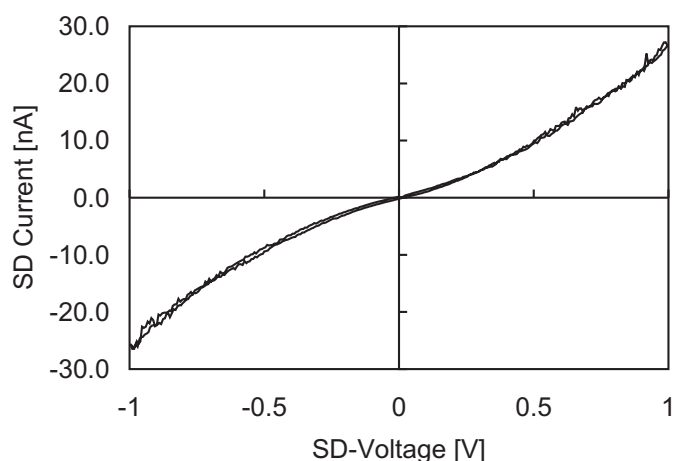


Figure 6.11: $I(V)$ for sample slots#22 in Table 6.4.

clumping and soft-landing on such sites as defects or other clusters. This type of assembly can be seen in Figure 6.10. Instead of filling the opening evenly, the clusters clump together.

This could also explain why no onset for slot#24 and slot#25 was observed. As can be seen from the deposited thickness of about 80 nm the time was nearly four times that of a successful onset of a bismuth device. Even though the assembly of antimony in PMMA slots is fascinating on its own, the focus of this work is on bismuth. Therefore no further investigation was done.

Figure 6.11 shows the $I(V)$ characteristic of an antimony cluster filled slot sample (sample slots#22 in Table 6.4). Similar to the bismuth cluster filled samples, the $I(V)$ is non-linear. Like the $I(V)$ shown for sample slots#18 (Figure 6.8) a positive slope at zero bias indicates that the sample onset.

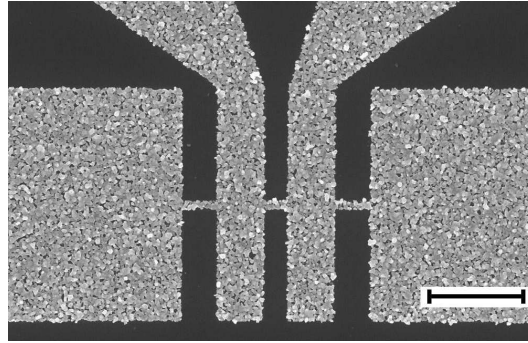


Figure 6.12: A cluster contact 4 point sample. This is sample 4pt#3 in Table 6.5. The scale bar is 2 μm .

6.4 Cluster Contact Four Point Samples

6.4.1 Why use Clusters as Contacts

Instead of using an evaporated metal to form the small scale contacts the samples presented in this section had clusters as their contact material. That means the cluster wire is connected to small scale contacts formed of clusters. This was used first for sample slots#17 in Table 6.3 with success and takes advantage of the adhesion properties of clusters (Chapter 5). For the samples discussed here, a four point layout was used (Section 4.3.2). The cluster wire and the small scale contacts were formed at the same time. This means that there are no contact potentials between the cluster wire and the cluster contacts. Compared to previous samples the four point layout allows the measurement of the contact independent resistance of a cluster network, which has not been done yet.

Figure 6.12 shows the layout of the cluster contact four point samples. Four electrodes connect to the cluster wire. The distance between the two outermost electrodes is about 4 μm . Each of the innermost electrodes is about 1 μm wide and the distance between the innermost electrodes is about 0.5 μm . The cluster wire connecting all four electrodes is about 0.2 μm wide.

6.4.2 Preparation

The cluster contact four point samples were deposited with bismuth clusters produced in the IGA, using a flow rate of 100 sccm argon and a crucible temperature between 775 $^{\circ}\text{C}$ and 785 $^{\circ}\text{C}$. The source pressure was 23 Torr. Further deposition details can be found in Table 6.5.

For a four point sample it is essential that all four electrodes are connected to the cluster wire. Therefore, during deposition the current through the cluster wire was monitored between the outermost electrodes and once an onset was achieved the deposition was stopped. Compared to the previously mentioned percolating film samples (Table 6.1) it took longer to achieve an onset. This can be easily

Sample	Deposition rate [Å/sec]	Time to onset [sec]	Thickness [nm]
4pt#1	0.70	640	45
4pt#2	0.75	610	46
4pt#3	0.75	400 (inner) 700 (outer)	52

Table 6.5: Deposition details 4pt cluster contact samples

Sample	2pt R outer [kΩ]	2pt R inner [kΩ]	4pt R inner [kΩ]
4pt#1	16	13	2.5
4pt#2	14	-	1.6
4pt#3	11	-	1.5

Table 6.6: Resistances of previously mentioned (Table 6.5) 4pt cluster samples. Outer refers to the two outer-most contacts in Figure 6.12 and inner are the two middle contacts.

understood since the crucial connection is obviously the cluster wire between the contacts which has a finite size (fixed width). In order to form a connection between the electrodes the clusters have to fill the opening over the whole length of the wire.

With sample 4pt#3 not only the outermost electrodes were monitored, but the innermost electrodes as well. The innermost electrodes were connected to a DC voltmeter. Once a connection was achieved the potential difference shown by the voltmeter was zero. Without a connection this potential was just floating. Using this method, it can be seen (Table 6.5) that the innermost electrodes were connected long before a current carrying wire over the whole length was formed. Having random cluster deposition it is easy to understand, that the shorter connection will have a faster onset than the long but equally wide connection.

6.4.3 Four Point Measurements

A four point measurement is a resistance (conductance) measurement which eliminates the effect of the contacts (contact potentials/contact resistances). Here, a voltage is applied between the outermost electrodes causing a flow of current; the innermost electrodes are used to measure the potential difference (only between the innermost electrodes) due to the current flow.

Table 6.6 lists the two point and four point resistances of the samples respectively. As can be seen the two point resistances for the outermost electrodes were between 11 kΩ and 16 kΩ. Compared to the bismuth cluster filled slots (Section 6.3) the two point resistances of the cluster contact four point samples are much lower.

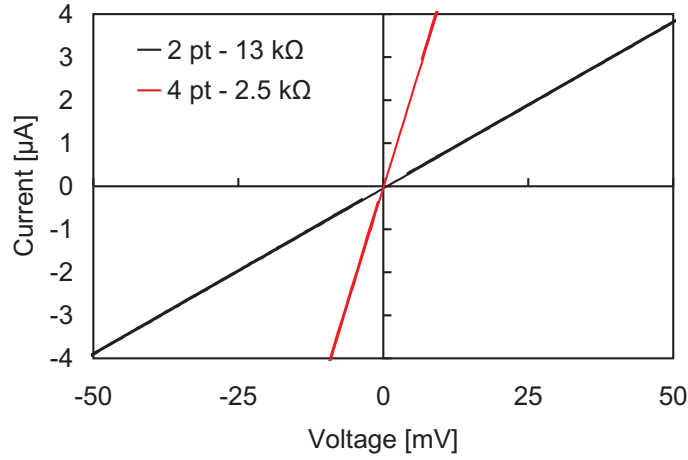


Figure 6.13: $I(V)$ characteristic for sample 4pt#1 (see Table 6.5). The two lines are the 2 point resistance (black) and 4 point resistance (red) respectively between the innermost electrodes.

Figure 6.13 shows the $I(V)$ characteristic for sample 4pt#1 between the innermost electrodes. As can be seen, both the two-point and the four-point $I(V)$ are linear. The four point resistance is only 2.5 kΩ compared to 13 kΩ for the two point resistance of the same sample. By taking into account the dimensions of the cluster wire, this relates to a resistivity of about $45 \times 10^{-6} \Omega\text{m}$ which is about 40 times the bulk resistivity of bismuth ($1.07 \times 10^{-6} \Omega\text{m}$ [Stöcker, 1994]). This means that even without taking into account the contact resistance, the bismuth cluster wire still has a higher resistivity. However, this is not surprising, because the cluster wire is far from an ideal wire. It is comprised of clusters, i.e. boundaries are present along the length of the wire. Scattering of carriers at the boundaries increases the resistivity. In addition, the packing of the cluster within the opening is not ideal either, i.e. there are holes and gaps in the cluster wire making it porous.

Bismuth clusters (and antimony clusters) are found not to adhere to the PMMA passivation layer (Chapter 5). Using this template method, it was possible to create a pattern in PMMA which allowed a four point measurement on a bismuth cluster assembled wire. The resistivity of a bismuth cluster wire was found to be 40 times higher than the bulk resistivity of bismuth. Similar to percolating film samples (Section 6.2) for a two point measurement the $I(V)$ are linear. Four point measurement $I(V)$ s are linear as well.

6.4.4 $R(T)$ Measurements

Using a four point cluster contact sample, the temperature dependent four point resistance of a bismuth cluster wire was measured. The temperature dependent

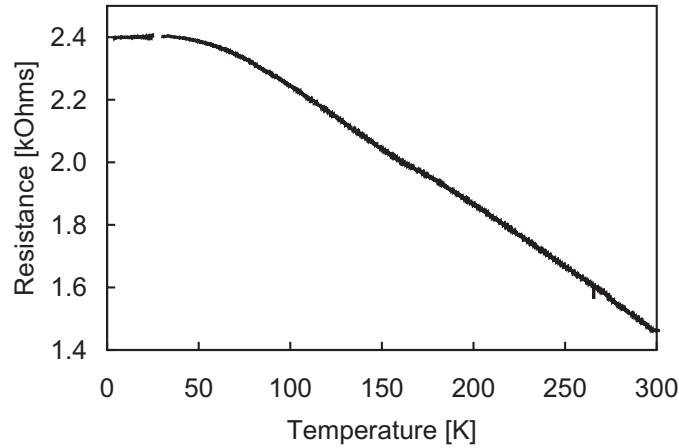


Figure 6.14: Temperature dependent four point resistance for a cluster contact four point sample. This is sample 4pt#3 in Table 6.5.

resistance of bismuth cluster assembled percolating films was previously studied at our group at the University of Canterbury [Schulze et al., 2003]. Similar to those findings on percolating films, the resistance of cluster assembled nanoscale devices was found to increase with decreasing temperature.

Figure 6.14 shows the temperature dependent four point resistance of a bismuth cluster wire. This is different to the previous results since a four point measurement excludes contact resistances. Still, the four point resistance of bismuth clusters is increasing with decreasing temperature showing a negative temperature coefficient of resistance (TCR).

The temperature dependance of the resistivity is given as

$$\sigma(T) = \frac{1}{\rho(T)} = \mu(T)n(T), \quad (6.1)$$

with $\mu(T)$ denoting the temperature dependence of the carrier mobility and $n(T)$ denotes the temperature dependence of the carrier concentration.

To be able to observe a negative TCR, either the scattering has to increase or the carrier density has to decrease as the temperature is reduced. The mobility $\mu(T)$ in bulk bismuth decreases by 3.5 orders of magnitude as the temperature increases over the range 5 K to 300 K [Heremans et al., 2000]. The carrier concentration in bismuth decreases by an order of magnitude when cooling it down from 300 K to 4.2 K [Zhang et al., 2000]. Combining the two facts, for bulk bismuth, the resistivity decreases as the temperature decreases. In the case of bismuth cluster assembled wires however, the resistivity increases with decreasing temperature (Figure 6.14).

The mobility is mainly caused by two scattering mechanisms. Electron phonon scattering which decreases with decreasing temperature, since the phonon density

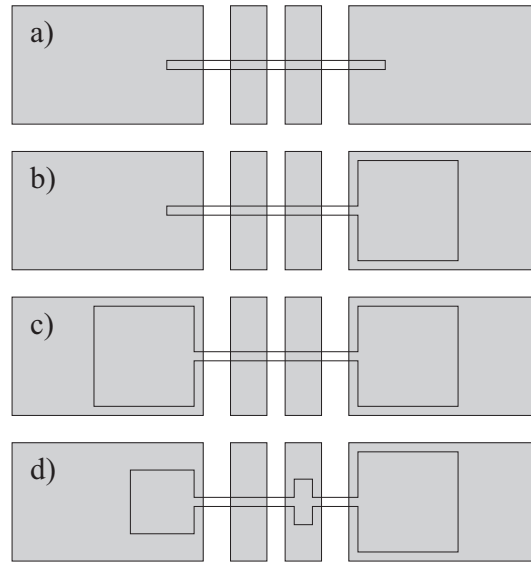


Figure 6.15: Schematic layout of the four point samples. a) opening connecting all four electrodes, b) same as a) and the overlap area on one outer electrode is increased, c) same as a) and the overlap area on both outer electrode is increased, d) opening connecting all four electrodes, the overlap area on all electrodes is different.

decreases with decreasing temperature and can not result in a negative TCR. Secondly, there is scattering at boundaries, which is the main scattering mechanism in cluster assembled wires. For bismuth the mean free path of electrons is already 250 nm at room temperature [Smith et al., 1964]. Therefore boundary scattering is already dominant at room temperature for bismuth clusters which are only 30 nm to 40 nm in size. This means that boundary scattering is independent of the temperature and can not explain a negative TCR.

The decrease of the carrier concentration with decreasing temperature in bismuth is independent whether bulk bismuth or bismuth clusters are involved. That means the temperature dependence of bismuth assembled cluster wires can be explained by the decrease of the carrier concentration in bismuth for decreasing temperature.

6.5 Four Point Samples with Metal Contacts

Four point samples with metal contacts are similar to the previously described slot samples (Section 6.3). However, instead of having only two contacts they have four contacts, which makes it possible to perform four point resistance (conductance) measurements to further investigate the non-linear $I(V)$ seen for the slot samples. Table 6.7 lists the various four point samples analysed. Three different cluster materials were investigated.

Figure 6.15 shows schematically an overview to the variations in contact area between the cluster ensemble and the contacts of the investigated four point

Sample	Material	Thickness	Notes
4pt#1	Bi	45 nm	
4pt#2	Bi	46 nm	
4pt#3	Bi	52 nm	
4pt#4	Bi	120 nm	only slots
4pt#5	Bi	85 nm	only slots
4pt#6	Bi	48 nm	only slots
4pt#7	Bi	74 nm	only slots
4pt#8	Bi	88 nm	only slot; no onset
4pt#9			test sample
4pt#10	Bi	82 nm	large foot one side; no onset
4pt#11	Bi	31 nm	large foot either side
4pt#12	Bi	62 nm	large foot either side
4pt#13	Bi	70 nm	varying foot all contacts
4pt#14	Pd	12 nm	large foot either side
4pt#15	Pd	10 nm	large foot either side
4pt#16	Pd	21 nm	large foot either side
4pt#17	Bi	96 nm	varying foots all contacts
4pt#18	Bi	35 nm	varying foots all contacts
4pt#19	Bi	25 nm	varying foots all contacts; high flow
4pt#20	Bi	32 nm	large foot either side; long pump
4pt#21	Bi	54 nm	large foot either side; long pump
4pt#22	Pd	7 nm	large foot either side; Bi-layer
4pt#23	Pd	8 nm	large foot either side; Bi-layer
4pt#24	Pd	8 nm	large foot either side; Bi-layer
4pt#25	Bi	68 nm	large foot either side; dI/dV
4pt#26	Bi	59 nm	large foot either side; dI/dV
4pt#27	Sb	24 nm	large foot either side
4pt#28	Sb	32 nm	large foot either side

Table 6.7: List of the cluster four point samples.

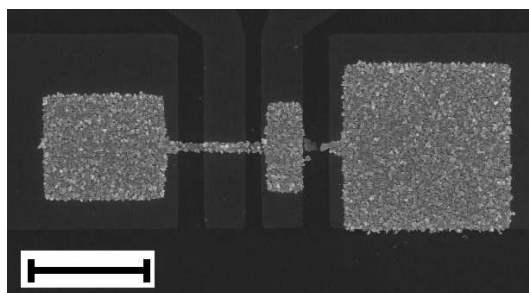


Figure 6.16: FE-SEM image showing sample 4pt#17. This sample has clusters deposited into an opening which has different area overlaps on all four electrodes. The scalebar is 3 μm .

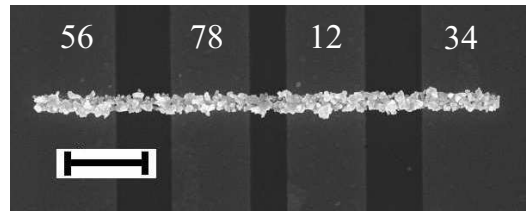


Figure 6.17: Labelling convention of the contacts on a four point sample. This is an FE-SEM image showing sample 4pt#7. The scalebar is $1 \mu\text{m}$.

cluster samples. The layout of the electrodes and the opening is the same as used for the cluster contact four point samples (Section 6.4). Figure 6.16 shows an FE-SEM image of a cluster wire on top of the four electrodes having varying areas of overlap on each contact. The innermost electrodes are about $1 \mu\text{m}$ wide, having a spacing of about $0.5 \mu\text{m}$. The distance between the two outermost electrodes is about $4 \mu\text{m}$ and the cluster wire connecting all four electrodes is about $0.2 \mu\text{m}$ wide.

Figure 6.17 shows the convention in labelling the contacts. Each four point sample has four contacts and each contact is connected to two contact pads. The contact pads here are denoted by a number from 1 to 8 and each electrode therefore is denoted by two numbers. Having four electrodes, it is possible to perform six independent two point resistance measurements. The possible combinations are noted by 34&56, 34&12, 34&78, 12&78, 12&56 and 78&56. See Figure 6.17 for the position of the respective contacts.

Using PMMA as a template, the opening connecting all four contacts can be easily changed. In Table 6.7, ‘Slot only’ refers to samples having a cluster wire of about 200 nm width connecting all four electrodes of the device layout (Figure 6.15a). This layout is the same as for the slot samples (Section 6.3) only that now two additional contacts are involved. The note ‘Large foot’ means that on top of the outer electrode(s) a larger area was exposed increasing the cluster wire-contact area for this particular electrode (Figure 6.15b and Figure 6.15c). ‘Varying foot’ then is only a variation of the overlapping area for all four electrodes (Figure 6.15d). The variation in contact area were done in order to see whether an increased contact area has an effect on the overall conduction (see Section 6.5.1).

Using the IGA source, the bismuth clusters were usually formed using an inert gas flow of 100 sccm argon. Changing the flow, changes the speed of the clusters. Sample 4pt#19 in Table 6.7 was formed using an inert gas flow of 200 sccm argon to investigate whether this effects the formation of the cluster wire, but no change was found. To reduce possible oxidation of the bismuth clusters, for samples 4pt#20 and 4pt#21 a much longer pre-pump cycle (one whole day) was used to lower the base pressure within the system. But still a non-linear $I(V)$ was observed.

Normally, the PMMA layer used to form the opening on top of the four electrodes was just a single layer of HMW PMMA. Samples 4pt#22, 4pt#23 and 4pt#24 had a bi-layer of PMMA which resulted in much deeper (also undercut) openings. Compared with the slot depth of a single layer of about 40 nm these were 5 times deeper (about 200 nm). Chapter 5 established that the bi-layer is no longer necessary for bismuth or antimony cluster assembled devices, but the assembly of palladium clusters is different. The reasoning to opt again for a bi-layer follows in Section 6.5.3, where the results of the electrical measurements of palladium clusters are shown.

In most cases the $I(V)$ characteristic does not give a conclusive picture of the conductance mechanism involved. Being able to access the differential conductance allows further analysis. For Ohmic devices the conductance is the current divided by the voltage ($G = I/V$) and is a fixed positive number which is a property of the device. Having non-linear $I(V)$ characteristics, more than one definition of conductance exists. For the conductance of that device at a certain voltage it can be defined as the current divided by the voltage. A differential conductance can be defined by $G_{diff} = dI/dV$ which can differ (for non-Ohmic devices) from the conductance defined previously. The differential conductance could even be negative; note that the actual conductance G of a device always remains positive.

Sample 4pt#25 and sample 4pt#26 were used to test a circuit for differential conductance measurements. Hereby, a slow voltage ramp to measure the $I(V)$ is superimposed with a fast small AC voltage to measure dI and dV . Due to the capacitive coupling of the conducting substrate however, the measured signal was dominated by the capacitance of the substrate and no direct measurement of the dI/dV was possible.

6.5.1 Bismuth Clusters

Samples 4pt#1, 4pt#2 and 4pt#3 are special bismuth four point samples and are discussed separately in Section 6.4. The bismuth clusters for the four point samples were prepared using the IGA with a 100 sccm flow of argon. During deposition the source pressure was 24 Torr and the crucible temperature was 800 °C. Sample 4pt#19 was formed using a flow of 200 sccm argon.

As mentioned previously, it was believed that the contact area for the overlap between the clusters and the contact electrode played a major role in the conduction through that contact. For sample 4pt#13, the maximum current for the maximum voltage of the voltage sweep was found to increase with the minimum contact area of the respective contacts. The minimum area is the smallest area of contact of the two contact electrodes involved. It is interesting to note that the current scales with the minimum contact area and not with the total area combined.

To investigate further, additional samples with varying contact areas were prepared (samples 4pt#17, 4pt#18 and 4pt#19). For these samples however the previous described increase of current with contact area was not seen.

Figures 6.18 and 6.19 show the two-point $I(V)$ for the innermost contacts (contacts 12&78) of samples 4pt#21 and 4pt#18 respectively. The $I(V)$ shown in Figure 6.20 is for contacts 34&56 of sample 4pt#4. The examples shown are typical examples of the non-linear $I(V)$ for bismuth cluster four point samples (Table 6.7).

As can be seen for the two point $I(V)$ the non-linearity becomes more dominant with maximum sweep voltage. Starting with a small maximum voltage of about 100 mV in Figure 6.18 the $I(V)$ is almost linear. For higher maximum sweep voltages the deviation from a linear $I(V)$ can be seen more clearly.

For sample 4pt#4, only after a certain forward voltage was surpassed (about 0.8 V) was the non-linear behaviour present. This shows a case of an irreversible switching behaviour contrary to the reversible switching shown for sample slots#26 (Figure 6.9).

However, four point measurements revealed a linear relationship as can be seen in Figure 6.21. The four point resistance for sample 4pt#18 is about 3.9 k Ω which relates to a resistivity of the cluster assembled wire to about $55 \times 10^{-6} \Omega\text{m}$ and is about 50 times more than the resistivity of bulk bismuth. This is quite comparable to the value for the resistivity measured previously (for samples 4pt#1) on a cluster contacted bismuth sample. The two point $I(V)$ for the same contacts can be seen in Figure 6.19.

Similar to the bismuth clusters in slot samples (Table 6.3) the two point resistances for four point cluster samples were high. A high contact resistance however can prevent any voltage being registered at the inner electrodes. Therefore a high voltage (current limited) was applied to the electrodes for a long time and it was possible to anneal the cluster wire and the contacts. The four point measurement in Figure 6.22 shows the result of such an anneal. This annealing can explain why the resistivity for sample 4pt#21 was only 10 times higher than the bulk resistivity of bismuth compared to the 50 times which was observed for the not annealed sample 4pt#18. However, as can be seen in Figure 6.18 the two point $I(V)$ for the inner pair of contacts is still non-linear.

6.5.2 Antimony Clusters

Antimony similar to bismuth is a semimetal. However, in the case of antimony the band overlap is larger. Previous electron diffraction experiments indicated that by varying the source conditions amorphous clusters, crystalline clusters and 'Sb4' assembled clusters can be formed [Kaufmann, 2006]. Furthermore, the size of antimony clusters can easily be adjusted by changing the flow of inert gas (Figure 3.4).

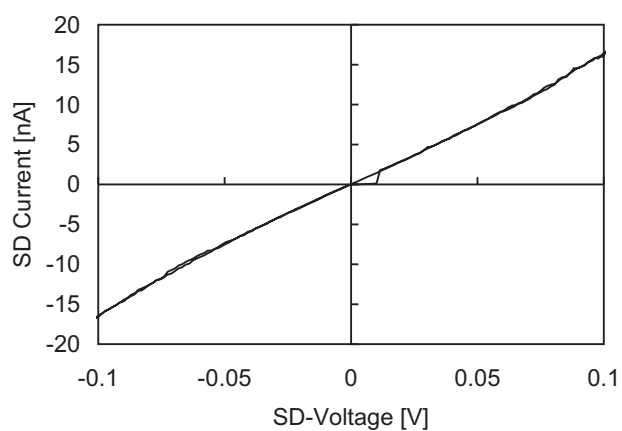


Figure 6.18: 2-point resistance measurement with non-linear $I(V)$ characteristic for a bismuth clusters sample (contacts 12&78 of sample 4pt#21 in Table 6.7).

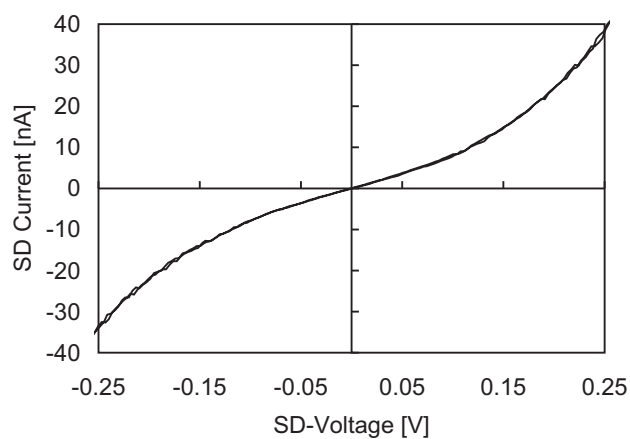


Figure 6.19: 2-point resistance measurement with non-linear $I(V)$ characteristic for a bismuth clusters sample (contacts 12&78 of sample 4pt#18 in Table 6.7).

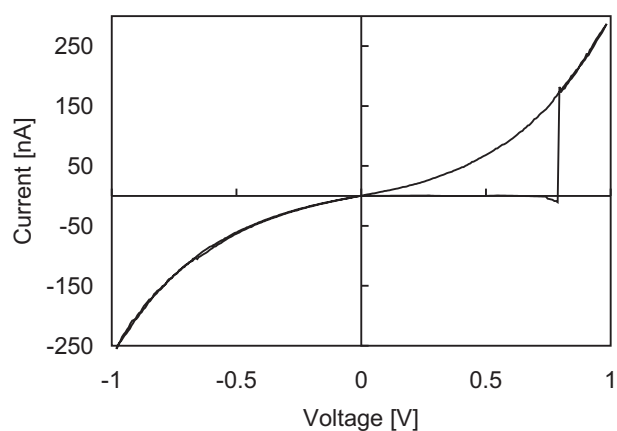


Figure 6.20: 2-point resistance measurement with non-linear $I(V)$ characteristic for a bismuth clusters sample (contacts 34&56 of sample 4pt#4 in Table 6.7).

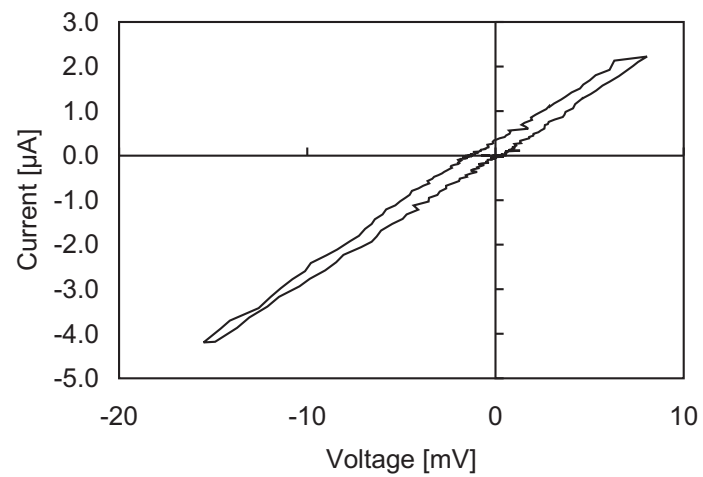


Figure 6.21: 4-point resistance measurement with linear $I(V)$ characteristic for the bismuth cluster sample 4pt#18 in Table 6.7.

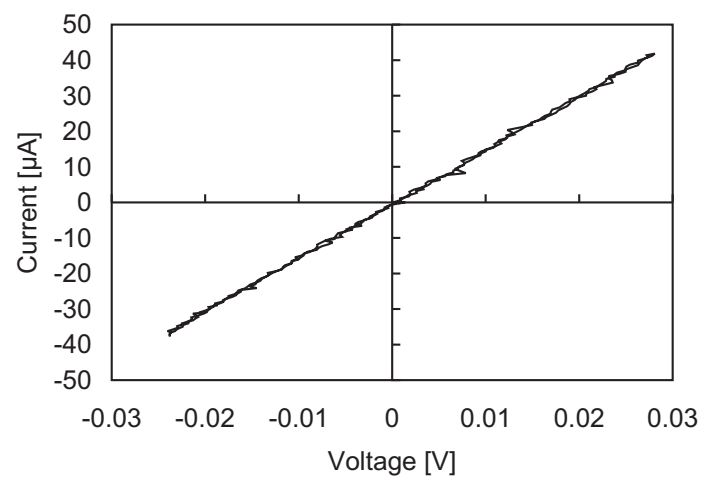


Figure 6.22: 4-point resistance measurement with linear $I(V)$ characteristic for the bismuth cluster sample 4pt#21 in Table 6.7.

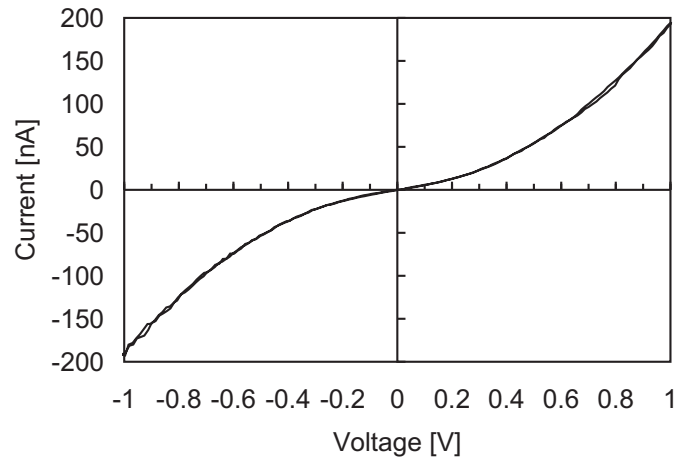


Figure 6.23: 2-point resistance measurement with non-linear current voltage characteristic for a antimony cluster sample (contacts 34&56 of sample 4pt#28 in Table 6.7).

The antimony clusters for samples 4pt#27 and 4pt#28 were produced using a mixture of 50 sccm argon and 50 sccm helium and the inert gas aggregation source. The source pressure was 8.4 Torr with a crucible temperature of 670 °C.

Figure 6.23 shows the two point $I(V)$ resistance of an antimony sample (sample 4pt#28 in Table 6.7). Again it can be seen that the $I(V)$ is non-linear. Unlike the bismuth cluster four point samples it was not possible to measure four point resistances for the antimony cluster samples. High contact resistances prevented any potential difference being registered at the inner electrodes.

6.5.3 Palladium Clusters

Unlike bismuth and antimony, which are semimetals, palladium is a metal. Using palladium clusters it is therefore possible to compare the previously observed conduction mechanism for the semimetals with the ‘simpler’ case of a ‘normal’ metal. Palladium clusters were produced using the magnetron sputter source (Section 3.4). A flow of 100 sccm argon and a sputtering power of 25 W yielded a deposition rate of about 0.08 Å/s.

In Table 6.7 there are two batches of palladium cluster samples. The first was prepared having a single layer of PMMA. Inspecting the samples 4pt#14, 4pt#15 and 4pt#16 with an FE-SEM after the deposition showed that the adhesion of the palladium clusters is independent on whether they hit the PMMA or the substrate within the opening. For the second batch of samples, therefore a bi-layer was used, which should prevent connection to the cluster film on top of the PMMA because of the increased depth of the opening. This was the original idea behind the passivation layer presented in Section 1.7.2.

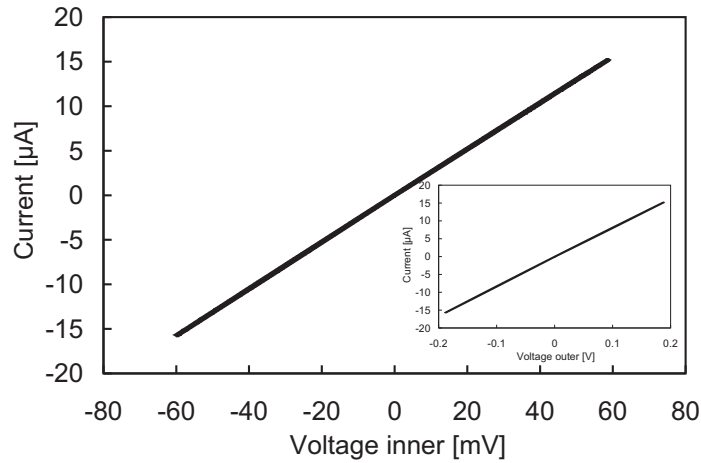


Figure 6.24: 4-point resistance measurement for a palladium cluster sample (sample 4pt#16 in Table 6.7) with linear $I(V)$ characteristic. Inset shows the 2-point resistance measurement of the outer contacts with linear $I(V)$ characteristic.

Figure 6.24 shows the $I(V)$ characteristic of the palladium sample 4pt#16. As can be seen the $I(V)$ is linear indicating Ohmic conduction within the cluster wire. The four point resistance is $4\text{ k}\Omega$. The inset shows the two point resistance measurement between the outermost contacts of the four point sample arrangement, which is also linear.

A different picture however, can be seen in Figure 6.25 for sample 4pt#15. Here, the $I(V)$ characteristic revealed a slightly non-linear behaviour for both the two point measurement and the four point measurement. For the discussion on the origin of the non-linear $I(V)$ for sample 4pt#15 see Section 6.6.

The two samples shown both had only a single layer of PMMA as a passivation layer. There is the possibility that the conduction might have been through the whole film on top of the PMMA as well. For the bi-layer samples (samples 4pt#22, 4pt#23 and 4pt#24) a slower onset was observed compared to the single layer samples. In addition, once a connection was formed, the resistance kept decreasing even though the deposition had stopped. This could mean that the current flow through the wire was constantly annealing it. It also prevented a $I(V)$ characteristic being taken since the current kept changing even with no voltage ramp applied.

In summary, the investigations using palladium clusters have shown metallic conduction between the electrodes of four point samples. The two point resistance measurements were linear (apart from sample 4pt#15, which will be separately discussed in Section 6.6). Palladium cluster four point samples have shown that the samples used had clean contacts, i.e. no oxide or residue causing unusual high contact resistances.

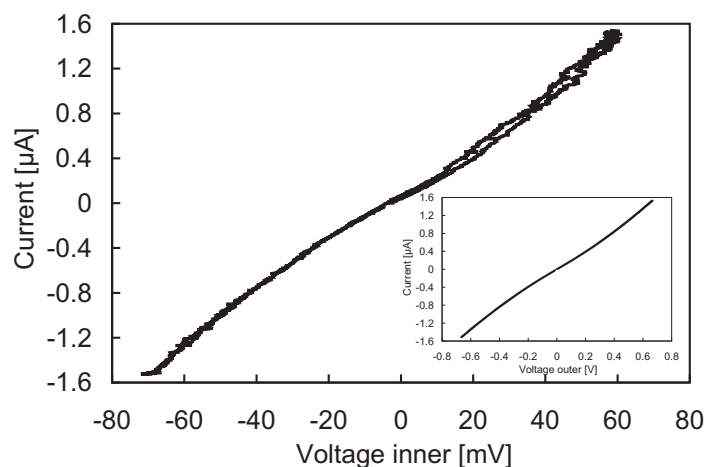


Figure 6.25: 4-point resistance measurement for a palladium cluster sample (sample 4pt#15 in Table 6.7) with non-linear $I(V)$ characteristic. Inset shows the 2-point resistance measurement of the outer contacts with non-linear $I(V)$ characteristic.

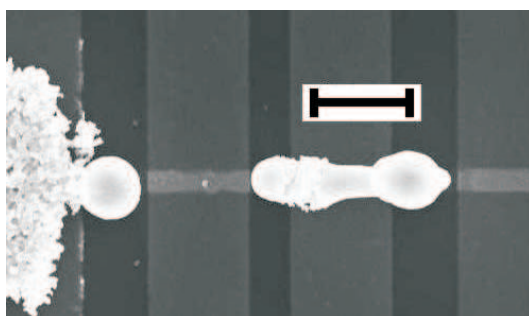


Figure 6.26: Annealing with fixed voltage. The scalebar is $1\mu\text{m}$. This is sample 4pt#10 in Table 6.7.

6.5.4 Annealing

The initial resistances of nanoscale cluster samples like the slot samples (Table 6.3) and four point samples (Table 6.7) were usually very high. It was investigated whether that high resistance could be lowered by annealing. However, the annealing attempts using fixed voltage were fatal to the samples.

Figure 6.26 shows the result of a voltage anneal attempt for a bismuth cluster four point sample (sample 4pt#10). When annealing, a fixed high voltage was applied to the outer electrodes. The voltage causes a current to flow through the cluster wire. Due to the high resistance at bottlenecks this current causes local heating and thereby annealing of the wire. Once the wire is annealed the current path becomes less resistive. That means that for the same applied fixed voltage now even more current can pass through. This heats the cluster ensemble even further and subsequently lowers the resistance further. The time scale involved for this to happen is very short (less than a second).

Sample	Nanoscale Device	V-groove	Percolation	Interdigitated Fingers
# of Clusters	~100	~1000	very large	very large
Contact Area	small	large	very large	large
Contact Separation	small	medium	large	small
Current Paths	~1	1-10	$\gg 1000$	$\gg 1000$

Table 6.8: Comparison of sample layouts used previous and during this thesis.

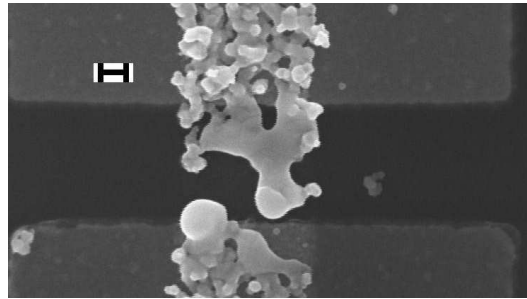


Figure 6.27: Accidentally ‘annealed’ nanoscale cluster device. The scalebar is 100 nm. The sample shown is slot#28 in Table 6.3.

Bismuth has a low melting point [Stöcker, 1994] and eventually enough current is flowing that the current heating causes the cluster ensemble to melt. The melt then beads, breaking the connection and rendering the device useless as can be seen in Figure 6.26. This behaviour is different to the observed lowering of resistance in percolating film samples (Section 6.2), but can be explained by comparing the different sample layouts. Table 6.8 shows that the nanoscale devices have a small number of clusters and in addition, usually only show one current path. That means the heat (and the current) required to melt the whole ensemble is much lower for the nanoscale cluster devices. Such a destructive scenario could happen for a current path in percolating cluster films, too, but there, more than one current path exists. So even if one is destroyed, the others are still able to carry the current. The quantity changing the resistance is not the applied fixed voltage but the current and the subsequent current heating at bottlenecks.

Indeed, the nanoscale cluster devices are so delicate that even connecting and disconnecting leads to the sample could destroy the existing current path. Complete care had to be taken that the cluster wires were shorted whenever equipment around the cluster apparatus was turned on or off. Figure 6.27 shows the result of an accidentally damaged sample.

The result was that careful considerations had to be made when measuring a $I(V)$ characteristic. If a too high maximum voltage is set on the ramp box, the device could be destroyed. Usually, several $I(V)$ sweeps were taken, beginning with a low maximum voltage and increasing it in steps until a too high current was observed.

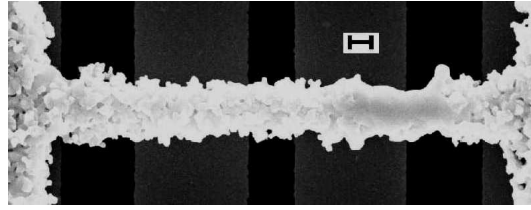


Figure 6.28: Annealing with fixed current. The scalebar is 200nm.

It would be of advantage to apply a current instead of a voltage. However, for the electrical measurements only a voltage supply was available and a different solution sought. In order to limit the maximum current that can pass through the clusters, a high resistance resistor was placed in series with the cluster wire. The resistance was usually chosen to be in the same order as the resistance of the cluster wire. Now a voltage was applied to both the resistor and the sample. As explained previously, current heating anneals bottlenecks along the current path and reduces the resistance of the cluster wire. The resistor in series now prevents the spiralling cycle to destruction by limiting the maximum current available to pass through both the resistor and the cluster ensemble. Figure 6.28 shows the result of a current limited voltage anneal. Clearly it can be seen that the cluster ensemble melted between the two right electrodes, annealing the wire.

6.5.5 Conclusion

Clusters were assembled on top of four electrodes which allowed four point measurements of cluster wires. Three different materials of clusters were used. The bismuth and antimony cluster assembled wires show non-linear two point $I(V)$. Four point measurements show for bismuth a linear $I(V)$.

The resistivity for a bismuth cluster wire determined by a four point resistance measurement was 50 times higher than the resistivity of bulk bismuth. This compares very well with the previously observed measurement for the cluster contacted bismuth wire (Section 6.4), which was 40 times higher than the resistivity of bulk bismuth.

It was shown that the cluster wire resistance can be decreased by current limited annealing. Applying a high voltage, as was the case for the percolating film samples (Section 6.2) proved fatal for the nanoscale cluster devices. Annealed bismuth cluster wire had a resistivity (by four point measurement) which was only 10 times the bulk resistivity of bismuth (Figure 6.22).

6.6 Non-Linear $I(V)$ vs Linear $I(V)$

From the nanoscale cluster samples (Section 6.3 and Section 6.5) it was noticed that the samples have shown both linear or Ohmic behaviour as well as non-linear

behaviour. A very large number of cluster assembled devices showed non-linear $I(V)$ characteristics. In one case or the other a non-linearity was seen for all sample styles and all investigated cluster materials.

6.6.1 Causes of Non-Linear Effects

Non-linear current-voltage characteristics can have several possible causes. In Section 1.8.1 the case of a Schottky diode was presented, where the difference in workfunctions forms a barrier between a semiconductor and a metal. Conduction through this barrier leads to non-linear $I(V)$ characteristics similar to that of a diode (pn junction). Any diode (pn junction or semiconductor junction) shows an exponential increase in current after a certain (positive or forward) threshold voltage. In reverse a diode would only show the leakage current and for high enough voltages a breakdown current flows. Tunnel barriers (metal oxide or insulator) between conductors (metals) will show an exponential rise in current as well (Section 1.9)

Obviously, the non-linear $I(V)$ are not caused by a pn junction (semiconductor junction) at the contacts, because for the contacts a metal was used. A pn junction between adjacent cluster is unlikely as well, since the clusters were all formed the same way and if semiconducting they would be all doped the same way.

If the non-linear $I(V)$ s is caused by Schottky diodes at the contacts, then the samples presented here would have two Schottky diodes back to back. That means that the observed $I(V)$ is actually the breakdown of the respective Schottky diodes. Further, the Schottky diode formed would be most likely non-ideal. The $I(V)$ of a non-ideal Schottky diode can be described by a non-ideality factor, which causes the current to already increase before the threshold (or breakdown) voltage.

To form a Schottky barrier it requires a metal-semiconductor junction and it is known that in bismuth a transition from semimetal to semiconductor occurs [Lin et al., 2000]. It could be argued that the increase in resistance with decreasing temperature indicates semiconducting behaviour, but a negative temperature coefficient of resistance can be also produced by films of disordered metallic islands [Kaiser, 2001].

A more likely candidate to cause the non-linear $I(V)$ would be a metal1 to insulator to metal2 junction (Section 1.9) because the semimetal to semiconductor transition is not needed. Since two different metals are involved (bismuth and gold) the $I(V)$ characteristic should be asymmetric for backward and forward bias but similar to above, two of those junctions are combined back-to-back, which would therefore produce a symmetric non-linear $I(V)$.

It was observed that non-linear effects occurred for highly resistive samples (see Table 6.3). Linear $I(V)$ characteristics were observed when the sample had a low resistance. If tunnelling is considered, then a high resistance is expected.

In addition, studies on the thermoelectric properties of bismuth nanowires [Cronin et al., 2002] reported non-linear $I(V)$ characteristics. The bismuth nanowire had an oxide shell and tunnelling conduction through the oxide was found to cause the non-linear behaviour.

So why has no one (in the group at University of Canterbury) seen non-linear $I(V)$ s before? Table 6.8 emphasizes the difference using slot samples (or any nanoscale cluster device) compared to previously established sample layouts. Let us consider that the clusters individually form a contact to the electrodes having barriers of individual heights and widths. For large contact areas then the possibility of finding a low barrier is much higher than for a small contact area (Section 1.9). A large contact area was certainly the case for the samples previously used (i.e. V-groove style, percolating films and interdigitated fingers). To investigate this behaviour the contact area between the cluster ensemble and the contact electrodes was varied between $0.2\mu\text{m}^2$ and $< 8\mu\text{m}^2$ for the nanoscale cluster assembled samples. No conclusive effect was seen. However, the changes in contact area were small compared to the contact areas of previous samples (Table 6.8).

6.6.2 Non-Linear $I(V)$ Examples

A non-linearity was seen for all sample styles and all investigated cluster materials. The following has a look at the conduction mechanism of a few selected samples in more detail. It explains the reason for the occurrence of non-linear $I(V)$ characteristics in those samples, but can be generalised to the analysis of other samples.

Percolation Style Sample Ag2

Here the interesting behaviour of the sample Ag2 (shown in Section 6.2) is discussed. Unlike the other samples of this batch, while taking a $I(V)$ sweep no steps were noticed indicating that no annealing occurred. For the maximum voltage of 10 V in Figure 6.5 a maximum current of about 22 nA was measured. This is a resistance of about $450\text{ M}\Omega$ which is almost twice as much as the onset resistance (see Table 6.2).

Since all of the other samples (Table 6.1) showed linear $I(V)$ behaviour the connections between the clusters are assumed to be Ohmic. From percolation theory it is known that for an infinite lattice at exactly p_c at least one current path exists [Stauffer, 1985]. Before p_c nearly continuous paths exist having small gaps. Current can flow by tunnelling through the gaps. However, for tunnelling

conduction a large resistance exists. The sample Ag2 indeed had a much larger onset resistance than any other sample (Table 6.2). In conclusion, the non-linear $I(V)$ for sample Ag2 is likely to be due to barriers in between adjacent clusters.

Pd Four Point Sample 4pt#15

Another example for tunnelling conduction through adjacent clusters is sample 4pt#15 (Figure 6.25). Looking at the $I(V)$ for this sample it can be seen that the two point resistance and the four point resistance are non-linear. A non-linear two point measurement by itself is not very meaningful, since it could indicate both a tunnelling contact to cluster wire barrier or a tunnelling cluster to cluster barrier. Having a non-linear four point resistance measurement as well indicates a cluster to cluster barrier tunnelling. This type of non-linearity disappears if more clusters are deposited onto the sample. The tunnelling conduction of sub-percolation threshold palladium cluster films is used to fabricate high sensitive hydrogen sensors [NCD Ltd. , 2004].

Bismuth Cluster Nanoscale Samples

The $I(V)$ characteristics for the bismuth slot samples (Section 6.3) and the bismuth and antimony cluster four point samples (Table 6.7) show non-linear behaviour. For the slot samples only two point $I(V)$ s were possible to measure and no conclusive statement can be made on whether the non-linear behaviour is due to cluster-cluster or cluster-contact tunnelling. The two point resistance measurements of bismuth cluster four point samples showed non-linear $I(V)$ (Figure 6.20) as well, but the four-point resistance was linear (Figure 6.22). This indicates that the non-linearity is due to the contact between the clusters and the electrodes. Furthermore, it was found that the resistance for the four point cluster samples did not depend on the length of the wire. A length dependency of the resistance could indicate tunnelling conduction between adjacent clusters.

In conclusion, the non-linear $I(V)$ in bismuth cluster assembled four point samples was found to be due to barriers between the cluster ensemble and the contacts. This was found to be true for the case of antimony cluster assembled four point samples as well. The non-linear $I(V)$ s in bismuth slot samples (Section 6.3) are believed to be due to barriers at the contacts.

6.7 Fitting the Data

6.7.1 Data Fitting Procedure

In the previous section it was established that tunnelling through a small barrier at the contacts is a good explanation for the observed non-linear $I(V)$. Further investigation involved fitting of the $I(V)$ data to a given theoretical equation.

The theories to model the non-linear conduction were presented in Section 1.9. Before showing the results of the fitting attempts, some of the key steps involved while fitting the non-linear $I(V)$ to a theoretical equation are given.

The fitting procedures were done using Matlab programming. For the input data, the raw data sets of a $I(V)$ sweep were used. During the sweeps, starting from 0 the voltage was swept to a maximum voltage V_{max} , then reversed and swept to $-V_{max}$, reversed again and finished at 0. For the fit, the low voltage data points were ignored below a certain threshold voltage $|V_t|$.

Using the `nlinfit` routine in Matlab, the data set was compared to a fit equation (Equation 1.17 or Equation 1.21 or Equation 1.22). A set of start parameters had to be provided. The `nlinfit` routine in Matlab returns the least squares parameter estimates. That is, it finds the parameters that minimize the sum of the squared differences between the data and their fitted values. The returned parameters could then be analysed.

6.7.2 Fitting Parameters

Fit using Simmons theory

For this fitting procedure, Simmons equation for the medium voltage case (Equation 1.17 in Section 1.9) was used. The fit equation is

$$I = \frac{1}{R_0}V + \Gamma V^3. \quad (6.2)$$

Table 6.9 shows the fit parameter for samples 4pt#27, 4pt#28, 4pt#12 and 4pt#26. These are typical values for bismuth and antimony cluster four point samples respectively. The parameter R_0 describes the zero bias resistance and Γ describes the curvature of the non-linear $I(V)$. Typical values for R_0 are $> M\Omega$. Interestingly the values for R_0 for the antimony cluster samples are about two orders of magnitude lower than for the bismuth cluster samples. For the notation of the contacts see Figure 6.17.

Using the fit parameters in Table 6.9 and Equations 1.19, 1.18, the barrier heights φ_B and widths s_B can be determined. The area A used was the area of the overlap between the clusters with the respective contacts and m is the electron mass. Bismuth has a highly anisotropic effective electron mass, hence the electron mass at rest was used in the calculations. Table 6.10 gives the φ_B and s_B for selected four point samples. Note, that having negative fit parameters in Table 6.9 it is not possible to calculate the barrier height and barrier width.

As can be seen from the subset of samples in Table 6.10, the calculated barrier heights range from about 0.5 eV to around 3 eV having barrier widths ranging from about 1.5 nm to about 3 nm. Those values are expected for a small barrier.

Contacts	R_0 [Ω]	Γ [A/V^{-3}]	R_0 [Ω]	Γ [A/V^{-3}]
	Sample 4pt#27 Antimony 1 V		Sample 4pt#28 Antimony 1 V	
34&56	19×10^6	1.67	13×10^6	1.55
34&12	14×10^6	1.70	8.3×10^6	1.50
34&78	7.9×10^6	4.88	14×10^6	1.55
12&78	3.8×10^6	3.76	8.1×10^6	1.62
12&56	15×10^6	1.79	7.5×10^6	1.57
78&56	10×10^6	6.68	13×10^6	1.68
	Sample 4pt#12 Bismuth 0.5 V		Sample 4pt#26 Bismuth 0.5 V	
34&56	2.0×10^7	1.16	6.2×10^7	45.6
34&12	1.5×10^9	2.59	1.0×10^8	1.61
34&78	2.5×10^9	3.67	6.5×10^8	2.65
12&78	4.3×10^9	0.64	7.0×10^8	2.94
12&56	2.0×10^9	3.01	6.6×10^7	2.03
78&56	2.6×10^9	3.31	5.5×10^8	3.42
	Sample 4pt#12 Bismuth 1 V		Sample 4pt#20 Bismuth 1 V	
34&56	1.7×10^7	0.76		
34&12	-9.7×10^9	-28.5		
34&78	-4.7×10^9	-16.3		
12&78	4.9×10^9	0.96	-1.2×10^6	-6.94
12&56	1.6×10^{10}	43.8	2.8×10^9	0.96
78&56	-1.4×10^{10}	-44.1	6.4×10^9	5.36

Table 6.9: Fit parameters using Equation 1.17 on $I(V)$ sweeps with maximum voltages of 1 V on the four point samples 4pt#27, 4pt#28, 4pt#20 and 4pt#12 and with maximum voltages of 0.5 V on the four point samples 4pt#12 and 4pt#26 respectively. 4pt#27 and 4pt#28 are antimony cluster samples and 4pt#12, 4pt#20 and 4pt#26 are bismuth cluster samples.

Contacts	s_B at 1 V	φ_B at 1 V	s_B at 0.5 V	φ_B at 0.5 V	s_B at 0.1 V	φ_B at 0.1 V
Sample 4pt#12 Bismuth clusters						
34&56	1.47 nm	3.11 eV	1.63 nm	2.51 eV	2.73 nm	0.81 eV
34&12	NA	NA	2.13 nm	1.91 eV	3.42 nm	0.73 eV
34&78	NA	NA	2.34 nm	1.63 eV	2.87 nm	1.04 eV
12&78	1.62 nm	2.99 eV	1.47 nm	3.66 eV	2.61 nm	1.07 eV
12&56	4.40 nm	0.48 eV	2.22 nm	1.79 eV	3.18 nm	0.86 eV
78&56	NA	NA	2.28 nm	1.72 eV	3.52 nm	0.68 eV
Sample 4pt#20 Bismuth clusters						
34&56						
34&12						
34&78						
12&78	NA	NA			2.87 nm	0.45 eV
12&56	1.70 nm	3.27 eV			3.11 nm	0.90 eV
78&56	2.61 nm	1.38 eV			2.35 nm	1.63 eV
Sample 4pt#26 Bismuth clusters						
34&56			4.03 nm	0.39 eV	3.52 nm	0.50 eV
34&12			1.80 nm	2.20 eV	2.48 nm	1.10 eV
34&78			2.11 nm	1.83 eV	3.23 nm	0.74 eV
12&78			2.03 nm	1.54 eV	2.97 nm	0.70 eV
12&56			1.89 nm	1.91 eV	2.21 nm	1.35 eV
78&56			2.24 nm	1.59 eV	2.07 nm	1.93 eV
Sample 4pt#27 Antimony clusters						
34&56	1.78 nm	2.07 eV	2.10 nm	1.48 eV	2.44 nm	1.07 eV
34&12	1.75 nm	1.96 eV	2.06 nm	1.40 eV	2.38 nm	1.03 eV
34&78	2.22 nm	1.10 eV	2.36 nm	0.97 eV	2.96 nm	0.61 eV
12&78	1.89 nm	1.04 eV	2.17 nm	0.80 eV	2.80 nm	0.46 eV
12&56	1.77 nm	1.92 eV	2.06 nm	1.42 eV	2.48 nm	0.95 eV
78&56	2.41 nm	0.95 eV	2.43 nm	0.93 eV	3.06 nm	0.57 eV
Sample 4pt#28 Antimony clusters						
34&56	1.74 nm	2.11 eV	2.13 nm	1.38 eV	2.62 nm	0.89 eV
34&12	1.68 nm	2.05 eV	2.08 nm	1.33 eV	2.41 nm	0.96 eV
34&78	1.71 nm	2.06 eV	2.08 nm	1.37 eV	2.36 nm	1.05 eV
12&78	1.59 nm	1.69 eV	1.95 nm	1.10 eV	2.47 nm	0.66 eV
12&56	1.69 nm	1.99 eV	2.09 nm	1.30 eV	1.54 nm	0.28 eV
78&56	1.74 nm	1.97 eV	2.11 nm	1.33 eV	2.38 nm	1.03 eV

Table 6.10: Barrier heights and barrier widths calculated using Equation 1.19 and Equation 1.18 respectively for selected four point samples. The fit parameters were determined using Equation 6.2 on $I(V)$ sweeps with maximum voltages of 1 V, 0.5 V and 0.1 V respectively.

Equation 1.17 describes the $I(V)$ of one tunnel barrier. If the contacts are assumed to be those tunnel barriers, then for each $I(V)$ two tunnel barriers are present. This means that the values determined in Table 6.10 are not the actual value of the barriers and widths for one junction, since the voltage is dropped over two tunnel barriers. The values in Table 6.10 can only be overestimated.

What is interesting to note, is that for different maximum voltage sweeps, different barrier heights and widths were calculated for the same set of contacts. Increasing the maximum voltages, the barrier heights increase and the barrier widths decrease. This effect has not been noticed in Simmons theory. It could be that for increasing voltage Equation 1.17 does not hold true anymore ($eV < \varphi_0$ — see Section 1.9). However, judging by the values obtained for the barrier height Equation 1.17 should still be valid.

It was shown that the non-linear $I(V)$ data for the bismuth and antimony nanoscale cluster devices can be modelled using Simmons theory of tunnelling conduction for medium voltages. Using the obtained fit parameters, values for barrier heights and barrier widths were calculated, which are expected for small barriers. However, the barrier heights and the barrier widths should be fixed values when increasing the maximum sweep voltage. Instead, the barrier heights increased and the barrier widths decreased with increasing maximum voltage.

In addition, the equation for the tunnelling conduction had a V^3 dependence as highest order. The inclusion of higher order terms could describe the data better.

Fit using Equation 1.21

Observing that the barrier heights and barrier widths change for different maximum sweep voltages a different approach was tried to fit the data sets. The voltage dependence is now described by an exponential expression using Equation 1.21. Table 6.11 lists the fit parameters using Equation 1.21 for samples 4pt#27, 4pt#28, 4pt#20 4pt#12 and 4pt#26 respectively. The notation ‘NA’ means that fit parameters which model the data could not be obtained.

Comparing the fit approach using Equation 1.21 with the fit using Simmons model, it can be seen that the fit parameter R_0 in Table 6.9 and the fit parameter G_0 in Table 6.11 describe the same zero bias resistance (conductance). However, evaluating the conductances from $1/R_0$, it is found that the resulting values are all higher values than the respective G_0 in Table 6.11. Bismuth cluster samples did show a lower zero bias conductance than antimony cluster samples.

The parameter V_0 describes the voltage scale for the increase in conductance with voltage. It depends on the number of barriers along the conductance path as well as on the character of the barriers and how the voltage is split between them [Ozturk et al., 2006].

Contacts	G_0 [Ω^{-1}]	V_0 [V]	G_0 [Ω^{-1}]	V_0 [V]
	Sample 4pt#27 Antimony 1 V		Sample 4pt#28 Antimony 1 V	
34&56	4.00×10^{-8}	0.81	5.97×10^{-8}	0.84
34&12	5.56×10^{-8}	0.80	9.33×10^{-8}	0.86
34&78	10.7×10^{-8}	0.51	5.67×10^{-8}	0.84
12&78	21.3×10^{-8}	0.56	9.57×10^{-8}	0.82
12&56	5.16×10^{-8}	0.78	10.3×10^{-8}	0.84
78&56	9.01×10^{-8}	0.47	6.00×10^{-8}	0.80
	Sample 4pt#12 Bismuth 0.5 V		Sample 4pt#26 Bismuth 0.5 V	
34&56	4.48×10^{-8}	1.46	1.95×10^{-8}	0.21
34&12	5.54×10^{-10}	0.75	8.38×10^{-9}	1.10
34&78	3.21×10^{-10}	0.58	1.28×10^{-9}	0.74
12&78	2.20×10^{-10}	2.57	1.18×10^{-9}	0.69
12&56	4.03×10^{-10}	0.67	1.30×10^{-8}	0.90
78&56	3.17×10^{-10}	0.63	1.48×10^{-9}	0.62
	Sample 4pt#12 Bismuth 1 V		Sample 4pt#20 Bismuth 1 V	
34&56	4.86×10^{-8}	1.33		
34&12	NA	NA		
34&78	NA	NA		
12&78	1.61×10^{-10}	1.12	NA	NA
12&56	1.84×10^{-10}	0.36	2.84×10^{-10}	1.11
78&56	NA	NA	1.19×10^{-10}	0.46

Table 6.11: Fit parameters using Equation 1.21 on $I(V)$ sweeps with maximum voltages of 1 V on the four point samples 4pt#27, 4pt#28, 4pt#20 and 4pt#12 and with maximum voltages of 0.5 V on the four point samples 4pt#12 and 4pt#26 respectively. 4pt#27 and 4pt#28 are antimony cluster samples and 4pt#12, 4pt#20 and 4pt#26 are bismuth cluster samples.

Contacts	G_0 [Ω^{-1}]	h	V_0 [V]	G_0 [Ω^{-1}]	h	V_0 [V]
	Sample 4pt#27 Antimony 1 V			Sample 4pt#28 Antimony 1 V		
34&56	3.24×10^{-8}	0.13	0.49	4.61×10^{-8}	0.14	0.46
34&12	4.61×10^{-8}	0.12	0.51	7.17×10^{-8}	0.15	0.46
34&78	9.19×10^{-8}	0.04	0.42	4.77×10^{-8}	0.12	0.54
12&78	16.1×10^{-8}	0.06	0.38	7.48×10^{-8}	0.13	0.47
12&56	4.20×10^{-8}	0.12	0.49	7.45×10^{-8}	0.15	0.42
78&56	7.88×10^{-8}	0.02	0.40	4.54×10^{-8}	0.13	0.44
	Sample 4pt#20 Bismuth 1 V			Sample 4pt#26 Bismuth 0.5 V		
34&78				1.10×10^{-9}	0.24	0.34
12&78	8.03×10^{-8}	0.003	0.23			
78&56				1.29×10^{-9}	0.23	0.32

Table 6.12: Fit parameters using Equation 1.22 on $I(V)$ sweeps with maximum voltages of 1 V on the four point samples 4pt#27, 4pt#28 and 4pt#20 and with maximum voltages of 0.5 V on the four point sample 4pt#26 respectively. 4pt#27 and 4pt#28 are antimony cluster samples and 4pt#20 and 4pt#26 are bismuth cluster samples. Note: Fit results giving values $h < 1$ or even negative values for h are omitted.

Using Equation 1.21 the non-linear $I(V)$ can be described. The conductance in this model is assumed to rise exponentially with voltage. For small barriers the voltage is eventually high enough to excite carriers over the barrier and the conductance saturates at a fixed value — the conductance of the material.

Fit using Equation 1.22

Another investigation of the data sets used Equation 1.22. Here the exponential increase is eventually limited by a saturation conductance G_h . The fit parameters using Equation 1.22, for the samples 4pt#27, 4pt#28, 4pt#20 and 4pt#12 and 4pt#26, are presented in Table 6.12. Fitting data sets having $I(V)$ sweeps with a maximum voltage of less than 250 mV did not prove successful.

The fit parameter G_0 is again the zero bias conductance, but differs from the zero bias conductance obtained by using Equation 1.21 and from the zero bias resistance obtained using Simmons medium voltage equation. The zero bias conductance obtained using Equation 1.22 was always the lowest for all contacts.

The parameter V_0 in Table 6.12 describes the voltage scale of the conductance. Compared with the values obtained using Equation 1.21 it can be noticed that V_0 in Table 6.12 is almost half the value of V_0 in Table 6.11 for the antimony samples.

Using Equation 1.21 it was not possible to obtain fit parameters for some of the contacts of sample 4pt#12 with a maximum sweep voltage of 1 V. However, using Equation 1.22 fit parameters could be obtained. For sample 4pt#26, with

a maximum voltage of 0.5 V it was not possible to obtain fit parameters for two of the contacts.

What is interesting to note for sample 4pt#28, only two distinct values of G_0 are taken. Checking the contacts involved, it can be determined that only the combinations having 12 as one of these contacts have a higher conductance. From that it can be concluded that the contact resistance for this particular contact must have been much lower than for all the other contacts.

6.7.3 Detailed Analysis

Following is a detailed analysis on one of the contact 34&56 of sample 4pt#28 (see $I(V)$ in Figure 6.23).

Figure 6.29 shows the conductance voltage characteristic of contact 34&56 of sample 4pt#28 along with the three fit curves. The conductance was calculated by $G = I/V$. Comparing this with the theoretically calculated $G(V)$ in Figure 1.13, the observed $G(V)$ does not follow the theoretical form of Simmons medium voltage case of a tunnel barrier. Simmons predicted the conductance to be proportional to V^2 .

As can be clearly seen in Figure 6.29, the fit using Equation 1.22 (Kaiser) describes the data the best. Even though, Equation 1.21 (Ozturk) has a similar functional form, it can only describe the data for higher voltages, misrepresenting the lower voltages. This is also the reason for the different zero bias conductances for the three fits. It can be seen in Figure 6.29 that $1/R_0$ Simmons $> G_0$ Ozturk $> G_0$ Kaiser. Only the zero bias conductance determined by fitting the data using Equation 1.22 (Kaiser) gives the zero bias conductance of the data.

Since Equation 1.17 (Simmons) does not fully describe the data and only fits the higher voltages, the changes in barrier heights and barrier widths can be explained. This also means that the barrier widths and heights (Table 6.10) probably do not have a physical meaning, since the theory used to calculate them is not applicable for the observed non-linear $I(V)$.

Using Equation 1.21 only the high voltages are represented properly. This explains the difference in V_0 between Table 6.12 and Table 6.11. In addition, a larger G_0 is extrapolated due to the misrepresentation of the low voltages.

Figure 6.31 and Figure 6.32 show the residual $I(V)$ and $G(V)$ for contact 34&56 of sample 4pt#28. Here, the fit curves were subtracted from the data set. For low voltages the Simmons and Ozturk fits deviate from the data and only the Kaiser fit describes the data well for the whole voltage range. At higher voltages all the different models fit equally well the data set.

The empirical Equation 1.22 describes tunnelling through thin barriers between conducting regions with sufficiently small barriers so that tunnelling is thermally assisted. In the case of the bismuth or antimony cluster assembled devices a much

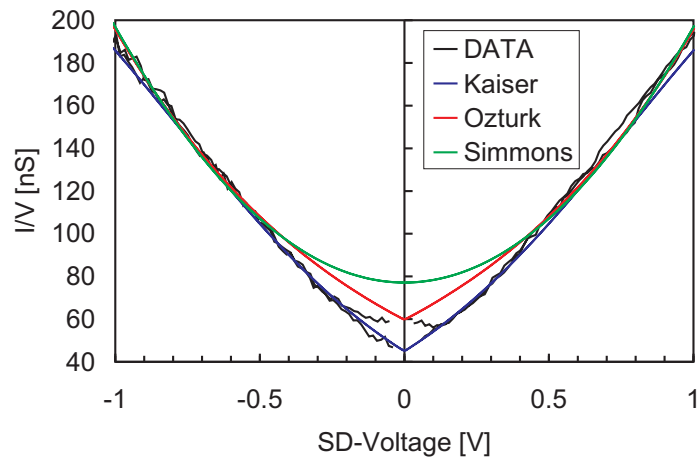


Figure 6.29: Fit curves and data for I/V of contacts 34&56 of sample 4pt#28.

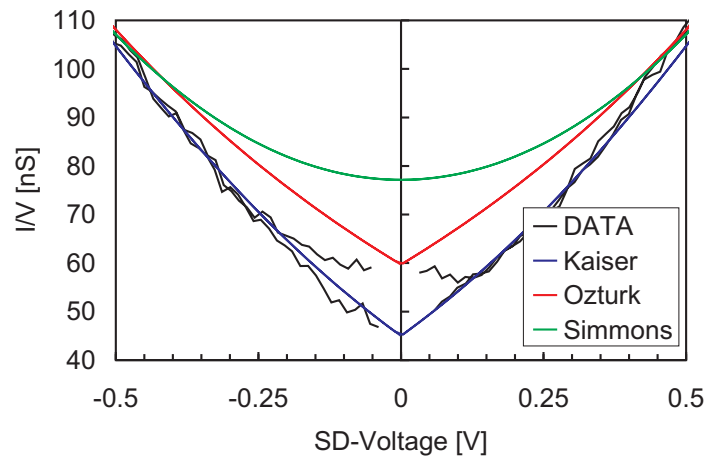


Figure 6.30: Detail of Figure 6.29.

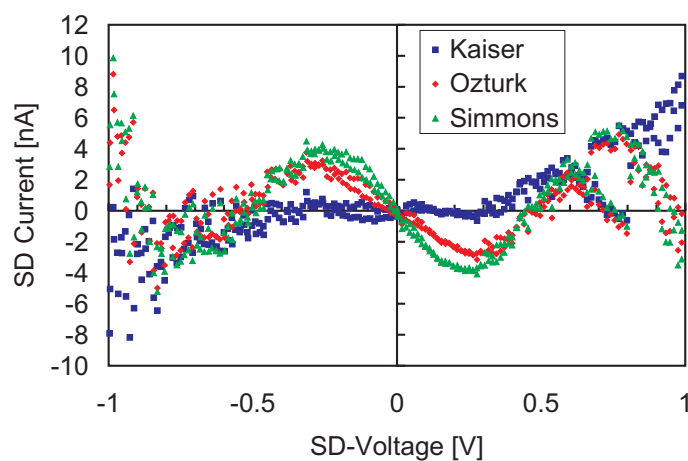


Figure 6.31: Residual $I(V)$ by subtracting the fit curves from the actual data for contact 34&56 of sample 4pt#28.

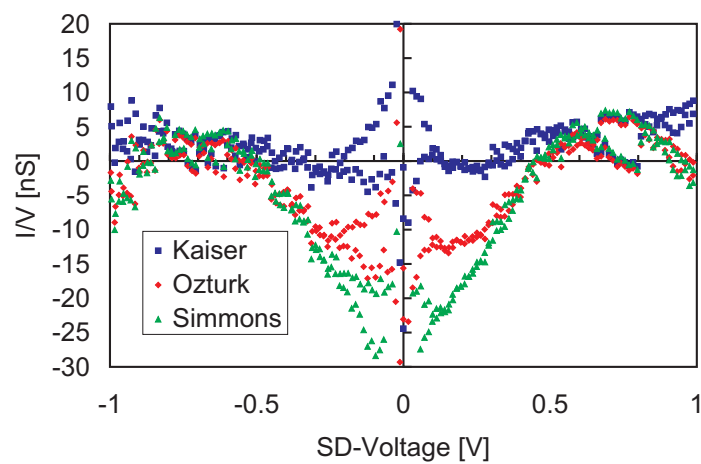


Figure 6.32: Residual $G(V)$ by subtracting the fit curves from the actual data for contact 34&56 of sample 4pt#28.

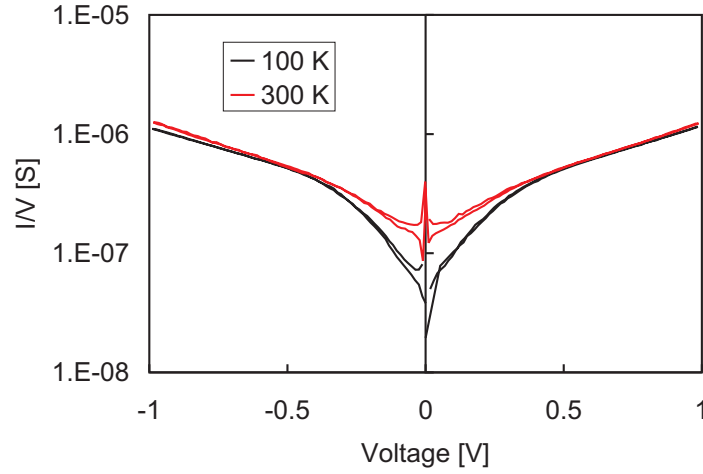


Figure 6.33: $G(V)$ for contact 12&78 of sample 4pt#27.

Contacts	G_0 [Ω^{-1}]	h	V_0 [V]	G_0 [Ω^{-1}]	h	V_0 [V]
	300 K			100 K		
34&56	3.24×10^{-8}	0.13	0.49	2.16×10^{-8}	0.12	0.35
34&12	4.61×10^{-8}	0.12	0.51	2.21×10^{-8}	0.09	0.30
34&78	9.19×10^{-8}	0.04	0.42	9.18×10^{-8}	0.06	0.42
12&78	16.1×10^{-8}	0.06	0.38	1.71×10^{-8}	0.07	0.41
12&56	4.20×10^{-8}	0.12	0.49	2.29×10^{-8}	0.10	0.32
78&56	7.88×10^{-8}	0.02	0.40	8.09×10^{-8}	0.03	0.44

Table 6.13: Fit parameters using Equation 1.22 on $I(V)$ sweeps of four point samples 4pt#27 at different temperatures.

simpler case of only two thin barriers is present if considering that the tunnelling barriers are between the cluster ensemble and the contacts.

Figure 6.33 shows the $G(V)$ at two different temperatures for contact 12&78 of sample 4pt#27. At a temperature of 100 K the zero bias G_0 is lower than at 300 K, which is expected. We have seen that the resistance for bismuth assembled device increases with decreasing temperature. Antimony cluster assembled devices show a negative TCR, too. What is interesting however, is the occurrence of two distinct slopes for the 100 K curve. For thermally assisted tunnelling, smaller barriers start only to inhibit conduction at lower temperature. The smaller barriers are however overcome for higher voltages.

Table 6.13 lists the fit parameter using Equation 1.22 for all contacts of sample 4pt#27 at 100 K and at room temperature. Similar to contact 12&78 in Figure 6.33, G_0 is lower at 100 K than at room temperature.

In the case of a bismuth cluster sample, the zero bias conductance decreases with decreasing temperature, too. Figure 6.34 shows the conductance for contact 34&56 of samples 4pt#18. The overall shape of the curve, i.e. the voltage

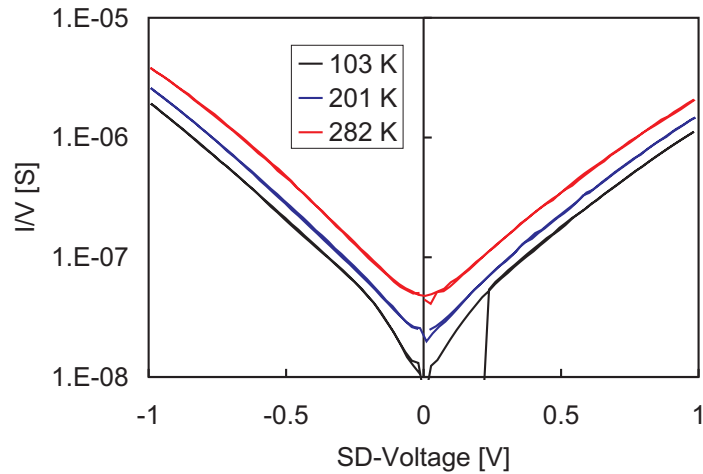


Figure 6.34: $G(V)$ for contact 34&56 of sample 4pt#18.

dependence, stays nearly the same for temperatures between 103 K and 282 K. Only for the lowest temperature of 103 K and for voltages lower than about 0.2 V can a different slope be observed.

In conclusion, it was found that the two point $I(V)$ of nanoscale bismuth and antimony cluster devices are non-linear. Fitting the data indicates that the non-linearity could be due to tunnelling conduction at the cluster to contact interface. It appears that the non-linear data might be fitted better using a model involving fluctuation-assisted tunnelling through barriers of different heights (two barriers).

6.8 Summary

In this chapter the electrical measurement of cluster assembled devices was investigated, which included $I(V)$ measurements and temperature dependent resistance measurements. Most interestingly, it was found that the nanoscale cluster devices (of semimetallic clusters) had non-linear $I(V)$ s. The investigation during this research to the cause of this non-linear behaviour indicates that tunnelling conduction occurs at the interface between the cluster-ensemble contact-electrode.

It was shown that non-linear $I(V)$ could be measured even for samples which did not show an onset of conductance. It could be argued that the quality of the contacts might cause a barrier to exist. However, it was shown that when depositing large coverage of metallic palladium clusters onto a nanoscale device the $I(V)$ were linear ruling out this possibility. Furthermore, the two test samples slots#5 and slots#8 showed metallic conduction when metal was deposited into the nanoscale opening.

Another possibility is that the non-linear $I(V)$ are the result of oxidised clusters. However, if the clusters were oxidised, than surely the non-linear behaviour

should be observed for percolating film samples as well. Non-linear $I(V)$ were measured for one percolating film sample and one palladium (metal) cluster nano-scale devices as well. The cause of the non-linear $I(V)$ in those two samples however is most likely due to tunnelling between adjacent clusters. Depositing more clusters onto the sample fills the gaps in between and a linear $I(V)$ can be measured.

References

- Baker, D. R., Paul, G., Sreenivasan, S., and Stanley, H. E. (2002). Continuum percolation threshold for interpenetrating squares and cubes. *Phys. Rev. E*, 66(4):046136.
- Cronin, S. B., Lin, Y. M., Black, M. R., Rabin, O., and Dresselhaus, M. S. (2002). Thermoelectric transport properties of single bismuth nanowires. In *The 21st International Conference on Thermoelectrics: ICT Symposium Proceedings, Long Beach, CA*, page 243.
- Goodberlet, J. G., Hastings, J. T., and Smith, H. I. (2001). Performance of the raith 150 electron-beam lithography system. *J. Vac. Sci. Technol. B*, 19(6):2499.
- Gourley, S. (2002). Electronic properties of cluster deposited bismuth nanowires. Master's thesis, University of Canterbury.
- Heremans, J., Thrush, C. M., Lin, Y.-M., Cronin, S., Zhang, Z., Dresselhaus, M. S., and Mansfield, J. F. (2000). Bismuth nanowire arrays: synthesis and galvanomagnetic properties. *Phys. Rev. B*, 61(4):2921.
- Kaiser, A. B. (2001). Electronic transport properties of conducting polymers and carbon nanotubes. *Rep. Prog. Phys.*, 64:1.
- Kaufmann, M. (2006). *Electron diffraction studies of unsupported antimony clusters*. PhD thesis, University of Canterbury, Christchurch.
- Lin, Y. M., Sun, X., and Dresselhaus, M. S. (2000). Theoretical investigation of thermoelectric transport properties of cylindrical Bi nanowires. *Phys. Rev. B*, 62(17):4610.
- Maximov, I., Zakharov, A. A., Holmquist, T., Montelius, L., and Lindau, I. (2002). Investigation of polymethylmethacrylate resist residues using photoelectron microscopy. *J. Vac. Sci. Technol. B*, 20(3):1139.
- NCD Ltd. (2004). www.nanoclusterdevices.com.
- Newman, M. E. J. and Ziff, R. M. (2000). Efficient monte carlo algorithm and high-precision results for percolation. *Phys. Rev. Lett.*, 85(19):4104.
- Ozturk, B., Blackledge, C., Flanders, B. N., and Grischkowsky, D. R. (2006). Reproducible interconnects assembled from gold nanorods. *Appl. Phys. Lett.*, 88:073108–1.

- Partridge, J. G., Brown, S. A., Dunbar, A. D. F., Kaufmann, M., Scott, S., Schulze, M., Reichel, R., Siegert, C., and Blaikie, R. J. (2004). Template-assembled antimony cluster mesowires and nanowires. *IEEE Transactions on Nanotechnology*, 3:61.
- Pratin, D. L., Heremans, J., Morelli, D. T., Thrush, C. M., Olk, C. H., and Perry, T. A. (1988). Growth and characterization of epitaxial bismuth films. *Phys. Rev. B*, 38(6):3818.
- Quintanilla, J., Torquato, S., and Ziff, R. M. (2000). Efficient measurement of the percolation threshold for fully penetrable discs. *J. Phys. A: Math. Gen.*, 33:L399.
- Schmelzer Jr., J. (2001). Finite-size effects in cluster films. Master's thesis, University of Canterbury.
- Schmelzer Jr., J., Brown, S. A., Wurl, A., Hyslop, M., and Blaikie, R. J. (2002). Finite-size effects in the conductivity of cluster assembled nanostructures. *Phys. Rev. Lett.*, 88:226802.
- Schulze, M., Gourley, S., Brown, S., Dunbar, A., Partridge, J., and Blaikie, R. J. (2003). Electrical measurements of nanoscale bismuth cluster films. *European Physical Journal D*, 24:291.
- Smith, G. E., Baraff, G. A., and Rowell, J. M. (1964). Effective g factor of electrons and holes in bismuth. *Phys. Rev.*, 135:A1118.
- Stauffer, D. (1985). *Introduction to percolation theory*. Taylor & Francis, London.
- Stöcker, H. (1994). *Taschenbuch der Physik*. Verlag Harri Deutsch, 2nd edition.
- Zhang, Z., Sun, X., Dresselhaus, M. S., Ying, J. Y., and Heremans, J. (2000). Electronic transport properties of single-crystal bismuth nanowire arrays. *Phys. Rev. B*, 61(7):4850.

Conclusions & Outlook

The conclusion of this thesis shows the three main results of this research. Firstly, a newly built and commissioned UHV-compatible cluster apparatus was used to fabricate clusters. Bismuth (and other) clusters were successfully incorporated into lithographically designed samples. Secondly, it was shown that the a new assembly method opens new possible ways in fabricating nanoscale cluster devices. Thirdly, performing $I(V)$ characteristics have shown that the conduction in nanoscale bismuth cluster devices is dominated by the cluster to electrode contact (for two terminal measurements).

UHV compatible Cluster Apparatus

This study uses clusters formed in a UHV-compatible cluster apparatus. During the course of this thesis, this UHV-compatible cluster apparatus was successfully built and commissioned. It was shown that this system provides a high degree of flexibility.

For example, two interchangeable cluster sources can be used enabling the fabrication of clusters from a wide range of materials. An inert gas aggregation source allowing the production of low melting point materials was used for the formation of 30 nm to 40 nm bismuth clusters and antimony clusters of varying size. With a magnetron sputter source, on the other hand, high melting point materials and even semiconducting materials can be used to form clusters. During this research, palladium clusters (< 10 nm), silicon clusters having diameter of up to 500 nm and bismuth clusters with less than 10 nm diameters were successfully fabricated using the magnetron sputter source.

Further, the UHV-compatible cluster apparatus can be used with two mass spectrometers, which allow the characterisation of the cluster size distributions. For this of course ionised clusters have to be used. Clusters formed using the magnetron sputtering source are already ionised. For the inert gas aggregation source an ioniser has to be used. The two mass filters are a von Issendorff & Palmer mass filter, which combines high cluster throughput with relatively high

resolution, and a home-built TOF of the Wiley-McLaren type. High throughputs are needed for the deposition of mass-selected clusters, which makes the von Issendorff & Palmer mass filter the preferred option for both deposition and characterising the cluster beam.

The UHV-compatible cluster apparatus presented here provides high cluster fluxes, which makes this system ideal for the production of cluster assembled nanoscale devices. Clusters can be deposited on samples mounted on an UHV-compatible cryostat cold finger. The cryostat and the electrical feedthroughs to the deposition chamber allow in-situ preparation of electrical device samples as well as in-situ testing of the cluster assembled devices. Electrical characterization of cluster assembled nanoscale devices can be done before, during and after the deposition. In-situ characterisation can be done at room temperature as well as cryogenic and elevated temperatures.

The cluster sources and mass filters not only can be chosen to exactly fit the requirements for the production of cluster assembled nanoscale devices, but samples can be deposited onto samples at various places within the UHV-compatible cluster apparatus. The cryostat sample holder can be moved closer to the cluster source, which enables that the exact cluster flux and beam spread can be chosen for the respective requirements during the fabrication.

Lastly, in all configurations, the diameter and spacing of all apertures is variable in order to control the range of source flow rates, pressures and temperatures, which together control the deposition rate and the mass distribution of the clusters produced.

Preparation of Nanoscale Cluster Devices

Using the UHV-compatible cluster apparatus, bismuth (and other) clusters were incorporated into lithographically defined devices. This thesis started with the proposal of a layout of a device to investigate fractal conductance fluctuations in nanoscale bismuth cluster devices. During the course of this research changes however had to be made to the originally proposed design to yield measurable cluster devices.

In the investigation of possible sample styles a novel cluster assembly method was discovered. With this assembly method it was instantly possible to fabricate cluster devices with nanoscale resolution. The results were compared to molecular dynamic simulations of cluster surface collisions. It was found that the reflection or adhesion of clusters on surfaces is most important for plastic deformation of the clusters.

The cluster assembly discovered during this research can be also used for lift-off free lithography. That means after the metallisation with clusters no additional lift-off step is necessary. Further, it was shown that arbitrary patterns can be successfully filled with clusters.

Electrical Measurements

Bismuth (and other) clusters were incorporated into electrically contacted samples and electrical measurements were performed. In percolating film samples previously used the onset of conduction marked the point where a cluster network spanning from one electrode to the other formed. In nanoscale cluster assembled devices an onset of conduction was not always observable. Post-deposition $I(V)$ however showed that often a connection had in fact been formed. It was shown that this has to do with the quality of the contact interface between the cluster ensemble and the contact material. Previously it was expected that the point of contact would be at the tip of the contact electrodes to the clusters.

The quality of the cluster to contact interface prevents not only the observation of an onset, it was also shown that the electrical measurements performed on nanoscale cluster devices are dominated by the cluster to contact interface. That is for two point resistance measurements a non-linear $I(V)$ was measured. Four point resistance measurements of bismuth or antimony cluster assembled nanoscale devices however showed linear $I(V)$ behaviour. Temperature dependent resistance measurements on a four point bismuth cluster sample showed that the resistance increases with decreasing temperature (negative TCR). Since scattering at boundaries is dominant in cluster wires this increase in resistance was related to the change in carrier concentration in bismuth with temperature.

For percolating cluster films annealing, by applying a high voltage, proved successful to reduce the resistance of the film. Using nanoscale cluster devices current limited annealing was successful as well. Passing a high current through a nanoscale cluster wire however proved to be fatal, melting the bismuth clusters. This is due to the much more limited number of current paths and the total number of clusters forming the wire compared to previously used sample layouts.

For bismuth clusters, the resistivity (determined by four point measurements) was found to be 40 - 50 times higher than that of bulk bismuth. When annealed, the resistivity of a bismuth cluster assembled wire was found to be only 10 times that of bulk bismuth.

It was established that the non-linear $I(V)$ are due to tunnelling conduction between the cluster ensemble and the contact electrodes. A fitting of the data to three existing tunnelling theories was attempted. It was found that the observed non-linear $I(V)$ characteristics can be explained by a theory of thermally assisted tunnelling conduction.

Outlook

With the UHV-compatible cluster apparatus presented here it is possible to investigate cluster assembled devices for many more different cluster materials. The use of an IGA source makes low melting point materials readily available for cluster production. The magnetron sputtering source then provides the possibility to study clusters of high melting point materials and semiconducting materials. It is possible to use other cluster sources enabling the fabrication of clusters of a wide variety of materials due to the flexibility of the UHV-compatible cluster apparatus.

So far, the inert gas aggregation source was successfully refined to yield silver clusters as well as copper clusters and previously an inert gas aggregation source was used for the diffraction study of lead and zinc clusters. Copper is used for interconnects in existing micro chips. Using copper clusters, nanowires and interconnects could be formed using the bottom-up approach presented in this thesis.

Further investigations are currently underway into the formation of germanium clusters using an inert gas aggregation source. Germanium is a semiconducting material and if germanium clusters can be assembled in nanoscale devices (similar to the ones presented in this study) it would be possible to form nanoscale transistors.

The high surface to volume ratio of clusters makes them ideal for highly sensitive sensors or catalysts. Most catalytic reactions occur at the surface of the catalyst. Now increasing the surface without having to increase the amount of the material could help making catalysts more economic. Further, it is known that palladium swells when absorbing hydrogen. Having a sub-percolation threshold palladium cluster film exposed to hydrogen, a sharp increase in conductance can be noticed since now the swelling palladium cluster form continuous current paths. Using the assembly method presented in this thesis, the cluster assembled sensors could be formed as nanowires, rather than having to rely on a percolating network in a thin film of clusters. Having more than one of such sensor wires parallel could increase the signal dramatically. In a film of clusters the number of current paths is unknown, but the number of sensor wires can be pre-selected when directly assembled. A pre-selection of the number of wires guarantees identical signal responses of the produced sensors.

The novel assembly method presented in this research needs to be further investigated using different materials and different size clusters. To date, in addition to the research presented in this thesis, investigations were done on the cluster surface interaction of copper and palladium clusters. For example the adhesion of bismuth, antimony and copper clusters to various organic and inorganic substrates has been investigated. The substrates investigated include resists and materials commonly encountered in device fabrication methods (photo-resist

which is used for large scale metallisation, SU8 - another electron beam sensitive resist, silicon dioxide substrates, silicon nitride substrates). It has been shown that the clusters tend to adhere to the substrates but reflect off the resists.

Arbitrarily shaped patterns can be produced by the novel assembly method, which allows for an even more elaborate design of the nanoscale devices. For instance, side gates (formed using clusters) could be placed close to a cluster assembled wire and formed at the same time as the wire. Using side gates and a semiconducting cluster wire (for instance germanium cluster wire), the current through the cluster wire could be altered by applying a voltage to the side gates. Furthermore, cluster wires which split into two branches at one end (Y-branched nanowire) could be produced. Each of the branches would have a side gate (of course formed using clusters as well). Then, by applying alternatively a voltage to the side gates next to the branches, the current through the wire could be directed towards one or the other branch.

It is also plausible to individually place clusters forming islands of one or more clusters. Islands of conducting materials between two electrodes have been the interest of many researchers for a long time. Further, arranging clusters (or groups of clusters) in an array of islands, it would be relatively easy to form quantum dot structures. The use of clusters to form single electron transistors or quantum dot structures already provides the means of controlling the size of the island by controlling the cluster size. The cluster size can be either controlled when forming the clusters within the source, or passing the beam of ionized clusters through the Issendorff & Palmer mass filter. The assembly method presented here would then allow for the mass production of single electron transistors or quantum dots with identical size islands. Hereby, clusters are deposited onto the preformed structures but would only position (adhere) themselves where they are wanted and would reflect off anywhere else. However, further refinement of the assembly method is needed to be able to position the individual clusters with more precision than is possible at the moment.